UNIVERSITY OF CALIFORNIA, MERCED

Mechanical interactions in biological active filaments and networks

A dissertation submitted in partial satisfaction of the
requirements for the degree
Doctor of Philosophy

in

Physics

by

Patrick S. Noerr

Committee in charge:

Professor Bin Liu, Chair
Professor Kinjal Dasbiswas
Professor Ajay Gopinathan

2024

The dissertation of Patrick S. Noerr is approved, and it is acceptable in quality and form for publication on microfilm and electronically:

(Professor Kinjal Dasbiswas)

(Professor Ajay Gopinathan)

(Professor Bin Liu, Chair)

University of California, Merced

2024

DEDICATION

To Samara and Graham.

EPIGRAPH

To attain knowledge, add things everyday.
To attain wisdom, remove things every day.
—Lao Tse

TABLE OF CONTENTS

LIST OF FIGURES

LIST OF TABLES

ACKNOWLEDGEMENTS

Thank you first and foremost to my beautiful wife, Samara, and our new son, Graham. You are my light and my life; you are everything to me. I would like to thank my parents Beverly and Robert who have dedicated their lives to serving each other and my siblings and I, setting a pure example of success in the most meaningful aspects of life. To my siblings, I love you. Thank you for supporting me and giving me laughter and encouragement in my educational journey and beyond. To my friends, thank you for making the road trip to Merced every now and again and giving Samara and I a place to crash for the weekend when we were able to make it down south.

Thank you to my doctoral advisor Kinjal. It is an incredible honor to have been your first PhD student. I appreciate that you spent so much time investing in and brainstorming with me, I will forever cherish what I have learned from you and hope I will be able to pass that on to others. I am grateful that we could do fascinating and meaningful science while cracking jokes and having fun. Thank you for being persistently and proactively involved in our projects and empathetic and flexible when life got in the way.

Thank you to Ajay Gopinathan. You enriched every project we were a part of and were supportive along every step of this journey. Thanks for all you do (which I'm sure is immeasurable) with respect to science at UC Merced and for the biological physics community at large.

I would like to thank the University of California, Merced, as it made this wonderful period possible. It is a beautiful campus filled with tremendous talent. I am proud to forever be a part of the bobcat family and am excited to see how our young campus grows and continues to make far reaching contributions.

A huge thank you to the National Science Foundation (NSF) Center for Cellular and Biomolecular Machines (CCBM), to those who are responsible for its creation, to those who upkeep it and facilitate its growth, and to all the participants. Thank you for funding my research as a fellow and for giving me the opportunity to play a role in the development of the center as a graduate mentor fellow. I could not dream of a more impressive interdisciplinary science center. The center is a crucial pillar of the success our departments are propagating on a daily basis by making a space for a broad

spectrum of expertise to think about several classes of problems on a panoply of scales. As a result, we have a vast array of powerful and effective collaborations forging the frontier of these complex problems.

VITA

2017	A. S. T. in Mathematics and Physics, Crafton Hills College
2019	B. S. in Physics, California State University San Bernardino
2019 - Present	Ph. D. in Physics, University of California, Merced

PUBLICATIONS

P. S. Noerr, S. E. Zamora Alvarado, F. Golnaraghi, K. E. McCloskey, A. Gopinathan, K. Dasbiswas, “Optimal mechanical interactions direct multicellular network formation on elastic substrates”, Proceedings of the National Academy of Sciences, 120 (45) e2301555120, 2023.

S. Bose, P. S. Noerr, A. Gopinathan, A. Gopinath, K. Dasbiswas, “Collective states of active particles with elastic dipolar interactions”, Frontiers in Physics, 10, 876126, 2022.

P. S. Noerr, M. Guruprasad, D. A. Beller, A. Gopinathan, K. Dasbiswas, “Off-axis propulsion and stochastic buckling drive chiral motion of active filaments”, 2024 (in preparation).

FELLOWSHIPS AND AWARDS

Physics graduate group travel award (Spring 2024).

Center for Cellular and Biomolecular Machines (CCBM) Graduate Mentor Fellow (Spring 2022 - Spring 2024).

Center for Cellular and Biomolecular Machines (CCBM) Fellow (Fall 2020, Spring 2021, Fall 2021, Spring 2023).

Center for Cellular and Biomolecular Machines (CCBM) Travel Award (Fall 2022).

CONFERENCES

American Physical Society March Meeting – “Optimal mechanical interactions direct multicellular network formation on elastic substrates”, contributed talk, 2024.

Active Polymers – Leiden University – “Off-axis propulsion and stochastic buckling drive chiral motion of active filaments”, poster, 2024.

CCBM External Advisory Board Meeting, poster and talk, 2023.

American Physical Society March Meeting – “Substrate mediated mechanical interactions induce multicellular network formation”, contributed talk, 2023.

Complex Active and Adaptive Material Systems Gordon Research Conference, poster, 2023.

Active Matter symposium – UC Merced – “Optimal mechanical interactions direct multicellular network formation on elastic substrates”, poster, 2022.

Frontiers in Soft Matter and Macromolecular Networks – “Optimizing multicellular network formation on elastic substrates”, poster, 2022.

American Physical Society March Meeting – “Optimizing multicellular network formation on elastic substrates”, contributed talk, 2022.

CCBM External Advisory Board Meeting, talk, 2021.

Banff International Research Station - Mathematics of the Cell: Integrating Signaling, Transport and Mechanics, lightning talk, 2021.

CCBM External Advisory Board Meeting, virtual poster, 2020.

PROFESSIONAL SERVICE AND OUTREACH

CCBM STEM Pathways Presentation (Summer 2023).

CCBM Virtual Sessions – “Modeling Cell Movements on a Computer!” (Summer 2023).

CCBM Virtual Sessions – “Modeling Cells and Organelles on Computers” (Summer 2022).

Peer Review - Physical Review E (2022).

CCBM Virtual Sessions – “Modeling Cells and Organelles on Computers”, (Summer 2021).

CCBM Virtual Sessions – “Cell Division on a Computer”, (Summer 2020).

ABSTRACT OF THE DISSERTATION

Mechanical interactions in biological active filaments and networks

by

Patrick S. Noerr
Doctor of Philosophy in Physics

University of California Merced, 2024

Professor Kinjal Dasbiswas

Active matter systems are those whose individual constituents convert energy to move or perform mechanical work. Physicists have long been fascinated by active matter systems as they are inherently out of thermal equilibrium, making them much more difficult to classify and quantify using the traditional techniques of statistical mechanics. Biology, being comprised of many such systems, has become one of the most sought-after fields for the physics community. In this work, we are predominantly interested in biological machines that consume chemical energy, like ATP, and use this fuel to exert forces on their surroundings. We utilize theoretical and computational techniques to investigate these systems as *in silico* is a cost effective way to span the parameter space and learn design principles that can both decipher the current generation of *in vivo* and *in vitro* experiments and propel the next. Here, we develop minimal mechanical models, conduct computer simulations, and apply quantitative analytics at the cellular level (chapters 2, 3, and 4) and subcellular scale (chapter 5) to both gain insight into relevant design principles and make testable predictions regarding the system constituents and emergent behavior thereof. Specifically, in chapter 2, we ask if cells modeled solely as coarse grained anisotropic contractile force dipoles are sufficient to produce branched multicellular network structures and how the mechanical properties of the substrate and cell response to the substrate affect this tendency. In chapter 3, we ask if cells modeled as contractile dipoles in a discretized elastic medium can give rise to a strong nonlinearity in force production as a function of density suggested by recent experiments of

fibroblasts embedded in collagen gels. In chapter 4, motivated by a wide variety of systems like synthetic Janus colloids in an alternating electric field and magnetotactic bacteria, we explore the collective behavior of highly motile contractile anisotropic dipoles. Lastly, in chapter 5, we ask if the geometric helicity of microtubules coupled to motor propulsion is sufficient to produce emergent chiral motion of isolated microtubules, rather than a fundamental chirality given by intrinsic curvature.

Chapter 1

Introduction

1.1 Motivation

1.1.1 Mechanobiology

Once thought to be irrelevant relative to genetics and molecular biology, the role of mechanics in biological structure and function is found to be evermore crucial. Cells utilize mechanical force generation, transmission, and response to accomplish a host of functions including locomotion [1], division [2, 3], gene expression and regulation [4], and differentiation and maturation [5].

While there are a multitude of interactions and influences at play in these processes, including chemical, thermal, and otherwise, one of the key questions we ask throughout these studies is: How do mechanical forces facilitate coordinated behavior in noisy biological environments? Will a deeper understanding of the role of mechanics at this scale offer insights into cell and tissue pathologies? Can we glean design principles applicable to regenerative medicine and bioengineering via tissue fabrication or otherwise? Specifically, in chapter 2, we ask if substrate-mediated mechanical interactions via mutual substrate deformations are sufficient to form vascular network structures and how sensitive this self-assembly process is to the mechanical properties of the substrate. In chapter 3, we ask if active regulation of cell forces in elastic media can give rise to a phase transition in global contraction. In chapter 4, we investigate the properties of collective motion resulting from highly motile mechanically interacting particles. In chapter 5, we study the motion of semi-flexible microtubules propelled by directed mechanical forces of kinesin molecular motors.

1.1.2 Active matter

While many materials traditionally studied by physicists are at thermodynamic equilibrium, living matter is typically active. Active matter are non-equilibrium systems whose constituents convert a form of available energy into directed motion at the scale of the constituents. Examples include molecular motors that hydrolyze ATP to take steps along cytoskeletal filaments, Janus particles whose metallic hemisphere catalyzes the decomposition of ambient peroxide, flagella and cilia powered bacteria and protozoa up through macroscopic matter such as schools of fish, flocks of birds, and heavy-metal concert going humans. Active matter is of ever-increasing interest to the physics community as they typically exhibit dynamics not expected at thermal equilibrium and are more and more ubiquitous as both synthetic and organic systems [6].

Several canonical idealizations of active matter systems include active Brownian particles (ABPs) wherein particle velocity magnitude is fixed but reorients diffusively [7], run and tumble particles wherein particle velocity magnitude is fixed and undergoes stochastic tumble events resulting in random orientation [8], and Ornstein-Uhlenbeck particles wherein both particle velocity magnitude and orientation are dynamic [9]. Characteristic behaviors of these models distinguishing them from equilibrium systems include boundary accumulation, coordinated motion, and aggregation not requiring inter-particle interactions - a phenomenon coined motility induced phase separation or MIPS [10].

A compelling question in the field remains, how do specific interaction forms alter the behavior of these active systems? In chapter 2, we investigate the collective configurations of agents with anisotropic contractile dipolar active force patterns. In chapter 3, we ask if activity in the form of forces on a lattice can give rise to a phase transition in boundary stress. In chapter 4, we explore the consequences of ABPs with long-range elastic interactions in a confined environment. In chapter 5, we ask if off-axis propulsion forces on a filament with both bending and stretching rigidity are sufficient to produce emergent chiral motion.

1.2 Background

1.2.1 Cell mechanics

While cells routinely communicate using chemical signals, they also sense each other through mechanical forces that they exert on each other, either through direct cell–cell contacts or indirectly, through mutual deformations of a compliant, extracellular substrate [11, 12]. Large and measurable substrate deformations [13] are produced by many types of adherent cells. These use mechanical forces actively generated by myosin motors in their actin cytoskeleton to change shape, move, and sense their surroundings [14]. Adherent cells ubiquitously induce contractile mechanical deformations in elastic media. The resulting inter-cellular communication is longer ranged, faster, and more general than chemical signaling which typically requires diffusive transport and specific chemical interactions. Elastic substrate-mediated inter-cellular mechanical communication has been demonstrated for several contractile cell types. For example, endothelial cells modulate their inter-cellular contact frequency according to substrate stiffness [15], cardiomyocytes synchronize their beating with substrate mechanical oscillations induced by a distant probe [16, 17], and fibroblasts interact at long range through their structural remodeling of fibrous extracellular media [18, 19].

The substrate-mediated elastic interactions between such cells has important implications for biological processes such as self-organization during blood vessel morphogenesis [20] and synchronization of beating cardiac muscle cells [16, 21, 17, 22]. The overall motility of spatially separated cells is expected to depend on cell–cell mechanical interactions. This is revealed by experimental observations of substrate stiffness-dependent interactions of pairs of motile cells [23, 24]. These are the fundamental motivations by which we construct our models in chapters 2-4.

1.2.2 Molecular motors and cytoskeletal filaments

As briefly mentioned in the previous section, molecular motors are proteins which consume ATP to “walk” along cytoskeletal filaments. While the molecular motor that was highlighted in the previous section was the force-producing myosin II which has the tendency to oligomerize into large bipolar aggregate structures, another motor which walks preferentially along filaments, in this case microtubules, is kinesin. Unlike the aforementioned myosin molecule, kinesin does not form aggregates. In the cell, the motile end of the kinesin - called the heavy chain - binds to a microtubule and walks toward the plus end of the filament while the non-motile end - called the light chain - binds to various cargo. It is by this mechanism that several directed intracellular transport functions, such as centriole positioning [25], endocytosis and exocytosis [26, 27], and axonal transport [28] are executed.

While the roles that the varieties of these motor families play in various specific complex biological processes remains an ongoing field of study, *in vitro* experimental systems called gliding motility assays were built to peer deeper into the fundamental dynamics of motor-filament transport. Microtubule gliding motility assays are experiments in which kinesin motors are made to have their light chain bind to a surface - usually glass for a stationary distribution or lipids to study the effects of surface diffusion. Microtubule filaments, cytoskeletal biopolymers comprised of cylindrically stacked protofilaments - strings of alternating α and β tubulin monomers, are then placed in an accompanying solution and the system is supplied ATP. With all these components present, kinesins will bind to the microtubules and, since they cannot translate, push the microtubules around as they hydrolyze ambient ATP.

While it is known that these systems form polar - global direction of microtubule alignment and motion characterized by a vector - and nematic - global direction of microtubule alignment and motion characterized by a double headed vector called a director - states and exhibit rich dynamic laning behavior, recent experiments in both dense and dilute gliding assays show an inherent or emergent chirality. Microtubules in both seem to rotate in a preferred direction. Depending on the number of protofilaments that make up the microtubule, the protofilaments may be oriented along the long axis of the microtubule, as in the case of thirteen protofilaments called MT 13. If, however, the number of protofilaments deviates from thirteen, the protofilaments have a shallow helical wrapping whose direction depends on whether there are more or less than thirteen protofilaments present. The action, then, of a kinesin motor which predominantly walks along one protofilament would be that of an applied force on the microtubule at the angle of the helical wrapping. This is the fundamental assumption we use to build our model in chapter 5.

1.3 Methods

1.3.1 Brownian dynamics

Biological motion at the microscale is stochastic, due to the strong effect of thermal fluctuations. For example, a micron scale particle in an aqueous environment undergoes random Brownian motion due to collisions from water molecules. Writing Newton's second law most generally for a stochastic point particle we have the following force balance equation

$$m\ddot{\mathbf{r}} = \mathbf{F} - \zeta\dot{\mathbf{r}} + \sqrt{2\eta k_B T}\mathbf{W}(t), \tag{1.1}$$

which is comprised of a term representing inertia, $m\ddot{\mathbf{r}}$, where m is the mass of the particle and $\ddot{\mathbf{r}}$ is its acceleration, a sum of external forces, $\mathbf{F}$, a term representing dissipative effects, $\zeta\dot{\mathbf{r}}$, where ζ is a drag coefficient and $\dot{\mathbf{r}}$ is the velocity of the particle, and a stochastic term where k_B is the Boltzmann factor, T is temperature, and $\mathbf{W}(t)$ is typically a Gaussian white noise term for thermal motion, that satisfies $\langle W_i(t)W_j(t')\rangle = \delta_{ij}\delta(t-t')$, where $\delta(t)$ is the Dirac delta function and δ_{ij} is the Kronecker delta function. The Reynolds number, written $Re = \frac{\rho u L}{\mu}$, where ρ is the density of the fluid, u is velocity, L is a characteristic length scale, and μ is the dynamic viscosity, is a dimensionless quantity that represents the ratio of inertial to viscous forces. Taking the example of a cell, where the movement speed is on the order of $\frac{\mu m}{min}$ and the length scale is on the order of $10\mu m$, using the density and viscosity of water yields a Reynolds number of 10^{-7}. In many microbiological environments - including all those inspiring the coming studies - the Reynolds number is much smaller than unity meaning drag is a far more dominant force than inertia. It is appropriate then to drop the inertial term which allows us to rewrite eqn.1.1, having solved for velocity, as

$$\dot{\mathbf{r}} = \frac{1}{\zeta}\mathbf{F} + \sqrt{2D}\mathbf{W}(t), \tag{1.2}$$

where D is a diffusion coefficient. Equation 1.2 is the general equation of motion describing Brownian dynamics - or overdamped Langevin dynamics. It is this framework of dynamics that we use for all forthcoming chapters.

1.3.2 Continuum mechanics and Elasticity

Continuum mechanics is the field of study which seeks to understand and mathematically describe deformations of continuous material, whether it be flow of a patch of fluid, or displacement of a patch of solid. In all forthcoming chapters of this work, we draw heavily from the framework of elasticity theory - a subset of solid continuum mechanics which assumes completely reversible deformations with fast relaxation dynamics as opposed to viscoelasticity or plasticity [29].

Elasticity is concerned primarily with the relationship between an applied force on a material and its resulting deformation. This is usually presented as relating *stress* - the force per unit area - to *strain* - the relative non-dimensional change in length, and can be written most generally in einstein notation as

$$\sigma_{ij} = c_{ijkl}\epsilon_{kl}, \tag{1.3}$$

where σ_{ij} is the second order stress tensor, ϵ_{kl} is the second order strain tensor, and c_{ijkl} is the fourth order stiffness tensor. These tensors are symmetric by conservation of angular momentum balance. While in general the stiffness tensor could be comprised of many terms, using symmetry arguments and assumptions about the media, one can rewrite eqn. 1.3 in an explicit, simple, and separable way. Specifically, if one assumes as we do in chapters 2 and 4 that the material is isotropic - meaning the stiffness in all directions is identical - and homogeneous - meaning no volume element of the material is different from any other - then the stiffness tensor can be described by two quantities such that the strain as a function of stiffness, where the Einstein summation convention is used for repeated indices, can be written

$$\epsilon_{ij} = \frac{1}{E}[(1+\nu)\sigma_{ij} - \nu\delta_{ij}\sigma_{kk}], \tag{1.4}$$

where E is the Young's modulus given by $E = \frac{\sigma}{\epsilon}$ where σ is an axial stress and ϵ is the resultant axial strain and ν is Poisson's ratio written $\nu = -\frac{\epsilon_{trans}}{\epsilon_{axial}}$. The former quantity tells us how much deformation we get out of a given applied force - high E means small deformation in response to large force, *i.e.*, a rigid material. The latter quantity reveals to what extent the material is volume preserving. A cube which is volume preserving when stretched along one axis by an amount ΔL must compress along the other axes by an amount $\frac{\Delta L}{2}$ ($\nu = -\frac{-\Delta L}{2\Delta L} = \frac{1}{2}$) whereas a cube which is not volume conserving when stretched along an axis may well not compress at all along the other axes ($\nu = 0$). It is by these limiting cases that it is typically said that physical value of Poisson's ratio varies from 0 to 0.5, however, several materials including engineered systems like metamaterials can be geometrically designed to produce effectively negative Poisson's ratio [30].

Lastly, in chapters 2 and 4 we assume point-like anisotropic dipolar forces in an infinite half-space. The former means that we can write the displacement field directly as the product of the applied force and a response function - called a Green's function in the following way

$$u_i = G_{ij} \partial_k P_{jk}, \tag{1.5}$$

where $\mathbf{u}$ is the displacement, G_{ij} is the Green's function that captures the displacement in the elastic medium at the location of one cell (dipole) caused by the application of a point force at the location of the other [29], and $\mathbf{P}$ is the dipole moment [31]. The infinite half-space geometry provides boundary conditions that affords us the ability to write down the Green's function as

$$G_{ij} = \frac{1+\nu}{\pi E} \left[(1-\nu) \frac{\delta_{ij}}{r} + \nu \frac{r_i r_j}{r^3} \right], \tag{1.6}$$

where **r** is the vector coordinate with respect to the center of the dipole.

1.3.3 Agent-based modeling

Agent-based modeling is the approach of explicitly simulating agents or particles and the dynamics and interactions therein. As opposed to a continuum approach wherein an average observable quantity - typically a concentration - is discretized by a gridding schema and whose dynamics are determined by solving continuity constraints, in agent-based simulations, the corresponding equations of motion whose terms maybe physical or otherwise are applied to every individual particle comprising the simulation. While the benefits of continuum modeling - namely the ability to solve complex equations and extrapolate potent macroscopic data for large systems in a reasonable time - is very powerful, we utilize agent-based methods for all forthcoming models and simulations.

We chose this approach in chapters 2-4 because we wanted to construct our system such that the smallest length scale was the coarse-grained cell itself and corresponding dipole moment and the collective phenomena to emerge from the competition between stochasticity, motility, and substrate-mediated interactions alone. We chose this approach in chapter 5 because we were most interested in teasing out the dynamics of a single noisy filament with a focus on the effect of off-axis propulsion which is itself the coarse graining of an assumed sea of ambient motors.

Chapter 2

Optimal mechanical interactions direct multicellular network formation on elastic substrates

This chapter has been reprinted per the rights and permissions policy of the Proceedings of the National Academy of Sciences [32]. Note that all original experimental images are the work of our collaborator Jose E. Zamora Alvarado in the McCloskey lab. Portions of the introduction have been moved to the introduction of the dissertation.

2.1 Abstract

Cells self-organize into functional, ordered structures during tissue morphogenesis, a process that is evocative of colloidal self-assembly into engineered soft materials. Understanding how inter-cellular mechanical interactions may drive the formation of ordered and functional multicellular structures is important in developmental biology and tissue engineering. Here, by combining an agent-based model for contractile cells on elastic substrates with endothelial cell culture experiments, we show that substrate deformation-mediated mechanical interactions between cells can cluster and align them into branched networks. Motivated by the structure and function of vasculogenic networks, we predict how measures of network connectivity like percolation probabil-

ity and fractal dimension, as well as local morphological features including junctions, branches, and rings depend on cell contractility and density, and on substrate elastic properties including stiffness and compressibility. We predict and confirm with experiments that cell network formation is substrate stiffness dependent, being optimal at intermediate stiffness. We also show the agreement between experimental data and predicted cell cluster types by mapping a combined phase diagram in cell density substrate stiffness. Overall, we show that long-range, mechanical interactions provide an optimal and general strategy for multi-cellular self-organization, leading to more robust and efficient realization of space-spanning networks than through just local inter-cellular interactions.

2.2 Introduction

The morphogenesis of biological tissue involves the organization of cells into functional, self-assembled structures [33]. The aggregation of cells into ordered structures requires effectively attractive cell–cell interactions [34]. An example of such a process that is relevant to biological development, disease and tissue engineering, is the morphogenesis of blood vessels. This is initiated by patterned structures of endothelial cells (ECs), which align end to end to form elongated chains that intersect to give a branched morphology. Although the conditions required for vascular-like development in engineered *in vitro* systems are well established and EC vascular networks have been mathematically modeled using various approaches [35, 36, 37, 20, 38, 39, 40], the nature of the cell–cell interactions that drive the ECs to find each other to form networks and the dependence of these interactions on matrix stiffness have not been definitively identified.

The emergence of complex structures from the interactions of individual agents bears resemblance to colloidal self-assembly. For example, dipolar particles, such as ferromagnetic colloids, will align end-to-end into equilibrium, linear structures such as chains or rings [41]. At higher densities, the chains intersect to form gel-like network structures [42]. Such structures have been studied in simulation in the context of active dipoles representing synthetic active colloids endowed with a permanent or induced dipole moment [43, 44, 45] and swimming microorganisms [46] such as magnetotactic bacteria [47]. Animal cells that adhere to and crawl on elastic substrates and interact through mechanical deformations of the substrate [48] are also expected to attract and align to form multicellular structures [49]. Such mechanically directed self-organization of cells into functional structures, such as vascular networks, implies that network morphology depends on substrate stiffness.

Cells sense substrate mechanical deformations through mechanotransduction occurring at the biomolecular scale [50]. Such cellular signaling is carried out by proteins associated with the cell–substrate adhesions, that are in turn connected to the cell's cytoskeletal force-generating machinery [13]. At a coarse-grained level, the contractile apparatus of cells adhered to an extracellular substrate can be modeled as active elastic inclusions [51], which adapts the theory of material inclusions developed by Eshelby [52], to describe cellular contractility as force dipoles embedded in an elastic medium. This general theoretical approach predicts how multicellular and subcellular cytoskeletal organization depend on substrate stiffness [49, 53]. It has been applied successfully to explain experimental observations of substrate stiffness-dependent structural order in a variety of cell types in a unified manner [54, 55, 56, 21, 57]. While these previous works focused on the stationary configurations of elastic dipoles in the context of adherent cells [31, 58], we now consider cell self-assembly when the cellular dipoles are free to translate and rotate in response to mechanical forces, thereby serving as minimal models for contractile cells that adhere to, spread and crawl on soft media. We show that cell–cell mechanical interactions mediated by a compliant elastic substrate can drive network formation and that the resulting network morphology is inherently sensitive to substrate stiffness.

Coarse-grained material properties of the cellular micro-environment, such as its stiffness and viscosity, are known to play crucial roles in determining cell structure and function [50, 5, 59], including for bacterial colonies [60]. Recently, it was shown that human umbilical vascular endothelial cells (HUVECs) assemble into networks on softer substrates ($E \sim 1$ kPa) but fail to do so on stiffer substrates (Fig. 2.1a), independently of the type of hydrogel used [61]. In contrast, it was shown in ref. [62] that, under certain conditions, bovine endothelial cells formed networks preferentially on stiffer substrates

($E \sim 10$ KPa). Both these experiments show that EC network formation is sensitive to substrate stiffness, and therefore suggest that cell mechanical interactions mediated by the substrate are involved.

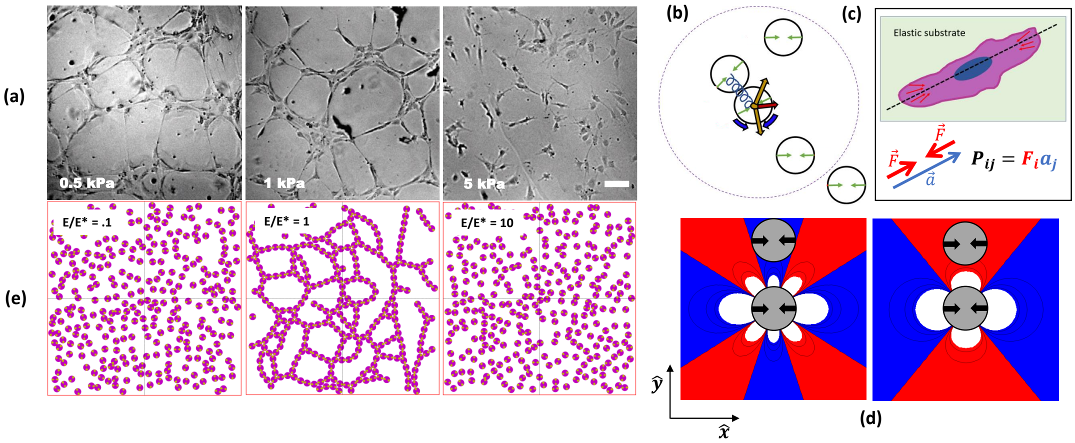

Figure 2.1: Cell network formation is optimized by substrate stiffness. (a) Human umbilical vascular endothelial cells (HUVECs) cultured on polyacrylamide hydrogel substrates of varying stiffness that were coated with Matrigel. At high stiffness (5 kPa and glass), the cells did not form networks but did so on softer substrates (0.5 and 1 kPa). Scale bar = $100\ \mu\mathrm{m}$. Images reprinted with permission from ref. [61]. (b) Cartoon of a simulation snapshot where green arrows indicate the cell's force dipole, the large purple dashed ring denotes the elastic interaction range, the blue squiggle indicates a repulsive spring to prevent overlap, bold gold arrows represent force vectors due to elastic interactions, the bold red arrows represent the net force vector on the central cell, the bold blue arrow represents torque on central cell due to elastic interaction with neighbors. (c) Cartoon cell deforming the surrounding elastic substrate by applying forces along a main axis. (d) u_{xx} component of the strain field caused by a contractile force dipole centered at the origin pinching along the x-axis for ν = 0.5(left) and ν = 0.1(right) with coordinate axes labeled. (e) Simulation snapshots of 300 cells modeled as contractile force dipoles that move and reorient according to substrate-mediated cell–cell elastic interaction forces. Cells form percolating networks only for a range of substrate stiffness values centered around an optimal stiffness, E^*, above which cells exert maximal traction force. For substrates around optimal stiffness ($E/E^* \sim 1$), the substrate-mediated cell–cell elastic interactions are maximal and can be much larger than the noise in cell movements, whereas for very soft ($E/E^* \ll 1$) or very stiff ($E/E^* \gg 1$) substrates, the elastic interactions are likely to be overwhelmed by noise, resulting in a lack of ordered structures.

2.3 Model and Results

2.3.1 Substrate stiffness-dependent endothelial cell network organization motivates model for cell mechanical interactions.

To model cell network formation, we incorporate substrate-mediated cell mechanical interactions into an agent-based model for cell motility [63]. This captures the dynamic re-arrangements of cells into favorable configurations. In our agent-based approach [64, 65], summarized in Fig. 2.1b, we consider a system of N particles, each a disk of diameter d. Depending on the context, each disk could model a cell or its constituent parts, and their motion represents both cell migration as well as cell spreading, or shape change dynamics. Details of the cell shape are not included in this minimal model. These model cells self-organize according to substrate friction-dominated overdamped dynamics that depend on inter-cell interactions, as well as individual cell stochastic movements described by an effective diffusion. The model incorporates both short-range, steric and long-range, substrate-mediated elastic interactions between cells, and is detailed in the Methods section.

The ubiquitous traction force pattern generated by a single polarized cell with a long axis $\mathbf{a}$ and exerting a typical force $\mathbf{F}$ at its adhesions, can be modeled as a force dipole, $P_{ij} = F_i a_j$ (Fig. 2.1c). Note that the cell traction forces are generated by actomyosin units within the cell, each of which acts as a force dipole. Therefore, the disks in our model simulations could represent parts of a cell, and their motion represent the dynamics of cell protrusions. The resulting deformation induced by a force dipole in the elastic substrate is given by the strain, u_{ij}, which is determined by a force balance in linear elastic theory (see SI section A.1), and depends on the material properties of the elastic medium, specifically, the stiffness or Young's modulus E, and the compressibility, given by the Poisson's ratio ν [29]. The substrate deformation (u_{xx} component of strain) generated by a dipole (oriented along the laboratory x-axis) embedded on the surface of a linear elastic medium is shown in Fig. 2.1d for two representative values of ν. Here, the blue (red) coloring represents expanded (compressed) regions of the substrate. We note that the extracellular matrix in biological tissue is typically viscoelastic, and over long times the cell-generated strains may relax. However, our model still applies at short time scales and for linearly elastic synthetic substrates such as polyacrylamide that are routinely used in cell culture experiments [11].

A second contractile force dipole will tend to position itself in and align its axis along the local principal stretch in the medium to reduce the substrate deformation. The resulting interaction potential arises from the minimal coupling of one dipole (denoted by β) with the medium strain induced by the other (denoted by α), and is given by $W^{\alpha\beta} = P^{\beta}_{ij} u^{\alpha}_{ij}$[48]. The interaction energy between two dipoles then decays with their separation distance as $W^{\alpha\beta} \sim (P^2/E) \cdot r^{-3}_{\alpha\beta}$. We denote the characteristic elastic interaction energy when the dipoles are separated by only one cell length as, $\mathcal{E}_c = P^2/(16Ed^3)$, where the detailed expression is derived in the SI Section A.1. This coarse-grained description abstracts out the biophysical details of mechanotransduction, but provides a simple physical model for the cell response to deformations in their elastic medium [49].

Representative simulation snapshots (Fig. 2.1e) of final configurations show that elastic dipolar interactions induce network formation in a stiffness-dependent manner. The central snapshot corresponds to an optimal substrate stiffness E^* at which elastic interactions are maximal, while those to the left (right) correspond to substrates that are too soft (stiff) for connected network formation. The origin of this optimal stiffness lies in the adaptation of cell contractile forces to their substrate stiffness, as we discuss later.

2.3.2 Elastic dipolar interactions between model cells induce network formation

We expect the multicellular structures resulting from the dipolar cell–cell interactions to depend on three crucial nondimensional combinations of model parameters: the ratio of a characteristic elastic interaction energy $\mathcal{E}_c$, to noise – denoted by $A = \mathcal{E}_c/k_B T_{\text{eff}}$ – the effective elastic interaction parameter; the number of cells N, equivalently expressed as a cell density or packing fraction, $\phi = \frac{\pi N d^2}{4L^2}$; and Poisson's ratio, ν, which determines the favorable configurations (both position and orientation) of a pair of dipoles. To show the types of multicellular structures that result from our model elastic interactions, we perform Brownian dynamics simulations (detailed in *Methods*) to generate representative snapshots at slices of this $A - \phi$ parameter space for two val-

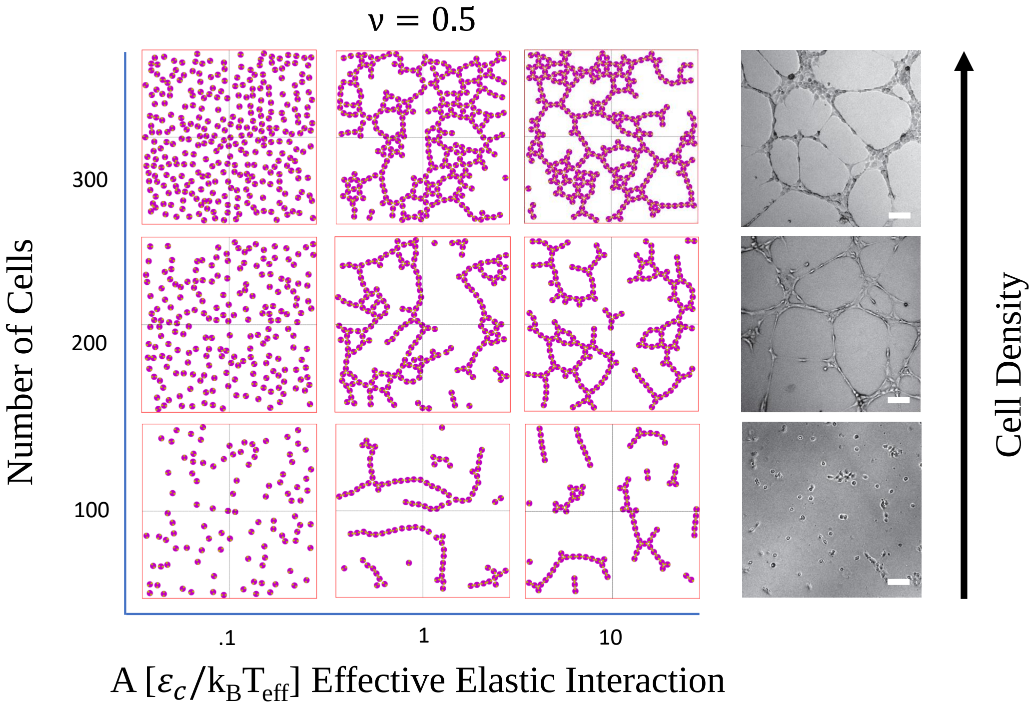

Figure 2.2: Simulation snapshots showing representative final configurations of model cell dipoles. We explore the parameter space of number of cells and $A \equiv \frac{\mathcal{E}_c}{k_\mathrm{B} T_\mathrm{eff}}$, the ratio of the characteristic elastic interaction strength and noise, for Poisson's ratio, $\nu = 0.5$. At lower packing fractions, cells form disconnected linear clusters. At lower A values, cells remain isolated, but at moderate values of A and sufficient packing fraction, cells form space spanning network configurations characterized by rings, branches, and junctions. At higher packing fractions, clumpy structures such as what previous literature calls ”4-rings” occur frequently [58]. The tendency for cells to form only local connections at low packing fraction and form space spanning structures at higher packing fraction is consistent with experimental images of endothelial cells cultured on hydrogel substrates (right column; images reprinted with permission from Ref. [61]). Scale bars: $100 \mu m$.

ues of ν; 0.5 and 0.1 shown in Figs. 2.2 and SI Fig. A.4, respectively. As packing fraction is increased, networks form more readily. As the effective elastic interaction is increased, cells form into networks characterized by chains, junctions, and rings. This can be thought of naturally as a competition between entropy and energy. At low packing fractions or effective elastic interaction, cells are either in a gas-like state or form local chain segments with many open ends which have high entropy. As packing fraction or effective elastic interaction increases, cells relinquish translational and rotational freedom for more energetically favorable states such as longer chains, junctions, or rings. This is consistent with the cell density dependent morphologies seen in images from *in vitro* hydrogel experiments (reproduced from Ref. [61]), and shown in Fig. 2.2.

We choose two representative values of ν in our model simulations because their corresponding strain plots are qualitatively different [31] as seen in Fig. 2.1d. Briefly, since contractile dipoles prefer to be on stretched regions of the substrate, the low (high) ν deformation patterns are expected to favor two (four) nearest neighbors. The different values of Poisson ratio could correspond to synthetic hydrogel substrates and the fibrous extracellular matrix, respectively. While hydrogel substrates are nearly incompressible ($\nu = 0.5$), the ECM comprises of networks of fibers which permit remodeling and poroelastic flows leading to reduced material compressibility (e.g., $\nu = 0.1$) at long time scales [66].

2.3.3 Substrate deformation-mediated interactions strongly enhance percolation in model networks

To characterize the extent of multi-cellular network formation, we consider the percolation order parameter which quantifies the ability of a connected network to span the available space. Percolation is defined as the probability that, for a steady state realization of the network, there exists a continuous path through it that spans the length of the simulation box. To compute percolation probability, we first identify connected clusters of cells, a process detailed in SI section A.3. A specific network configuration is considered to be percolating if any two cells within the same cluster are separated by a Euclidean distance greater than or equal to the simulation box size. The average values and corresponding errors (forty simulations per data point) are then plotted against varying packing fraction ϕ in Fig. 2.3a and varying effective elastic interaction parameter A in Fig. 2.3b. Multiple such simulations are then combined into a phase diagram in $A-\phi$ parameter space in Fig 2.3c. The results show that percolation requires both density and interaction strength to be above corresponding threshold values.

To contrast with the dipoles that mutually align through long-range and anisotropic interactions, we consider a control system of “diffusing sticky disks”. These agents

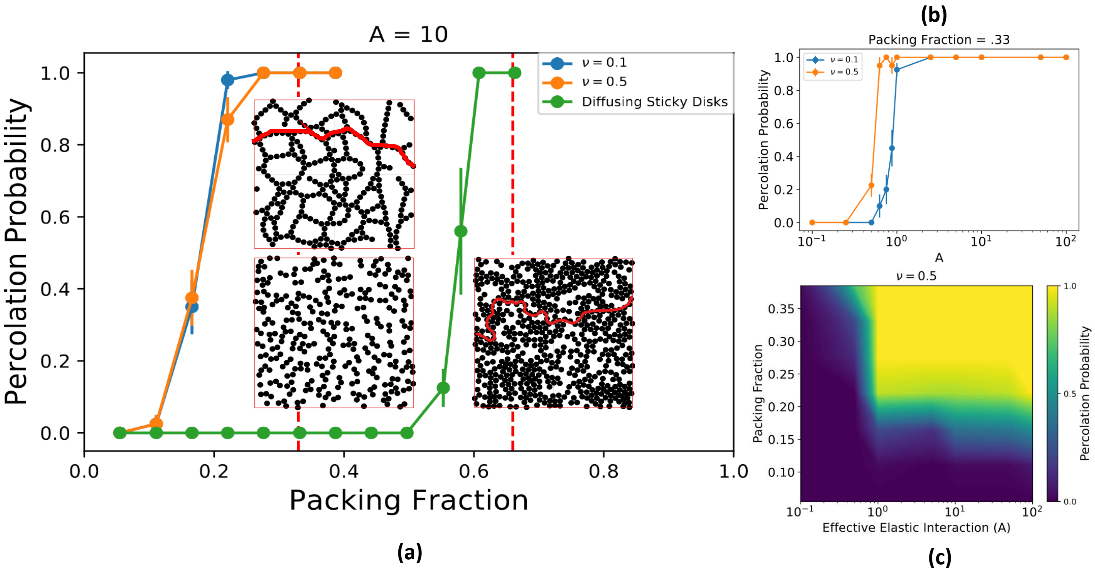

Figure 2.3: Analysis of connectivity percolation of simulated cell clusters predicts dependence on cell density and strength of substrate-mediated elastic interactions. (a) Percolation probability for elastic dipoles - blue and orange - and diffusing sticky disks - green - as a function of area packing fraction, ϕ. Elastic dipoles undergo the percolation transition at lower packing fractions than purely diffusive, sticky disks. The insets show characteristic final configurations for both elastic dipoles and sticky disks at a packing fraction of $.33 (N = 300)$, with an example percolating path shown in red. (b) The percolation probability for given packing fraction also exhibits a sharp transition in effective elastic interaction, A. (c) Percolation phase diagram in packing fraction and effective elastic interaction space. Generally, network assembly is more likely for higher cell density and elastic interactions. Each data point and error bar represents the average and standard error of the mean (SEM), respectively, of forty simulations with the exception of sticky disks in (a) at the three largest packing fractions which represent nine simulations each, and A = 0.25, 0.625, 0.75, 0.875, and 2.5 in (b) which represent twenty simulations each.

just diffuse without any long-range interactions and cease movement upon contact with another agent. We find percolating networks for both interacting elastic dipoles and diffusing sticky disks. However, Fig. 2.3a shows model cells which interact as dipoles at long-range require far fewer cells to percolate than their sticky disk counterparts given that the elastic interaction strength is sufficiently greater than noise as shown in Fig. 2.3b ($A \gtrapprox 1$ in the case shown where $N = 300$). This is because the anisotropic nature of the dipolar interactions promotes end-to-end alignment of cells, creating elongated structures like chains, which can self-assemble into space-spanning networks. We therefore show that network formation requires fewer cells when cells can sense, move and align in response to the substrate deformations created by other cells. Thus, networks guided by mechanical interactions are more cost efficient than when cells move or spread randomly, forming adhesive contacts upon finding their neighbors.

Much work has been done on characterizing the connectivity percolation transition on various lattice configurations [67]. The critical packing fraction can be widely different depending on the lattice geometry, and whether the space-spanning clusters comprise sites or bonds [68, 69]. The critical packing fraction for site percolation is known to be $\phi_C = 0.5$ for an infinitely large triangular lattice [70]. In approximate agreement with this, we find that the critical packing fraction for diffusive sticky disks for the current finite system size L is $\phi_C \approx 0.6$. For the dipolar particles, anisotropic interactions shift the percolation transition to $\phi_C \approx 0.2$, similar to those seen in dipolar colloidal assemblies at low reduced temperature [71].

Our observed packing fractions for transition to percolation are specific to the simulation system size, L, and differ from the actual critical packing fraction due to finite size effects. How prominent these effects will be depends on the fractal dimension, which provides a measure of how these structures scale with size. Since area scales like L^2, but number of particles scales like L^{d_f}, where d_f is the fractal dimension, $\phi_C \propto L^{d_f - 2}$. Therefore, there exists a regime in which ϕ_C will decrease with increasing L, as shown by simulations with bigger box sizes (see SI section A.4). We present an analysis of the fractal dimension of these networks and corresponding experiments in the next section.

2.3.4 Analysis of experimental cell cultures confirms predicted substrate stiffness dependence of cell network formation

We showed in the previous section that the cells' ability to form networks is expected to depend on the strength of elastic interactions arising from their mutual deformations of the substrate. To compare with experiments, we now consider how this elastic interaction strength A depends on the substrate stiffness. Experiments show that cells spread and polarize more on substrates of increasing stiffness, such that their traction force saturates to a maximal value P_0 at a characteristic substrate stiffness, E^*, that depends

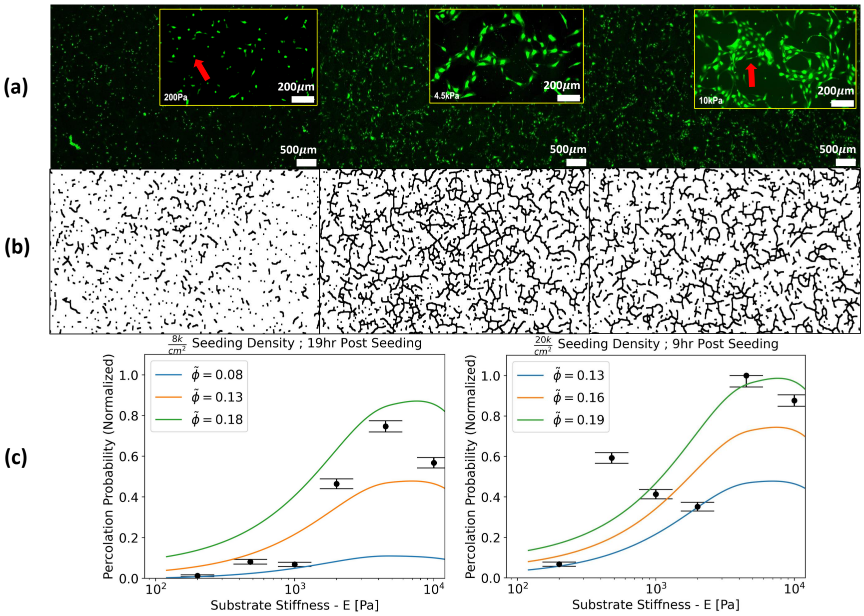

Figure 2.4: Analysis of connected clusters of endothelial cells cultured on elastic substrates reveals optimal stiffness for cell network formation (a) Experimental images of human umbilical vascular endothelial cells (HUVECs) at 8×10^3/cm^2 seeding density 19 hours post seeding on polyacrylamide substrates of varying stiffness: 200kPa (left), 4.5kPa (middle), and 10kPa (right). Insets show $10\times$ magnified images of the full field of view. Cells on substrates of lower stiffness tend to remain largely isotropic and isolated (shown by red arrow on the left), and do not form inter-cellular connections. Cells on substrates of higher stiffness tend to spread and aggregate into dense isotropic clusters (shown by the red arrow on the right). Both these tendencies counteract efficient network assembly. (b) Processed binary skeletons of the raw images in (a). Qualitatively, the intermediate substrate stiffness exhibits the most prominent networks. (c) Quantitative measurement of the percolation probability from experimental images such as shown in (b) support the model prediction that network formation is optimal on substrates of intermediate stiffness. Left and right plots show normalized percolation probability values measured for two different initial cell seeding densities, 8×10^3/cm^2 and 20×10^3/cm^2, respectively. The higher density cell culture data (right) is selected at an earlier time (9 hours post seeding) because these cells form dense isotropic clusters at later times. The continuous curves represent model predictions for percolation probability as a function of substrate stiffness at three different representative values of the packing fraction from skeletonized simulation images, $\tilde{\phi}$. These are chosen to approximately correspond to the experimental packing fraction, which however varies with substrate stiffness due to cell spreading. Percolation curves from simulation in (c) were interpolated from average values obtained for forty simulations. Experimental data points and error bars are average and standard error of the mean (SEM), respectively, of subboxes as described in *Methods*.

on cell type and matrix mechanochemistry. The effective elastic interaction parameter, A, can be mapped to substrate stiffness, E, by using a model relation predicting the dependence of cell traction force on substrate stiffness [72]: $P = P_0E/(E + E^*)$. The resulting elastic interaction parameter, A, is weak on softer substrates where cell forces are low and also on stiffer substrates, where the deformations are low. It reaches a maximum at the characteristic stiffness E^* as detailed in SI section A.5. This mapping from effective elastic interaction to substrate stiffness (SI Fig. A.6) results in a peak in the percolation curves (SI Figs. A.8a and A.8c) over an interval of substrate stiffness centered around the optimal stiffness E^*. This interval depends on both cell density and effective temperature representing noisy cell movements. Higher effective temperature and lower cell density reduce both peak height and width. This result is consistent with experiments on EC cultures (Fig. 2.1a) which show that percolating networks form only in a certain range of substrate stiffness, but these previous works do not demonstrate that network formation is optimal at intermediate substrate stiffness [62, 61].

To test this prediction of our model, we performed 2D cell culture experiments on elastic substrates over a wide range of stiffness values. Human umbilical vascular endothelial cells (HUVECs) were cultured at three different seeding densities (8×10^3/cm^2, 14×10^3/cm^2, and 20×10^3/cm^2) on fibronectin-coated polyacrylamide substrates of varying stiffness: (200 Pa, 480 Pa, 1 kPa, 2 kPa, 4.5 kPa, and 10 kPa). The substrate preparation protocol, described in *Methods*, and stiffness characterization of these substrates follow standard precedents [73]. Cells were fluorescently labeled and imaged at regular intervals over the course of 19 hours post-seeding. While for the lower seeding density, network formation could be observed at these longer time scales (Fig. 2.4a, middle), the higher seeding density led to denser, isotropic clusters and a resulting loss of network morphology (Fig. 2.4a, right). We then considered the images of these denser cultures at 9 hours instead of 19 hours, where network morphology was still apparent. We also observed that the dense isotropic clusters were more prevalent at higher substrate stiffness due to enhanced cell spreading and possibly proliferation at later times.

To quantitatively obtain the percolation probability for the observed cell clusters, we process the experimental images (Fig. 2.4a) by emphasizing inter-cellular connections as described in *Methods* under *Image Analysis*. We then parse the resulting binary images (Fig. 2.4b) into $N_B = 312$ sub-boxes each so as to obtain sufficient statistics from a single experimental image. We next computed the mean percolation probability over all sub-boxes, $p = \frac{1}{N_B} \sum_{i=1}^{N_B} p_i$ and the corresponding standard error of mean. Here, we set $p_i = 1$ if the i^{th} sub-box is "percolating" *i.e.* it contains a cluster that spans the sub-box, and set $p_i = 0$ otherwise. To compare the sparser, heterogeneous experimental configurations with our simulated networks, we normalized these values by the maximum mean percolation probability across all experimental seeding densities and stiffnesses. For practical convenience, we henceforth denote the normalized percolation probability value as p.

We find that for both the lowest seeding density sampled at long times (Fig. 2.4c - left) and for the highest seeding density sampled at short times (Fig. 2.4c - right), the normalized experimental percolation probability exhibits a peak at a stiffness of about 4.5 kPa. Unlike simulations where packing fraction and elastic interaction are independent parameters, the area covered by cells in experiments depends on stiffness because cells spread more on stiffer substrates. This is why we need a range of packing fraction values from simulation to compare with experiment. Like the experimental images, the simulation images were skeletonized to emphasize inter-dipole connection (see *Methods*, *Image Analysis*). We denote the corresponding packing fraction of skeletonized images by $\tilde{\phi}$ to distinguish from the packing fraction of simulated disks, ϕ. We then plot a family of interpolated simulation curves as a function of substrate stiffness over a range of packing fraction values, $\tilde{\phi}$, chosen to fit the experimental data in Fig. 2.4c. These values are close to the range of packing fraction values in experimental images (.05-.15 for $\frac{8k}{cm^2}$ and .1-.2 for $\frac{20k}{cm^2}$). The quantitative agreement of the experimental data with simulation values lends credence to our model that network formation is driven by substrate mediated elastic interactions, and that these are stronger within a range of substrate stiffness values centered around an optimal value, E^*.

We note an important distinction between the predictions of the cell dipole model and the observed cell clusters in experiments. These latter tend to exhibit isotropic dense clusters on stiffer substrates at higher seeding density. We expect this is because cells spread more on stiffer substrates and form direct adhesive contacts with neighbors. Cell spreading and direct cell-cell contact-based interactions are not implemented in our minimal model, since we focus on the long-range substrate-mediated dipolar interactions expected to dominate in dilute cultures. At higher densities, endothelial cells are known to form confluent monolayers [74]. At intermediate densities, some of these dense isotropic clusters occur alongside networks and elongated structures. Modeling these would require a combination of cell-cell and cell-substrate forces. Although dense isotropic clusters are not seen in our dipole simulations (Fig. 2.1e), their occurrence in experiment supports our model prediction that the dipolar elastic interaction strength (A) becomes smaller on stiffer substrates in relation to the isotropic, cell–cell contact interactions.

While the percolation analysis shown in Fig. 2.4 validated our model predictions for the substrate stiffness-dependence of network formation, we now seek to predict characteristic morphological traits of the cell clusters. A careful examination of experimental images in Figs. 2.4 and 2.5 reveals distinct morphologies of cell clusters, ranging from isolated cells and isotropic clusters to networks and elongated clusters. To obtain a measure of how elongated each cell cluster is, we calculate a “shape parameter”, defined as $s \equiv \frac{R_g^2}{Area} = \frac{1}{N^2}\sum_{k=1}^{N}(\mathbf{r}_k - \mathbf{r}_{CM})^2$, for each unique cluster as described in *Methods* under *Image Analysis*. Here, R_g represents the radius of gyration of the cluster, which is defined about its center-of-mass $\mathbf{r}_{CM}$, and N is the number of occupied pixels in each cluster. The normalization by cluster area ensures that we control for cluster size variations between different experiments. Lower values of this shape parameter correspond to isotropic shapes, the theoretical lower bound being $\frac{1}{2\pi}$ for a solid circular disk. Conversely, a higher shape parameter corresponds to more elongated clusters. To compare with simulation, we scale the shape parameter of each cluster by their global means across all identified clusters at the different seeding densities and stiffnesses. Henceforth, the scaled values of the shape parameter are denoted by s.

To classify the dominant morphological feature in each image, we constructed a composite order parameter combining the global information of connectivity percolation with the local cluster-scale morphological characteristics captured by the shape factor. The order parameter is defined such that clusters with normalized percolation probability above a threshold value ($p_T = 0.7$) are considered “networks”. We choose this value of p_T to pick out experimental images where a few of the largest clusters contain more than twenty percent of the total filled area (SI Fig. A.9). If $p < p_T$, implying that there are no dominant space-spanning clusters, we classify clusters into “isolated” or “chains”, depending on whether s is less or greater than a threshold value $s_T = 0.95$. This value of s_T is chosen to correspond to simulations with two aligned dipoles, giving an elongated morphology that this parameter is designed to capture. The order parameter which accomplishes the above classification is given by OP $\equiv \Theta(p - p_T)p + \Theta(p_T - p)(.25 + .5(s - s_T))$, where $\Theta(x)$ is the Heaviside step function and the numerical factors give an $0 < OP < 1$ for the specific values of s_T and p_T, justified above. The differences are captured by ranges of values of the order parameter: $OP > 0.7$, $0.25 - 0.7$ and < 0.25 correspond to percolating “networks”, elongated but disconnected “chains”, and isotropic “isolated” clusters, respectively.

We compute this order parameter for interpolated simulation data and for experimental data 9 hours post seeding, so that cell proliferation effects are minimal. Experimental data once again reveals a non-monotonicity in network formation at the high densities in Fig. 2.5 - bottom left. We construct a phase diagram of this order parameter in $\tilde{\phi} - E$ space (Fig. 2.5 - center), where the color map corresponds to simulation data. Overlaid on this phase diagram are discrete markers representing experimental data, which have been classified into the three distinct regimes according to their measured order parameter values. The data comprises three initial seeding densities and five stiffness values giving a total of fifteen data points. Their distribution clearly shows a correlation between cell area coverage and substrate stiffness. This is due to cells spreading more on stiffer substrates, readily seen through the lack of low packing fraction data at higher stiffness.

Phase boundaries are drawn as dashed lines that delineate the distinct regions of the simulation order parameter values. Of the fifteen experimental data points, only two lie outside of the corresponding predicted regions. Both of these are at low substrate stiffness and intermediate packing fraction. These are classified as “chains”, but which lie in the “isolated” part of the predicted phase diagram. We expect that at these intermediate densities, cells can spread and touch each other to form elongated structures even if the elastic dipolar interactions are small. Since our model does not include such spreading effects, this discrepancy is not surprising. Overall, the model phase diagram closely

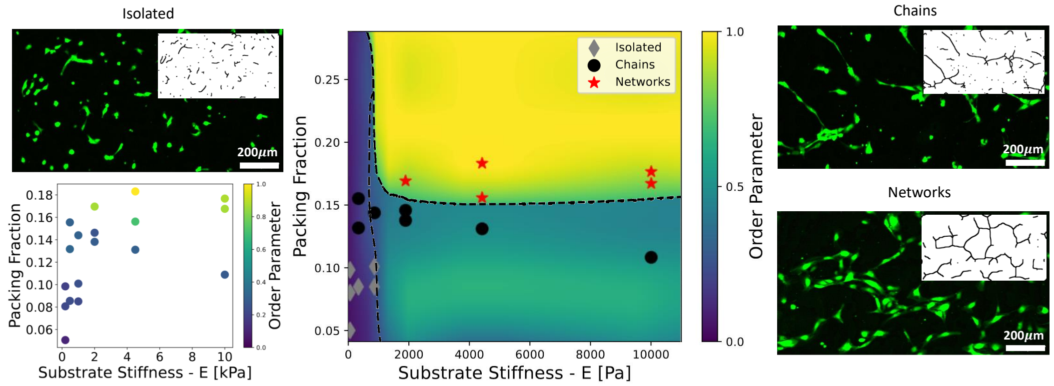

Figure 2.5: Experiments validate predicted classification of cell cluster morphology into distinct phases. (Center) “Phase diagram” of the distinct morphology of cell clusters, based on cell density and substrate stiffness. The color map represents a composite order parameter (OP, detailed definition in the text) designed to capture both the cluster percolation probability p and the cluster shape parameter s as a single value. Ranges of the order parameter values $OP > 0.7$, $0.25 - 0.7$ and < 0.25 correspond to percolating “networks”, elongated but disconnected “chains”, and isotropic “isolated” clusters, respectively. The background color map is created by interpolating over a set of order parameter values obtained from simulations of varying cell number (plotted as $\tilde{\phi}$ - the post-skeletonized filling fraction) and elastic interaction strength. The experimental data points, corresponding to different cell densities (measured as fractional area covered by cells in microscopy images) and substrate stiffness, are classified according to the measured value of the order parameter and overlaid on the simulated phase diagram. They demonstrate good agreement with the predicted phase boundaries (dashed lines). (Left - bottom) is the phase diagram showing the experimental order parameter values using the same color map as the simulation results in the central phase diagram. This reveals the non-monotonic behavior of the order parameter vs. substrate stiffness for the percolating networks, confirming the results of Fig. 4c. (Left-Top, Right-Top and Right-Bottom) show representative images from the cell culture experiments (at highest seeding density) and corresponding skeletonized images, to illustrate the occurrence of isolated cells, elongated chains and percolating networks for substrates of stiffness, 200 Pa, 480 Pa and 4.5 kPa, respectively. Simulation values used to construct the colormap in center panel are averaged over forty simulations for percolation and three simulations for shape factor for each data point.

predicts the experimentally observed multicellular structures.

We now further evaluate the morphological similarity of the networks from our simulated dipoles and our experimental cell culture by calculating the fractal dimension.

For the “sticky disks”, we find a fractal dimension of $d_f = 1.81$, whereas for the dipoles we find fractal dimensions of $d_f = 1.698 \pm .004$ and $d_f = 1.711 \pm .003$ for $\nu = 0.1$ and $\nu = 0.5$, respectively. We find a similar fractal dimension for our experimental HUVEC culture in the network regime on a substrate of stiffness $E = 4.5$kPa, $d_f = 1.722$. Interestingly, simulated networks on substrates of $\nu = 0.1$ and $\nu = 0.5$ are statistically distinguishable, with the experimental fractal dimension showing reasonable agreement with the $\nu = 0.5$ simulated dipole case. This is in accordance with the approximately incompressible nature of hydrogel substrates. The proximity of the fractal dimensions of the simulated dipoles to that of experimental cell networks, in relation to the sticky disks, indicates that cells utilize a more complex strategy to self-assemble than simply random movement followed by cell–cell adhesion. The elastic dipolar interactions are thus a plausible strategy allowing the self-assembly of biologically desirable, space-spanning and cost-effective networks.

2.3.5 Diverse Poisson-ratio dependent morphological features offer distinct advantages in network assembly and transport function

We now focus on simulated networks (such as in figure 2.3) to thoroughly characterize their two predominant network morphological constituents - branches and rings . We relate the resulting structural metrics to the transport function of biological networks. We highlight qualitative differences in morphology of simulated networks between high and low Poisson’s ratio values, which may motivate future experimental investigation. Fig. 2.6a shows average branch length for $N = 300$ ($\phi = 0.33$) cells as a function of effective elastic interaction (A). The average branch length for the higher ν case remains roughly constant and low at about two cell lengths. The lower ν case exhibits a peak in average branch length at the percolation threshold ($A = 1$) before decreasing and saturating at high A values. The distribution of branch lengths (Fig. 2.6b) shows that while $\nu = 0.5$ is sharply peaked at d, $\nu = 0.1$ exhibits branches greater than $18d$ and shows a greater relative count in the $3 - 10d$ range.

These results suggest that at higher values of ν, network morphology is more re-

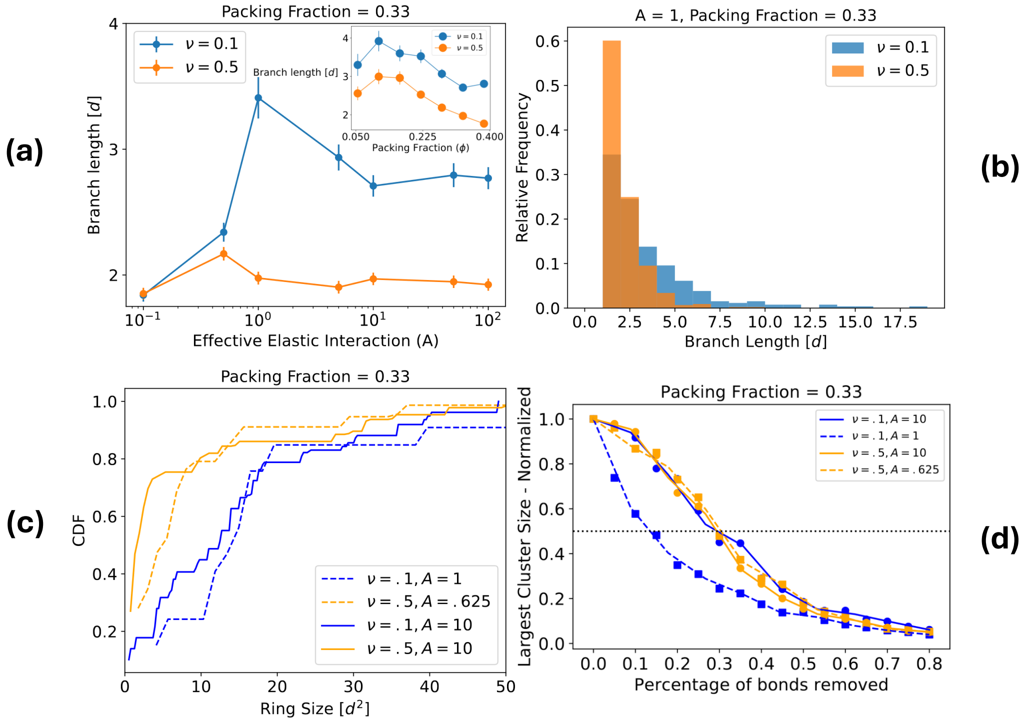

Figure 2.6: Substrate compressibility and rigidity affect efficiency and resilience of model networks. (a) Average branch length as a function of the effective elastic interaction for $N = 300(\phi \approx .33)$ cells. The lower ν case shows a greater sensitivity to A indicating a greater aptitude for tunability than the high ν counterpart. The inset shows average branch length as a function of packing fraction when $A = 10$. Both values of ν show similar behavior except at the highest point of packing fraction. At this packing fraction, the curves diverge as global configurations begin to become prevalent. For the low ν case, this will be long parallel strings whereas the high ν case will form a single cluster of 4-rings. (b) Normalized branch length histogram for $A = 1$ and $\phi = .33$. The networks on substrates of high ν are sharply peaked around the smallest branch lengths while the networks at low ν exhibit a broader, longer-tailed distribution. (c) Cumulative distribution of ring area for $N = 300(\phi \approx .33)$ cells shown both for networks at the shoulder of the percolation transition and networks well beyond the transition. Networks at high ν contain smaller rings than the networks at low ν. Irreversible networks show more smaller rings as noise is not great enough to jostle these compact structures apart to favor more stringy morphologies. (d) Largest cluster size as a function of the fraction of network branch segments removed - a measure of a network's ability to maintain functionality after being damaged [66]. Networks at the shoulder of the percolation transition exhibit less robustness than those well above the percolation transition for the $\nu = 0.1$ case. In the $\nu = 0.5$ case, however, networks retain their robustness even at the shoulder of the percolation transition. As this robustness metric saturates at a value of A dependent on the compressibility of the substrate, we hypothesize cells interacting in the way that we have estimated will tend to exert only a certain amount of force, enough to build a resilient network and no more. Each data point and error bar in (a)-(c) represent the average and standard error of the mean, respectively, of three representative simulations. Data points in (d) are averages of 20 trials per percentage of bonds.

silient to noise, and the branch lengths are not as easily tunable, The greater variability in branch lengths leads to longer branches in the lower $\nu = 0.1$ case, which then requires (for $A \geq 5$) fewer cells to percolate than at $\nu = 0.5$. This is seen by the difference of the curves at the shoulder of the percolation transition in Figs. 2.3a and SI Fig. A.10. The greater resilience of the network at higher substrate ν leads to percolation at smaller A than its low ν counterpart (Figs. 2.3b and SI Fig. A.10). In SI section A.7, we construct a detailed map of the percolation transition in the $A - \phi$ parameter space, to show how $\nu = 0.1$ requires fewer cells to percolate for a range of A values, while $\nu = 0.5$ can percolate at lower values of A. This suggests that the two regimes of substrate compressibility optimize two different measures of cost of network building: one, the number of cells, and the other, the strength of cell contractility.

Fig. 2.6c shows a cumulative distribution of ring area for our networks at two crucial regions in our parameter space – those at which the networks are well above the percolation transition (solid lines), or just above it (dashed lines). Similar to the branch length distribution, the networks at higher ν form many small rings and few large rings, while the lower ν case shows a broader distribution of ring sizes. The tendency of the $\nu = 0.5$ configurations to form numerous smaller rings leads to a marginally less efficient area coverage than the low ν case, which forms longer branches and fewer small rings (SI Fig. A.11). These results are also consistent with the fractal dimensions we obtained earlier, with d_f being slightly higher for the $\nu = 0.5$ than the 0.1 cases, indicating more compact structures for the former. These topological features also give rise to distinct coordination numbers for the two compressibility regimes (SI Fig. A.18). Interestingly, the coordination number on the lower Poisson ratio resembles those near the rigidity percolation of elastic fiber networks[75, 76]- indicating connectivity percolation as a precursor to mechanical rigidity which is relevant to both tissue development and disease [77].

To examine the robustness of our model networks to damage, a biologically significant property, we measure the largest remaining cluster size as a function of the fraction of network bonds removed [78] (Fig. 2.6d). We find that whether well above or just at the percolation threshold, the networks at higher ν retain cluster size well as bonds are removed. Networks at lower ν well above the percolation transition lose largest cluster size at the same rate as their higher ν counterpart. At the shoulder of percolation, however, networks at low ν lose largest cluster size and fall apart much more rapidly than any of the other networks. This is the same parameter regime in which networks at low ν exhibit a peak in branch length. By forming long branches, ring structure formation is sacrificed. Thus, we find that the prime factor for robust networks is the tendency to form rings which provide degeneracy to paths between any two nodes in the network - a result consistent with network structure optimization models [79]. In summary, at lower ν, networks tend to form longer and more broadly distributed branches which promote efficiency with respect to the filling and spanning of space at the cost of being susceptible to damage, while at higher ν, networks are predominantly composed of small rings, which provide robustness to the networks at the cost of transport efficiency.

2.4 Discussion

Our model generates testable predictions for the dependence of cell network morphology on substrate mechanical properties. By performing and analyzing experiments on ECs cultured on hydrogels of varying stiffness, we show that network formation is indeed optimized at an intermediate stiffness. Although many experiments show that EC network formation or capillary sprouting require softer matrices (Ref. [80] and references therein), these findings can show different trends at different stiffness regimes [81, 82]. We suggest that this may be because cells adapt their traction forces to substrate stiffness, and therefore, the expected optimal stiffness for network formation should be where cells attain their maximal contractility. This optimal stiffness may be dependent on cell type and matrix mechanochemistry [62].

Our modeling thus relates network structure to cell contractility, and the predictions can be further checked in cell culture experiments on substrates of varying stiffness and Poisson's ratio [66], that combine traction force measurement with quantification of network morphology. The presence of substrate deformation-mediated interactions can also be directly investigated in a two-cell setup on a micropatterned substrate which allows one to observe reorientations of one cell in response to the other, similar to strategies used to examine pairwise interactions during cell motility [83] and cardiomyocyte synchronization [17].

Further, cells may persistently migrate, in addition to the stochastic movements assumed in the present model. Our prior work suggests that cells form stable network structures rapidly at lower migration speeds [65]. At high persistent migration speeds, the networks dissolve and the dipoles self-organize instead into motile chains. This suggests that an optimum cell migration speed is favorable for network formation, which cells may achieve through self-regulation of their motility through interaction with their neighbors, such as contact-inhibition of locomotion.

A crucial modeling challenge for vasculogenesis, and other instances of cell network formation in biology, is that multiple factors ranging from cell differentiation to chemotactic cues could be involved *in vivo*. Modeling approaches based on different hypotheses can all lead to network pattern formation [84]. Here, by combining experiments on hydrogels of varying stiffness and a physical model based on mechanical interactions alone, we aim to isolate the different factors involved. While we focus on endothelial cell networks as a model system, our predictions are generally applicable to other contractile cell types that self-organize into networks such as fibroblasts [85], neurons or smooth muscle cells (Table 2.2), as well as to synthetic particles with electric or magnetic dipolar interactions, that are of interest in materials science.In summary, our work provides proof-of-concept that substrate-mediated elastic interactions is a physical strategy that biological cells may employ to direct their self-organization into efficiently space-spanning, multicellular networks.

2.5 Methods

2.5.1 Model details

We model the ubiquitous traction force pattern of a polarized cell as a single, anisotropic force dipole. The dipole magnitude is the cell force times the distance along the long axis of the cell, $P = Fa$. Since the contractile cytoskeletal machinery (e.g. actomyosin stress fibers) of the cell is typically aligned along this axis, this is also usually the principal direction of stress exerted by the cell and is henceforth called the “dipole axis”. Such a force dipole induces a strain in the substrate, which is modeled as an infinitely thick, linear, isotropic elastic medium.

By considering two dipoles $\mathbf{P}^{\alpha}$ and $\mathbf{P}^{\beta}$, we show in SI section A.1 that the work done by a dipole β in deforming the elastic medium in the presence of the strain created by the other dipole α, is given by [31]: $W^{\alpha\beta} = P^{\beta}_{il} u^{\alpha}_{il}(\mathbf{r}^{\beta})$, where the strain can be written in terms of $\mathbf{P}^{\alpha}$ and second derivatives of an elastic Green's function as $u^{\alpha}_{il}(\mathbf{r}^{\beta}) = \partial_l \partial_k G_{ij}(\mathbf{r}^{\beta} - \mathbf{r}^{\alpha}) P^{\alpha}_{jk}$. This minimal coupling between dipolar stress and medium strain represents the mechanical interaction energy between dipoles. Typical substrate strains are shown in Fig. 2.1(d) where the blue (red) coloring represents expanded (compressed) regions. A second or test dipole present in these regions would tend to align its contractile axis along the principal stretch direction of the substrate. In the expanded (blue) regions, the test dipole is aligned with and attracted towards the central dipole, whereas in the compressed (red) regions, a test dipole is aligned orthogonally to and repelled away from the central dipole. The orientational dependence of the strain field is changed by the Poisson's ratio or compressibility of the substrate [49].

Our computational "many-cell" model considers cells as discrete agents (N agents in a $L \times L$ box with periodic boundary conditions) which move and orient randomly, but that also interact with one another through long-range elastic interactions via a force dipole strain field coupling and a short-range repulsive spring. Fig. 2.1(e) shows our simulation setup and the main ingredients of the model. We ignore details of the cell shape and subcellular structures in this minimal model and instead consider the cells as disk-shaped agents endowed with contractile, elastic dipoles. This simplifying assumption implies that we do not consider changes in the shape and size of individual cells that occur as a result of cell–substrate feedback when substrate stiffness is varied, but instead focus on the multicellular structures at longer length scales.

We now consider the translational and orientational dynamics of a collection of model cells. These interact with each other through short range, steric and long-range, substrate-mediated, elastic interactions, and undergo diffusive motion. The overdamped Langevin dynamics governing the position of a cell labeled α is

$$\frac{d\mathbf{r}_{\alpha}}{dt} = -\mu_T \sum_{\beta} \frac{\partial W_{\alpha\beta}}{\partial \mathbf{r}_{\alpha}} + \sqrt{2D_{\mathrm{T}}}\ \boldsymbol{\eta}_{\alpha,\mathrm{T}}(t) \tag{2.1}$$

where D_{T} is the effective translational diffusivity quantifying the random motion of an isolated moving cell, with $\boldsymbol{\eta}_{\mathbf{T}}$ as a random white noise term whose components satisfy

$\langle \eta_{i,\mathrm{T}}(t)\eta_{j,\mathrm{T}}(t')\rangle = \delta(t-t')\delta_{ij}$. Typical adherent cells do not move very persistently and at time scales much longer than their persistence time, their motion is random and has been shown to be well-characterized by a diffusion constant [23]. We thus neglect the directed self-propulsion term typically included for active particles from the dynamics.

The mobility μ_T in Eq. 2.1 is inversely related to the effective friction from the medium that the moving cell experiences at its adhesive contacts with the substrate. Similarly, the orientational dynamics of the cell denoted by α is given by

$$\frac{d\hat{\mathbf{n}}_\alpha}{dt} = -\mu_R \sum_\beta \hat{\mathbf{n}}_\alpha \times \frac{\partial W_{\alpha\beta}}{\partial \hat{\mathbf{n}}_\alpha} + \sqrt{2D_{\mathrm{R}}}\ \boldsymbol{\eta}_{\alpha,\mathrm{R}}(t) \tag{2.2}$$

where $\hat{\boldsymbol{n}}_\alpha$ is the unit vector along the dipole axis of the cell α and D_{R} is the effective rotational diffusivity quantifying the random reorientations of an isolated moving cell. Cells encounter various forms of internal stochastic effects including internal cytoskeletal rearrangements producing membrane morphological fluctuations, substrate surface binding fluctuations and fluctuations in myosin motor forces, which are all absorbed into a coarse-grained effective temperature, T_{eff}, in our model. Single cell and cell cluster experiments have shown this effective temperature to be on the order of $10^{-15} - 10^{-14}$ J [86]. Though the rotational and translational diffusion are in principle independent, we will here assume them to correspond to the same underlying processes and therefore the same effective temperature, $k_B T_{\text{eff}} = D_T/\mu_T = D_R/\mu_R$. We also show some exceptions to this assumption in the SI section A.10, which all robustly form networks.

The pairwise cell–cell interaction potential $W_{\alpha\beta}$ between cells labeled α and β consists of the long-range elastic interaction arising through their mutual deformation of the substrate (SI section A.1), and a short-range steric interaction between two cells in contact, and is given by,

$$\begin{aligned} W_{\alpha\beta} &= \frac{1}{2}k(d-r_{\alpha\beta})^2, \quad \text{when} \quad 0 \le r_{\alpha\beta} \le d \\ &= \frac{P^2}{E}\frac{f(\nu,\theta_\alpha,\theta_\beta)}{r^3_{\alpha\beta}}, \quad \text{when} \quad r_{\alpha\beta} > d, \end{aligned} \tag{2.3}$$

where f is a function of Poisson's ratio - shown in SI section A.1, θ_α, and θ_β where $\cos\theta_\alpha = \hat{\boldsymbol{n}}_\alpha \cdot \hat{\boldsymbol{r}}_{\alpha\beta}$ and $\cos\theta_\beta = \hat{\boldsymbol{n}}_\beta \cdot \hat{\boldsymbol{r}}_{\alpha\beta}$ are the orientations of cell α and cell β with respect to their separation vector, $\mathbf{r}_{\alpha\beta} = \mathbf{r}_\beta - \mathbf{r}_\alpha$ connecting the centers of the two model cell dipoles, respectively. Note that while the elastic potential is in principle long-range, it decays strongly as a $1/r^3$ power law, we cut this pairwise interaction off at $r_{\alpha\beta} > 3d$ in our simulations, since the substrate strain induced by one cell is unlikely to be detected by a cell few cell lengths away [16].

The above equations are non-dimensionalized by a suitable choice of length, time and energy scales. By choosing the length scale to be the cell diameter d, the time scale to be an elastic time, $t_c = \frac{16Ed^5}{P^2\mu_{\mathrm{T}}}$, and a characteristic elastic interaction as the energy scale, $\mathcal{E}_c = \frac{P^2}{16Ed^3}$, the dynamical equations reduce to (SI section A.11),

$$\frac{d\mathbf{r}^*_\alpha}{dt^*} = -\sum_\beta \frac{\partial W^*_{\alpha\beta}}{\partial \mathbf{r}^*_\alpha} + \sqrt{\frac{2}{A}}\ \boldsymbol{\eta}^*_{\alpha,\mathrm{T}}(t^*), \tag{2.4}$$

for the translational motion,while the rotational equation of motion can be written as,

$$\frac{d\hat{\boldsymbol{n}}_\alpha}{dt^*} = -\sum_\beta \hat{\mathbf{n}}_\alpha \times \frac{\partial W^*_{\alpha\beta}}{\partial \hat{\mathbf{n}}_\alpha} + \sqrt{\frac{2}{A}}\ \boldsymbol{\eta}^*_{\alpha,\mathrm{R}}(t^*), \tag{2.5}$$

where the starred variables indicate nondimensionalized quantities, and we have assumed $\mu_{\mathrm{R}}d^2 = \mu_{\mathrm{T}}$ and $D_{\mathrm{R}}d^2 = D_{\mathrm{T}}$, although the latter is not required for a system that is out of equilibrium. The nondimensionalized pairwise interaction potential in Eq. 2.3 is here given by $W^*_{\alpha\beta} = \frac{1}{2}k^*(1-r^*)^2\Theta(1-r^*) - \frac{16f}{r^{*3}}\Theta(r^*-1)$, where $k^* = kd^2/\mathcal{E}_c$. We introduce an effective elastic interaction parameter quantifying the elastic interaction strength relative to that of intrinsic noise in the cell motion,

$$A = \frac{P^2\mu_T}{16Ed^3D_T} = \frac{\mathcal{E}_c}{k_BT_{\text{eff}}}, \tag{2.6}$$

where the noisy cell movements correspond to an effective temperature, $k_BT_{\text{eff}} \equiv D_T/\mu_T$. This explicitly shows that A is a measure of the characteristic elastic interaction energy scale relative to the magnitude of cell stochasticity described by an effective temperature.

2.5.2 Physiological estimates of parameter values

In experiments, the value of the effective interaction parameter A will depend on cell contractility, the stiffness of the elastic substrate, and the diffusivity that originates from the motility of single cells. Importantly, cells adapt their contractile forces to the stiffness of the underlying substrate. Measurements [87] and models [72] of the dependence of cell force on substrate stiffness suggest that the magnitude of the force dipole can be written as: $P(E) = P_0/(1 + E/E^*)$, where the characteristic substrate stiffness for a given cell at which the cell traction forces saturate to their maximal value is denoted by E^*. This dependence when inserted into the definition of the effective elastic interaction parameter, A, in Eq. 2.6, leads to A being a peaked function of E. Since stiffer substrates are harder to deform and cells on softer substrates don't generate enough traction, substrate deformations and therefore elastic interactions are maximal at an intermediate optimal stiffness value ($E = E^*$).

Table 2.1: Simulation parameters and their meaning.

Parameter	**Interpretation**	**Simulation values**
A	Elastic interaction : Noise	0.1-100
k^*	steric interaction	1.6×10^3
ϕ	Cell packing fraction	0.05-0.5
d	Cell diameter	1
L	Box size	26.66

To identify a plausible range for the values of A consistent with cell culture experiments, we note that the typical values for the force dipole for contractile cells adhered to elastic substrates is $P_0 = Fd \sim 10^{-12} - 10^{-11}$ J [53, 58]. This corresponds to measured traction forces of $F \sim 10 - 100$ nN with a distance of ~ 50 μm separating the adhesion sites at which the forces act on the substrate [51, 23], which is also the typical size of the cell along its long axis. For a typical substrate stiffness of $E \sim 1$ kPa characteristic of EC network formation [62, 61], we therefore estimate an elastic dipole energy of $\mathcal{E}_c = \frac{P^2}{16Ed^3} = \frac{F^2}{16Ed} \sim 10^{-15}$ J, similar to measured values for cell contractile energy stored in the elastic substrate [88]. Since, adherent cells crawl by exerting forces at the focal adhesions at which forces are transmitted to the substrate, the net mobility that determines cell translation, μ_T, can be estimated from the friction force at these adhesion sites. From the observation that the focal adhesions with surface area of 10 μm^2 reorient with speeds of μm/min in the direction of an external, applied stress of kPa [89], we can estimate the mobility coefficient (inverse of friction coefficient) to be

$\mu_T \sim 0.1\mu\mathrm{m}/\mathrm{min} \cdot pN^{-1}$. The effective diffusivity characterizing single endothelial cell movements was measured to be $\sim 10\ \mu\mathrm{m}^2/\mathrm{min}$ [90, 15, 61]. Together, these give an estimate for the effective temperature: $k_B T_{\mathrm{eff}} = D_T/\mu_T \sim 10^{-16}$ J $\sim 10^4\ k_B T$. For substrate stiffness $E \sim E^*$ 1 kPa, we thus estimate the ratio of elastic energy to noise to be $A = \mathcal{E}_c/k_B T_{\mathrm{eff}} \sim 10$.

In experiments, the substrate stiffness can be tuned over a wide range. In particular, Califano *et al.* tested the formation of EC networks on substrates whose rigidity was varied from $100\mathrm{Pa} - 10\mathrm{kPa}$ [62]. This, in our estimate, corresponds to an interaction parameter $A \sim 1-100$, with $A = 0.1$ corresponding to high noise or non-optimal values of substrate stiffness (too soft or too stiff). Similarly, we can estimate the characteristic timescale as $t_c = \frac{d^2}{\mathcal{E}_c \mu_{\mathrm{T}}} \sim 10^2$ min. This timescale of hours is consistent with that required for the formation of cellular structures in experiments [62].

2.5.3 Experimental Methods

Cell Culture: green florescent protein (GFP) expressing-human umbilical vein endothelial cells (HUVECs) (Angio-Proteomie) were expanded on 10mg/mL fibronectin-coated plates in Endothelial Cell Growth Medium-2 with BulletKit (EGM-2, Lonza). Cells used were between passages 3-12. Medium changes were performed every other day, and cells were split upon reaching 80% confluency.

Polyacrylamide (PAA) fabrication: PAA hydrogels were fabricated similarly to previously published protocols [73]. Briefly, hydrogels with relative stiffnesses (Young's Modulus or elastic modulus, E) at 200Pa, 480Pa, 1kPa, 2kPa, 4.5kPa, and 10kPa were fabricated by mixing acrylamide from 40% stock solution (Sigma, A4058) with bis-acrylamide from 2% stock solution (Sigma, M1533) in phosphate buffer saline (PBS). Air bubbles introduced during mixing were removed by vacuum gas-purge desiccation for 30min. The mixture was then mixed with 10% ammonium persulfate (Sigma, A3426) and tetramethylethylenediamine (Sigma, T7024) at a 1:100 and 1:1000 ratios, respectively, initiating PAA polymerization. The PAA mixture was then sandwiched between an 18mm glass coverslip (Fisher) and a hydrophobically-treated, and dichlorodimethylsilane (Sigma, 440272)-coated glass slide. After 30min of PAA polymerization, the 18mm glass slide with the PAA hydrogel attached was carefully removed from the hydrophobic slide. Lastly, PAA hydrogels were functionalized with 0.2mg/mL sufosuccinimidyl-6-(4'-azido-2'-nitrophenylamino)-hexanoate (Pierce Biotechnology) followed by 10mg/mL fibronectin.

Vascular Patterning: GFP-HUVECs were seeded on fibronectin- coated PAA hydrogels at densities of 8×10^3 cells/cm^2, 1.4×10^4 cells/cm^2, and 2×10^4 cells/cm^2 and imaged on a Nikon Eclipse TE2000-U fluorescent microscope. The images were all processed using a custom-built image processing macro in FIJI2.

2.5.4 Image Analysis

The following processing is done in order to directly compare simulation predictions to experimental results (Figs. 2.4 and 2.5) and to obtain network metrics for simulations (Fig. 2.6 and SI Figs. A.11, A.14, A.15, A.16). All image analysis used in this work was carried out using the open-source software ImageJ [91]. Raw grayscale experimental images are imported into ImageJ. ”Enhance Contrast” command is run with ”saturated pixels” widget set to 2. We then ”Despeckle” the image and ”Enhance Contrast” once more before running ”Subtract Background” with a rolling ball radius of 50 pixels. We ”Gaussian Blur” with a sigma of 10 pixels. We then threshold, keeping intensities 20 and above. This is then converted into a mask, skeletonized, and dilated four times so as to preserve the raw filling fraction (Fig. 2.4b).

For simulated networks like those shown in Fig. 2, we replace the isotropic disk markers with “pill-box” shaped markers (as seen in SI Fig. A.11) which are elongated along the dipole axis of each cell to guide the subsequent skeletonization. Using ImageJ, we first apply ”Gaussian Blur” with a sigma of 2 pixels; then, we threshold keeping intensities 150 and above; and then, convert into a mask and skeletonize. Finally, we dilate the skeleton four times so that small scale features of assembly like compact rings are preserved, while washing out the shape of the individual disks. At this point, both experimental and simulated images are dilated skeletons. The packing fraction of the dilated skeleton representations of simulations ($\tilde{\phi}$) are smaller than their respective non-overlapping disk packing fraction (ϕ) by a factor, $\tilde{\phi} \approx 0.75\phi$. To compute fractal dimensions, we follow the aforementioned image processing with the additional step of dilating experimental skeletons so as to have roughly the same packing fraction as simulations. We then use ImageJ's ”Fractal box count” tool with the default pixel array.

To identify unique clusters in both experimental and simulation images, dilated skeleton images are imported into a custom python program. This program assigns a cluster label to the first nonzero pixel, then does recurrent loops assigning neighboring pixels to the same cluster label until a pixel is identified that does not neighbor any of the pixels with this cluster label. The cluster label is incremented, and the process repeats until every nonzero pixel is assigned a cluster label.

Chapter 3

Collective cell polarization drives large scale compaction of gels

3.1 Introduction

The capacity for a group of cells to coordinate both their relative positions to one another and the forces they exert on their environment is critical for biological phenomena such as wound healing [92], embryonic development [93], and cancer metastasis [94]. A recent *in vitro* experiment of adherent cells embedded in collagen gel networks mimicking fibrous ECM shows that cell collectives are capable of compacting the surrounding matrix to as little as less than 1% its pre strained volume [95]. Furthermore, it has been verified across several of these experiments that this compaction follows a phase transition like behavior in cell seeding density (Fig. 3.1c) [85, 96].

In the most recent of these experiments, it was seen that at low cell seeding density, cells remain largely sedentary and isolated from one another, and the gel retained its original shape. At and above a critical seeding density, gel contraction was preceded by cells forming local connections with one another until a fully connected network structure had been assembled (like those seen in simulations of cells modeled as anisotropic contractile force dipoles on elastic substrates [32]). Furthermore, the authors of these studies consistently state that it is the restructuring of the gel fibers, themselves, that is necessary for the observed transition. Here, we ask if the capacity for cells to polarize one another by mutual substrate deformations thereby enhancing the net contractility they apply to the gel is a sufficient mechanism to produce a transition in the likeness of experimental observation given a fully connected static matrix network architecture.

We think of this cell coordinated large scale force production in close analogy with the polarization of electric dipoles. In the case of electric dipoles, the product of the electric field and the electric polarizability gives a polarization density. In the analogous case of elastic dipoles, the product of the strain field and a mechanical polarizability (which we will call the feedback parameter later) gives us a contractility density. It is in the case of electric dipoles that at high density the dielectric constant of the material diverges at a critical combination of dipole density and polarizability as seen from the Clausius-Mossotti equation [97, 98]. We speculate that the shape of the curve in fig. 3.1c could reflect an experimental realization of the mechanical analogue of the Clausius-Mossotti relation wherein contractile force dipoles polarize one another by their strain field in a runaway fashion resulting in large scale contraction of the surrounding gel.

3.2 Model and Results

We utilize a Brownian Dynamics framework in two dimensions where the ECM is represented by a fully connected triangular lattice of of nodes connected to one another by Hookean springs with stretching and bending stiffness k_m and rest length $l_{0,m}$. Cells are modeled as "active bonds" of stiffness k_c which possess a rest length $l_{0,c}$ smaller than those of the matrix. This picture of a cell can be implemented as a single bond per cell, a cell which has a center of contraction, six neighboring nodes, and therefore six active bonds whose internal strain can be isotropic by averaging over all six bonds or anisotropic by averaging over colinear pairs. We will call the first representation A1, the second I6, and the third A6. Lastly, we consider a feedback parameter, α, for the model cells that up-regulates force production proportionally to cell strain as a coarse grained mechanism for stress induced myosin recruitment (Fig. 3.2). This model is an extrapolation of a one-dimensional model of cell polarization on elastic substrates [54].

Rather than considering the deformation of a free boundary as is done in the motivating experiments, we will consider a fixed boundary and use the boundary stress as

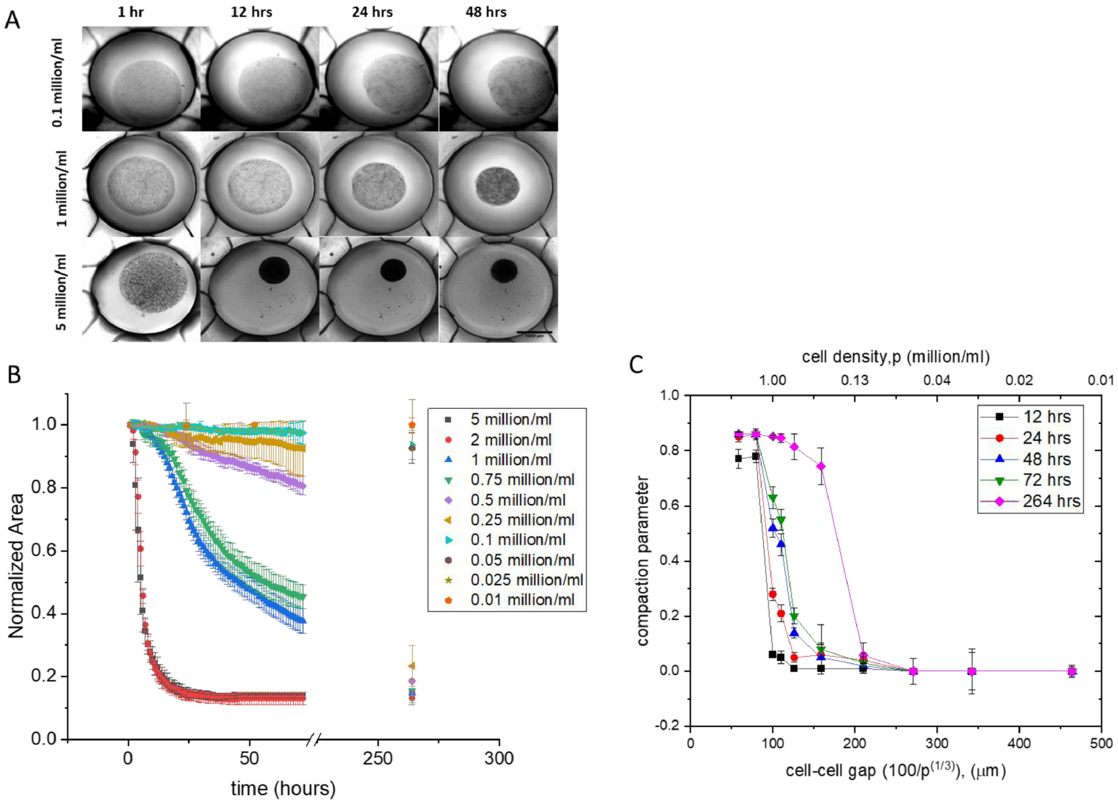

Figure 3.1: Fibroblasts embedded in collagen gels induce global compaction. (A) Bright field images at 1hr, 12hrs, 24hrs, and 48hrs of seeding densities 0.1 million/ml, 1 million/ml, and 5 million/ml. Scale bars = 1mm. Gels seeded with a higher density of fibroblasts contract to a greater extent within the same time interval. (B) Area as a function of time for various seeding densities. Highest seeding densities saturate to a final area of about 15% the initial area. (C) Compaction parameter ($\equiv 1 - \frac{A}{A_0}$ where A is the area of the gel at time t and A_0 is the initial area of the gel disk) as a function of cell density (top x-axis) or, equivalently, cell–cell gap (bottom x-axis). Area contraction undergoes a phase transition in cell density whose critical density can be shifted by time. Reprinted from Acta Biomaterialia, 154, Umnia Doha, Onur Aydin, Md Saddam Hossain Joy, Bashar Emon, William Drennan, M. Taher A. Saif, Disorder to order transition in cell-ECM systems mediated by cell–cell collective interactions, 290-301, Copyright (2022), with permission from Elsevier (Ref.[85]).

a proxy measure of contraction. For simplicity, we begin by considering the aforementioned system in athermal conditions. Thus, we can write the equation for the force on

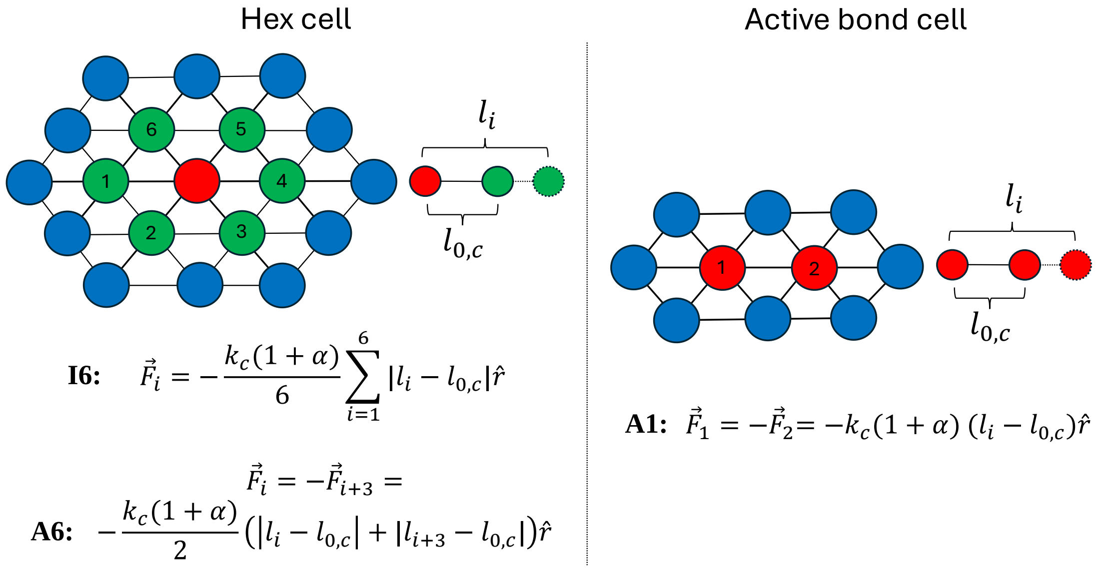

Figure 3.2: Dipole in spring network matrix (blue) schematic. (Left) A model cell can be seen as a central active node (red) surrounded by six nodes representing the cell boundary (green). When this cell contracts, it can sense either an isotropized average internal strain (I6) or an anisotropic average of strains in colinear bonds (A6) by which to regulate its active force. (Right) Another model of the cell can be an active bond (red–red), wherein the cell has only one internal strain with which it modulates its active force production.

node i, in the A1 representation, by the following:

$$\mathbf{F}_{ij}(r_{ij}) = \begin{cases} -k_c(1+\alpha)(\mathbf{r}_j - \mathbf{r}_i - l_{0,c}\hat{\mathbf{l}}_{ij}) & l_{ij} \text{ is active} \\ -k_m(\mathbf{r}_j - \mathbf{r}_i - l_{0,m}\hat{\mathbf{l}}_{ij}) & l_{ij} \text{ is not active} \end{cases}$$

where each node will sum over each of its six neighbors and the discretized equation of motion for each node i can then be written

$$\mathbf{r}_i(t+\Delta t) = \mathbf{r}_i(t) + \Sigma_{j=1}^{N=6}\mathbf{F}_{ij}(r_{ij})\Delta t. \tag{3.1}$$

Whether randomly or specifically placed, active bonds are constrained to be within an inner region, called R_{in}, of the simulated mesh such that $R_{in} = 0.5R_{out}$ where R_{out} is the radius of the fixed boundary. Simulations are run, regardless of their initial conditions, with a time step $\Delta t = 0.01$ until mechanical equilibrium is reached ($F_{total} \leq 10^{-6}$).

Preliminary simulations of the described system of A6 cells placed such that, for a given spacing, or separation distance, they are maximally packed yields a qualitative trend of more highly strained networks with increasing density and feedback parameter α (Fig. 3.3).

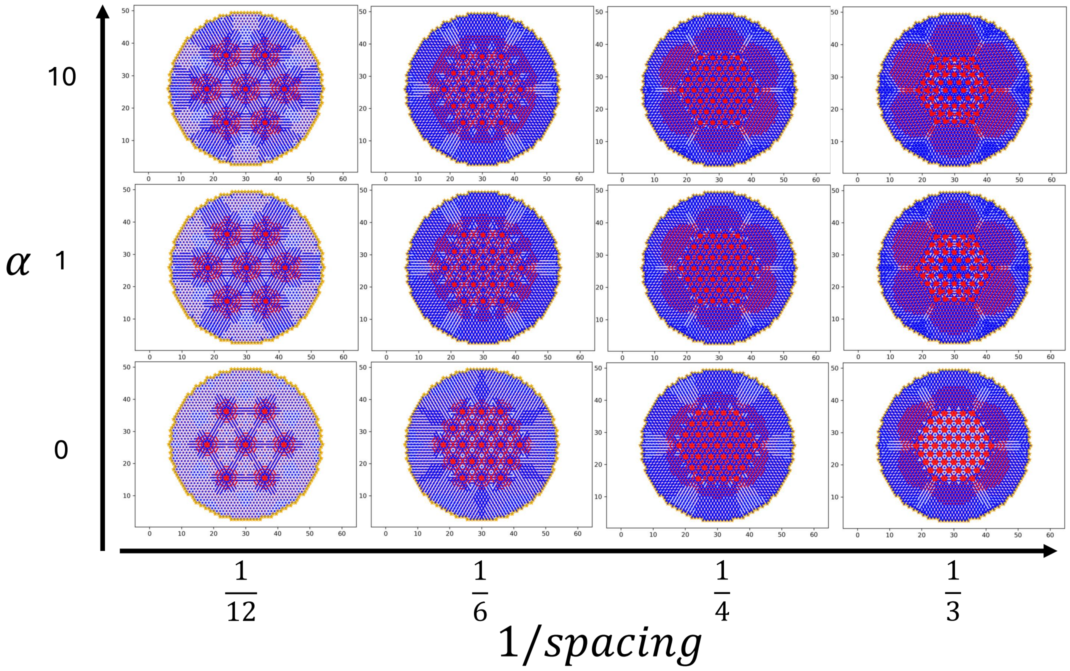

Figure 3.3: Final simulation snapshots of A6 cells in the space of density (1/spacing - x-axis) and feedback parameter α (y-axis). Fixed boundary nodes represented by orange stars. Bonds under slight tension (compression) represented by thin blue (red) lines. Bonds under large tension (compression) represented by thick blue (red) lines. At small spacing and $\alpha = 0$, tensile strain paths do not reach the boundary. By increasing α, strain sensitive forces allow tensile strain paths to broaden and reach the boundary. Similarly, increasing density produces further strain propagation.

To begin to quantitatively compare simulated networks and experiments, we randomly select bonds in the inner region and make them active with the additional constraint that no two centers of contraction can be within 3 lattice spacings of one another until the desired density is reached. This is done to accentuate the substrate mediated interactions as opposed to direct cell–cell communication. By specifying the number of dipoles, we can calculate the average intercellular spacing from the relation $\frac{\pi R_{in}^2}{N} = \pi a^2$ where N is the number of dipoles, R_{in} is the inner seeding radius, and a is the radius defining an area of exclusion.

In fig. 3.4a, we plot the boundary stress - the total force on the fixed boundary nodes divided by the circumference of the boundary - as a function of $\frac{1}{a^2}$ which is proportional to N. While we see a linear relation for $\alpha = 0$, whether the non-zero α cases exhibit linearity is unclear. If we instead plot boundary stress divided by N, we see that in the regime of small average spacing, *i.e.*, high density, there is indeed non-linearity which increases with the feedback parameter α (Fig. 3.4b). While this resultant trend of the model is in line with the experimental results that motivate it, the magnitude of the non-linearity is clearly distinct from the fibroblasts in collagen gels.

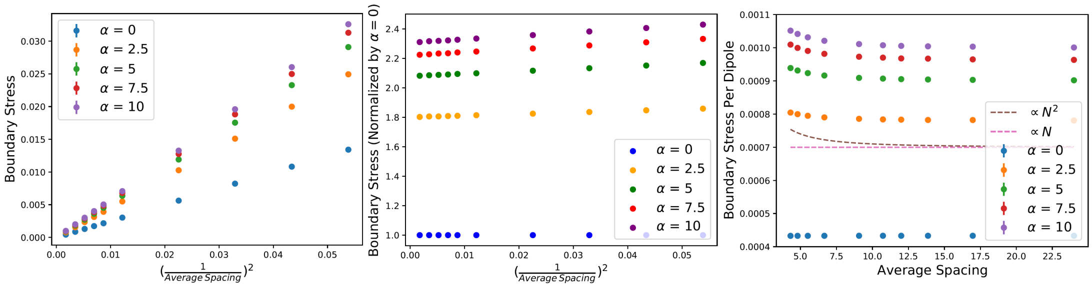

(a)

(b)

(c)

Figure 3.4: Simulated A6 cells with strain sensitive active force show non-linear boundary stresses. (a) Boundary stress versus the inverse of the average dipole spacing squared shows that while strain insensitive dipoles ($\alpha = 0$) are indeed linear, it is unclear if this holds for $\alpha \neq 0$. (b) Boundary stress normalized by α = 0. (c) Boundary stress per dipole reveals that at low average spacing, or high cell density, boundary stress is indeed non-linear for strain sensitive dipoles, reaching N^2 proportionality at α = 10, indicating a cooperative effect.

An obvious and pertinent deviation of these simulations from the collagen gel experiments is the motility of the cells themselves. While one could add dynamics to the location and/or orientation of the active bonds themselves, another way to account for this motility in a more discrete way is to simply consider the elastic energy of a given configuration as cells will move in such a way as to minimize this energy. Modeled cells exert a contractile force on surrounding nodes, giving rise to a mixture of stretched and compressed matrix springs. By placing another modeled cell in a stretched region, the stretch in these proximate matrix springs can be alleviated by the two dipoles cancelling their forces, thus lowering the elastic energy in the matrix. The opposite is true for the compliment, that is, placing a model cell in a compressed region accentuates the compression and the elastic energy is increased. Fig. 3.5(a) shows that randomly placed A1 model cells with both random and specified dipole orientations exhibit primarily unfavorable interactions as indicated by higher elastic energy at smaller seeding radius. Conversely, Fig. 3.5(a) shows that three A1 model cells with x-oriented dipole orientations decrease elastic energy at smaller spaces. These results indicate that both positional and orientational order are required for energetically favorable states.

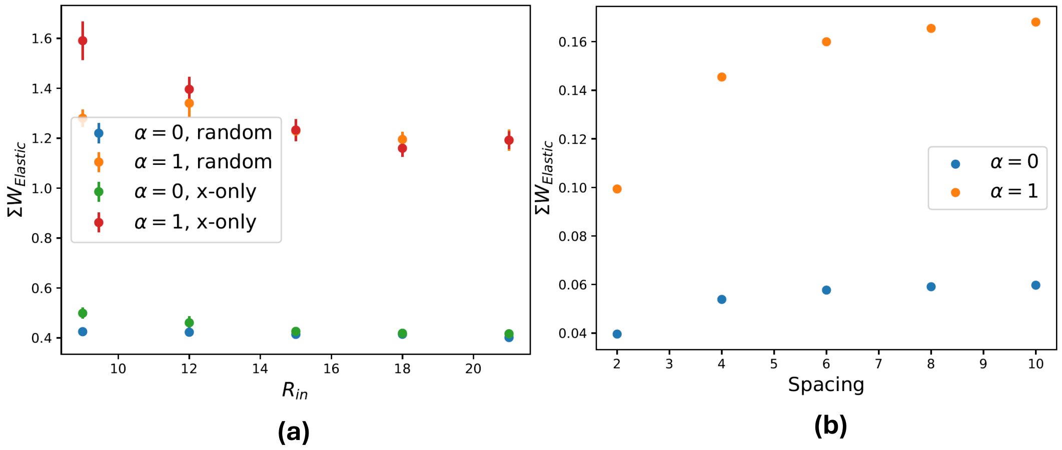

Figure 3.5: Both positional and orientational order are required for energetically favorable dipolar interactions. (a) Total elastic energy of matrix springs at mechanical equilibrium as a function of seeding radius (analogous to spacing) for $N = 20$ A1 active bonds. Average values of ten simulations are plotted where the error bars are the standard error of the mean. While for all active bonds - whether they are sensitive to strain (orange and red) or not (blue and green) - positions are random, their orientations are made to either be random (blue and orange) or fixed along the x-axis (green and red). For both strain sensitive and insensitive dipoles, whether randomly or specifically oriented, elastic energy does not decrease with decreasing seeding radius, indicating predominantly unfavorable interactions. (b) Total elastic energy of matrix springs at mechanical equilibrium for $N = 3$ A1 dipoles oriented along the x-axis placed on a line where intercellular spacing is varied. As expected for energetically favorable interactions, elastic energy is decreased as dipole spacing decreases for both strain sensitive (orange) and strain insensitive (blue) dipoles where the magnitude of the minimum is accentuated for $\alpha = 1$.

3.3 Summary and Future Work

Motivated by experimental work of fibroblasts embedded in collagen gels, we built a model of a discretized elastic material realized by a triangular mesh of Hookean springs with active bonds which produce mechanosensitive dipolar forces on the matrix. Our preliminary results show that by increasing simulated cell density and strain sensitive force production, tensile strain bands can broaden and propagate to the boundary. Furthermore, our simulations confirm a non-linearity in boundary stress as a function of number of dipoles even for our linear elastic material. While the shape of this non-linearity is too subtle to be compared to the phase transition seen in experiments, we have shown that the energetic favorability of cell configurations depends not only on their effective density, but their spatial and orientational patterning. We thus hypothesize that by weighting boundary stress by a Boltzmann factor in elastic energy that would privilege highly ordered configurations, as those seen in the supercritical density regime of collagen gel experiments, we may be able to recover a sharp transition resembling the global compaction of collagen gels. Additional sources of nonlinearity that may be explored include a larger stretching modulus than compression modulus of the matrix springs. We could also include a distance dependent step function to model direct cell–cell contact mediated force production and transmission. Additionally, we may make the feedback parameter, α, itself into a functional form like a sigmoid in strain. This is motivated by observed limits to cell–cell sensing. While the model(s) we have discussed above assumes cell sensitivity to internal strain, it may be appropriate to instead assert sensitivity to external strain. We could also phenomenologically impute that cells in ordered multicellular configurations increase their dipole moment. If these permutations are insufficient to produce the desired phase transition like behavior, network architecture itself may be necessary to explore, *i.e.*, coordination number less than six. In these networks, model cells can serve to stretch out floppy modes in the matrix thereby strengthening boundary force transmission [99], or even dynamic spring constants in analogy to buckling/breaking and tether formation [100].

Chapter 4

Collective states of active particles with elastic dipolar interactions

This chapter has been reprinted with permission according to the creative commons attribution license (CC BY) [65]. Note that portions of figures 4.1, 4.2 and the entirety of figures 4.4, 4.7, and 4.8 and their corresponding descriptive text was the work of Subhaya Bose. Portions of the introduction have been moved to the introduction of the dissertation. References to supplementary information have been omitted.

4.1 Abstract

Many types of animal cells exert active, contractile forces and mechanically deform their elastic substrate, to accomplish biological functions such as migration. These substrate deformations provide a mechanism in principle by which cells may sense other cells, leading to long-range mechanical inter–cell interactions and possible self-organization. Here, inspired by cell mechanobiology, we propose an active matter model comprising self-propelling particles that interact at a distance through their mutual deformations of an elastic substrate. By combining a minimal model for the motility of individual particles with a linear elastic model that accounts for substrate-mediated, inter–particle interactions, we examine emergent collective states that result from the interplay of motility and long-range elastic dipolar interactions. In particular, we show that particles self-assemble into flexible, motile chains which can cluster to form diverse

larger-scale compact structures with polar order. By computing key structural and dynamical metrics, we distinguish between the collective states at weak and strong elastic interaction strength, as well as at low and high motility. We also show how these states are affected by confinement within a channel geometry – an important characteristic of the complex mechanical micro-environment inhabited by cells. Our model predictions may be generally applicable to active matter with dipolar interactions ranging from biological cells to synthetic colloids endowed with electric or magnetic dipole moments.

4.2 Introduction

Active matter typically comprises autonomous agents, biological or synthetic in origin, that harness internal energy sources to move [101, 102]. These agents often undergo complex interactions with each other and their surrounding media that influence their collective behavior [103]. Mechanical interactions through a material medium are by their nature long-range and are expected to govern the collective states of active particles[104], and enrich the large–scale phenomena such as phase separation that arise purely from motility [10, 105].

In general, active particles endowed with a dipole moment are expected to interact at long range with each other while also propelling themselves. Passive dipolar particles such as ferromagnetic colloids at equilibrium will align end-to-end into linear structures such as chains or rings [41, 106]. At higher densities, the chains intersect to form gel-like network structures [42]. Topological defects in the networks such as junctions and rings are expected to affect the phases of passive dipolar fluids [107, 108]. When powered by chemical activity, dipolar colloidal systems exhibit self-assembly that depends on both the long-range, anisotropic interactions, as well as active motion, as revealed in recent experiments [45]. Such structures have also been studied in simulation in the context of active dipolar particles representing auto-phoretic colloids [109, 44], as well as swimming microorganisms [46] such as magnetotactic bacteria [47]. In related theoretical studies, constrained or bundled chains of self-propelling colloidal particles [110, 111, 112, 113] have also been shown to exhibit collective instabilities. Elasticity mediated interactions are seen to play critical roles, with the competition between mechanical interactions, steric interactions and activity determining the eventual dynamical behavior.

Here we build a minimal model of interacting elastic dipoles that is inspired by the mechanobiology of animal cells that actively deform their elastic substrate, while also exhibiting persistent motility. The starting point is the observation and deduction that contractile deformations of the underlying substrate originate from the elastic dipolar nature of stresses exerted by the cell on the substrate [114]. We show that incorporation of these substrate-mediated interactions offers a robust way to the formation of compact, and relatively stable collective states. Our model combining active self-propulsion of the particles with their long-range dipolar interactions applies to a general class of experimentally realizable systems, including synthetic colloids endowed with permanent or induced magnetic or electric dipole moments [115]. By performing Brownian dynamics simulations on a collection of such dipolar active particles, we demonstrate the rich array of collective states that they can self-organize into. In particular, strong dipolar interactions promote end-to-end alignment of active particles, leading to self-assembled, motile chains. These chains can then further self-assemble into a hierarchy of larger-scale structures.

4.3 Model

Our model system consists of soft, repulsive, active Brownian particles (ABPs) [7, 116] in two dimensions (2D), that interact at long range through elastic dipolar interactions and strongly repel when they overlap. We have previously studied a simple isotropic interaction model valid in the limit where the propulsion direction was decoupled from the magnitude of cell-cell interactions [64]. Here, we analyze a more general model that accounts for the anisotropy of cell interactions, expected for the elongated shapes characteristic of migrating cells.

The basis of elastic interactions between model cells is illustrated in Fig. 4.1. The schematic Fig. 4.1a shows the typical scenario of an adherent cell on top of an elastic substrate. The internal cytoskeletal machinery of the cell comprising actin stress fibers and myosin II molecular motors generates contractile mechanical forces, that are com-

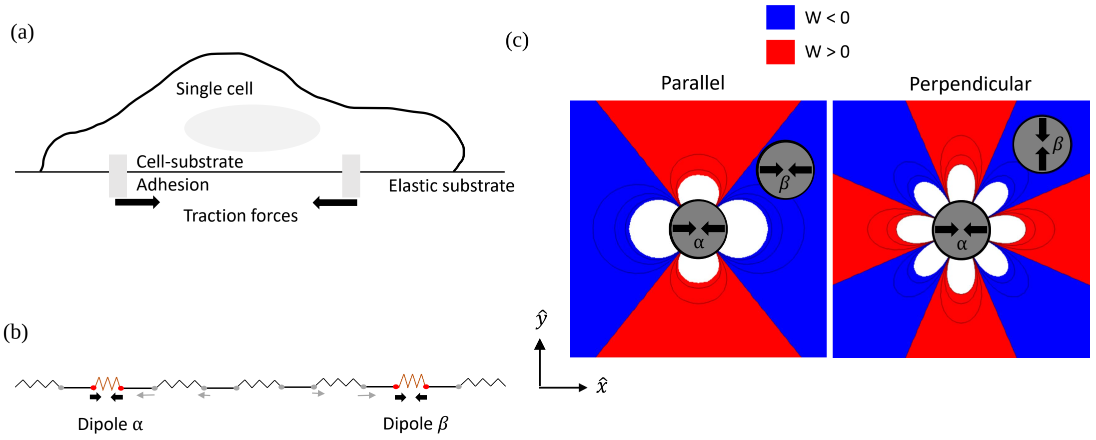

Figure 4.1: Elastic interactions between model cells on a substrate. (a) Schematic of adherent cell on an elastic substrate. (b) 1D spring model illustrating origin of elastic interaction potential between two contractile dipoles. The elastic energy stored in the medium corresponding to the deformation of springs depends on the relative placement of the dipoles. In particular, placing a contractile dipole in a region where the medium is already expanded by the other dipole can help to reduce the overall deformation of the medium. This leads to a strain-dependent interaction potential between the two dipoles. (c) Representative spatial maps of the interaction potential $W^{\alpha\beta}$ between two dipoles, from the solution of the strain field for the full linear elastic problem of forces exerted on the surface of a semi-infinite medium are shown. The interaction potential corresponds to the work done by a point-like dipole in deforming the substrate in the presence of the strain created by the other. The potential maps shown here are for a pair of contractile force dipoles of fixed orientation. The second dipole is free to translate but held parallel (left) or perpendicular (right) to the central dipole which is placed at the origin and aligned along the x-axis. The contour lines show how the potential decays in space, whereas blue and red regions correspond to attractive ($W^{\alpha\beta} < 0$) and repulsive ($W^{\alpha\beta} > 0$) interactions, respectively.

municated to the external substrate through cell-substrate focal adhesions [117]. In a minimal, coarse-grained description, the traction force distribution of an elongated cell with a long axis $\mathbf{a}$ and exerting a typical force $\mathbf{F}$ at the adhesion sites, can be modeled as a force dipole with dipole moment $P_{ij} = F_i a_j$. The theory of continuous elastic media then determines that the distribution of forces from multiple cells will lead to a restoring stress σ in the medium, that satisfies a force balance [29], $\partial_j \sigma_{ij} = -\partial_j p_{ij}$, where the net dipole density, $p_{ij}(\mathbf{x}) = \Sigma_\alpha P_{ij}^\alpha \delta(\mathbf{x} - \mathbf{x}^\alpha)$ is the sum of traction forces exerted by each point-like cell dipole, here labeled by an index α. In modeling cells as point-like dipoles, we ignore their finite size, an assumption that is valid only at "far field", *i.e.* at distances large compared to cell length. While this is not strictly the case in our simulations, a more general model accounting for finite separation of the cell forces is expected to lead to qualitatively similar interactions [22].

By considering two dipoles $\mathbf{P}^\alpha$ and $\mathbf{P}^\beta$, we can show that the work done by a dipole β in deforming the elastic medium in the presence of the strain created by the other dipole α, is given by [31]: $W^{\alpha\beta} = P_{ij}^\beta u_{ij}^\alpha(\mathbf{x}^\beta)$. This minimal coupling between dipolar stress and medium strain represents the mechanical interaction energy between dipoles. The strain in the elastic medium created by dipole α at the position of the dipole β is given by the gradient of the displacement, $u_{ij}(x) = \frac{1}{2}(\frac{\partial u_i}{\partial x_j} + \frac{\partial u_j}{\partial x_i})$ and can be calculated using standard methods in linear elastic theory [29]. This is detailed in the Methods section, where we follow the treatment introduced in Ref. [31]. The mechanical interaction between a pair of force dipoles is illustrated by the schematic in Fig. 4.1b in the form of a 1D series of springs representing the effect of the elastic substrate. While the springs underlying the contractile dipoles are compressed, the springs between them are stretched. By moving to different positions in the medium for a given position of dipole α, the dipole β can reduce the net substrate deformation energy by compressing regions stretched by dipole α. This leads to a substrate deformation-mediated elastic force on the dipole β,

$$f_{el}^\beta = -\frac{\partial W^{\alpha\beta}}{\partial \mathbf{x}^\beta} = -P_{ij}^\beta \frac{\partial u_{ij}^\alpha(\mathbf{x}_\beta)}{\partial \mathbf{x}_j^\beta}, \tag{4.1}$$

given by the gradient of the strain induced by the other dipole, where the strain therefore acts as a potential. While the expressions vary in detail, this physical interaction between elastic dipoles considered here is analogous to the interaction of an electric dipole with the electric field induced by another dipole. A similar reciprocal force results on dipole α, since the interactions are based on an elastic free energy. The physical origin of this force is the tendency of the passive elastic medium to minimize its deformations in response to the active, contractile forces generated by the cells. This generic mechanical interaction between dipoles is not limited to cells [31], but also occurs for passive inclusions in an elastic medium [118]. Experimentally, hydrogen atoms in metals were shown to diffuse and distribute themselves according to configurations dictated by these elastic interactions [119].

Pairwise dipolar interactions are anisotropic and depend on both the distance between and relative orientations of the two particles with respect to their separation axis. Insights into the nature of the elastic interaction potential between a pair of force dipoles may be obtained from Fig. 4.1c where we plot spatial maps of the interaction potential $W^{\alpha\beta}$ for two cells with fixed orientation. To plot these functions, we choose a reference contractile force dipole α that is fixed at the origin with its axis along the $-x$ direction, *i.e.* whose dipole moment has purely the P_{xx} component. A second test dipole β interacts with the reference dipole according to its position and orientation. The red (blue) regions in the potential maps in Fig. 4.1c represent repulsion (attraction) which arises from the substrate strain. Here, we use the convention that stretched (compressed) regions have positive (negative) strain, while compressive dipole moment is negative. While the map on the left corresponds to parallel alignment, that on the right maps the interaction potential for perpendicular alignment of the two dipoles. In this example, we fix the orientation of the second dipole to be either parallel or perpendicular, and therefore it couples to either the u_{xx} or the u_{yy} component of the strain according to Eq. 4.1. In general, the dipoles can also rotate and change its relative orientations. In particular, while the favorable parallel configuration shown here leads to end-to-end alignment of the dipoles, the unfavorable perpendicular configuration will lead to mutual torques that tend to orient them in the favorable parallel configuration. The elastic material comprising the substrate is treated as homogeneous and isotropic with shear and compression modulii proportional to the Young's modulus E, and a Poisson ratio ν that provides a measure of its compressibility [49]. While the Poisson's ratio can in principle have the full range $-1 < \nu < 1/2$ in linear elasticity theory, the figures plotted here correspond to $\nu = 0.1$[1].

The interaction potential and model dynamics are detailed in the Methods Section 4.5 in Eq. 4.4-Eq. 4.7. As shown in Fig. 4.2a, the ABPs – here termed particles – are modeled as circular disks of diameter σ, each particle being endowed with a dipole moment and a self-propulsion direction $\hat{\mathbf{n}}$. The orientation of $\hat{\mathbf{n}}$ is aligned with the dipole axis (shown as the bold black line). This assumption is reasonable for motile cells with elongated shape, but is not necessarily satisfied for all cell types, where higher force multipoles may be relevant [24]. Particles are assumed to self-propel with a speed v_0. This phenomenologically models the movement of cells which require internal cell forces arising from actomyosin activity as well as the remodeling dynamics of the cell-substrate adhesions, not explicitly modeled here. Additionally, the motion of each particle is subject to forces and torques arising from dipolar interactions with other particles, as well as a random stochastic force. This latter mimics the effect of the thermal environment surrounding the particles and leads to diffusive effects in both orientation and spatial position of the ABPs.

Since we are motivated by adherent cells on elastic substrates whose contractile traction forces act as elastic dipoles, a cutoff distance of $r_{\text{cut}} = 7\sigma$ (red dashed circle in Fig. 4.2a) is imposed on the long range dipolar interactions. The choice of a cutoff length for interactions is consistent with experimental observations that cells can interact with one another via mechanical signaling at distances that are up to a few cell lengths away [15, 16]. In addition to the long-range interactions mediated by the elastic substrate, cells may also interact via short-range interactions. Here we introduce short-range steric repulsion using a mechanical model using compressive springs that discourage overlap between neighboring particles. Specifically, two particles in close-contact exert a repulsive elastic force on each other when the center-to-center distance is less than the rest length σ of these springs.

The ensuing dipolar interactions, when strong enough relative to the stochastic noise, cause end-to-end chaining of the particles along their dipole axis. Examples of this

---

[1] This choice ensures end-to-end alignment of dipoles and provides interactions seen not just in cells but also in other types of active matter that feature particles with magnetic or electric dipole moments. The interactions at $\nu > 0.3$ have a different symmetry and can result in more complex structures such as short rings without any electric or magnetic analogs [58].

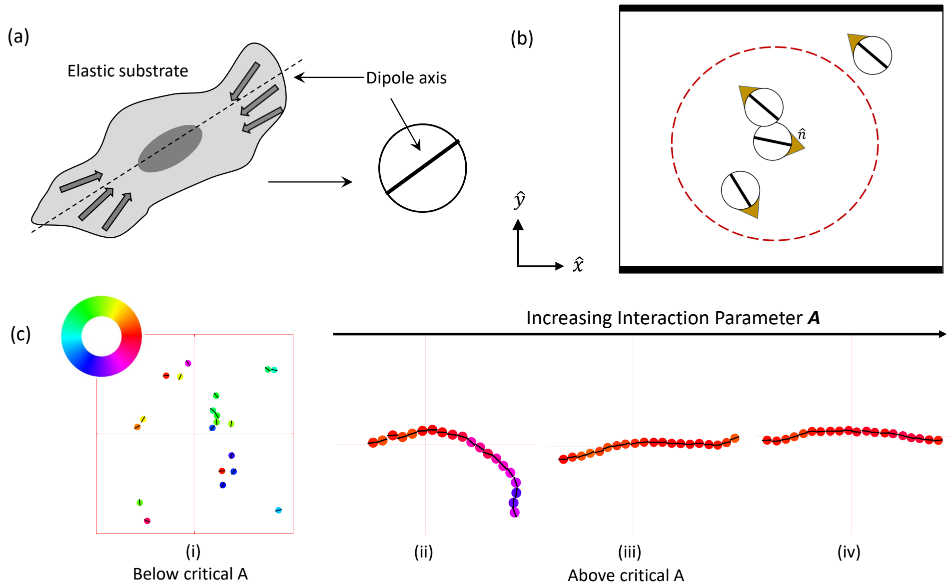

Figure 4.2: Overview of agent based simulations of active Brownian particles (ABPs) moving in the x-y plane and interacting mechanically via elastic deformations induced by contractile, active force dipoles. (a) An elongated cell with traction forces distributed around its long axis is modeled as a disk-like particle endowed with a dipole moment. (b) Each ABP has a dipole axis represented by the bold black line and an in-plane self-propulsion direction represented by the gold arrow. These particles move on a linearly elastic, thick, flat substrate, on which they exert contractile dipolar stresses. Substrate deformation due to one particle is sensed by neighboring particles. These dipole-dipole elastic interactions are confined to particles within a cutoff distance $r_{\text{cut}} = 7\sigma$ (shown as the dashed red circle). Particle overlap is penalized by a short-range steric repulsion. They are confined by steric repulsions along the top and bottom walls shown by the thick lines, while being free to move through periodic boundaries shown by the thin lines. (c) For figure (i), simulation snapshot shows that weakly interacting particles do not stick to each other and move as independent entities. As the elastic dipolar interaction parameter A increases, the particles self-assemble into long chains ((ii)-(iv), zoomed view shown). The flexibility of the chains and fluctuations in the mean curvature both decrease with increasing values of the interaction parameter. The colors represent the self-propulsion direction of each particle, as indicated by the color wheel.

chaining process are seen to occur in our simulations and representative snapshots are shown in figure 4.2c. As expected intuitively, increasing interaction gives rise to stronger alignment resulting in chains that are progressively less flexible. The effective elastic bending modulus of these chains that determines the fluctuations of the backbone contour of the chained ABPs is thus higher with increasing interaction strength.

To illustrate the bulk behavior of interacting ABPs as well as the effect of confinement on emergent collective patterns, we simulate a few hundred of these particles in a box confined in the $y-$ direction, and periodic in the $x-$ direction. The confining boundary is lined by repulsive springs of the same type used to penalize particle overlap and keeps the ABPs from escaping the simulation box. This setup mimics a channel geometry typically used in cell motility experiments [120] and is used in other works on simulations of ABPs under confinement [121, 122, 123]. We focus on the physical barriers to cell motility and not interfaces in the elastic medium. In principle, such elastic interfaces can lead to additional elastic torques and forces on dipoles by inducing "image forces" [31], but this is outside the scope of the present work. One way to realize this type of confining boundary that does not induce stresses in the elastic medium is to culture cells on a large and thick slab of hydrogel with uniform elastic properties, but micropattern a specific region of the substrate with ligands to which the cells can adhere – a common technique in mechanobiological cell culture studies [13].

The important nondimensional control parameters in the model are the elastic dipole-dipole interaction strength A, the active self-propulsion velocity characterized by a Péclet number,. Pe, and the packing fraction, ϕ. The packing fraction used in simulations below is typically either $\phi = 0.08$ or 0.25 corresponding to relatively dilute regimes, except in a narrow channel geometry where we go up to $\phi = 0.75$. Definitions and physical interpretations of these parameters are provided in the Methods Section 4.5.

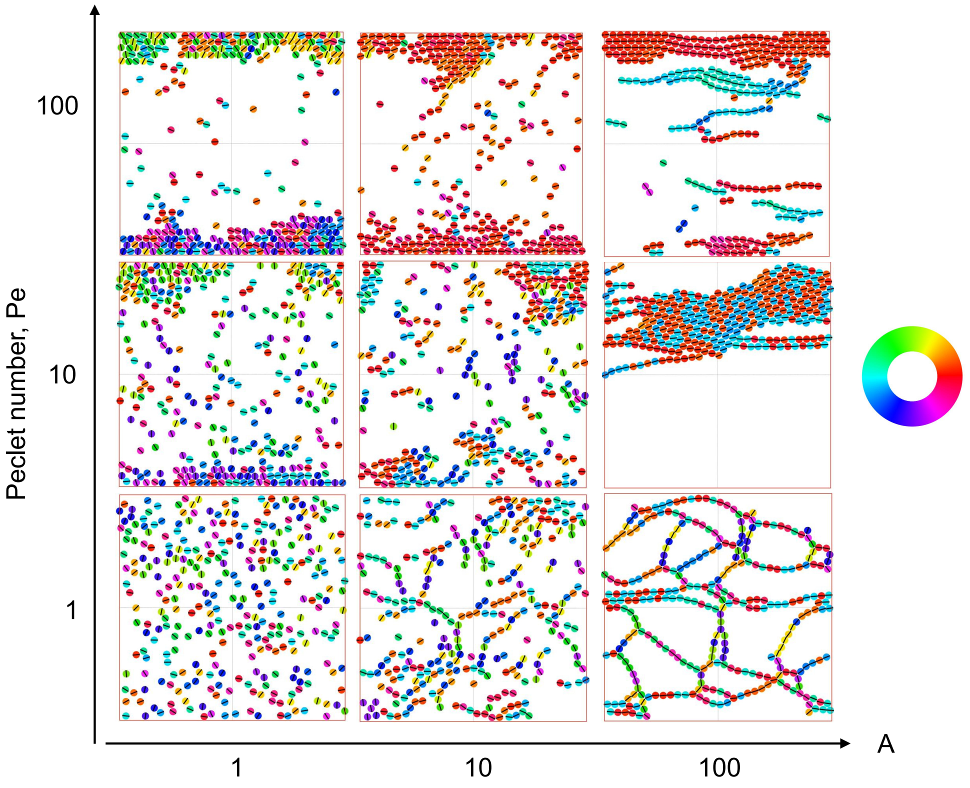

Figure 4.3: Simulation snapshots of active particles with short range steric repulsions and long-range elastic dipole-dipole interactions as a function of effective elastic interaction $A = P^2/E\sigma^3 k_\mathrm{B} T_\mathrm{eff}$ and Péclet number $Pe = \sigma v_0/D_\mathrm{T}$. Particles are confined in the y-direction, while they experience periodic boundary conditions in the x-direction. They are colored according to their self-propulsion direction $\hat{\mathbf{n}}$, and coded based on the color wheel. Motile particles at low effective elastic interaction collect into clusters at the boundaries. Strong elastic interactions promote network formation at low activity. Strong elastic interactions paired with high activity gives rise to active polymers and polar bands.

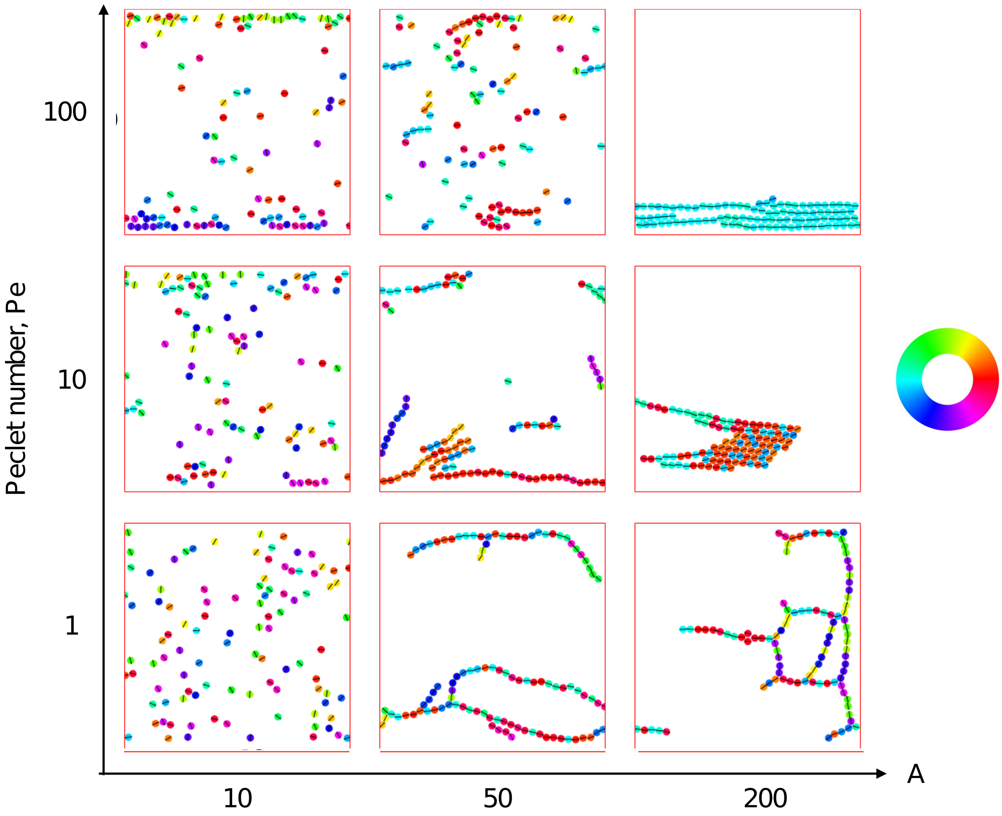

Figure 4.4: Simulation snapshots of active particles at low packing fraction - The interaction parameter $A \equiv P^2/E\sigma^3 k_\mathrm{B}T_\mathrm{eff}$ and Péclet number $Pe \equiv \sigma v_0/D_\mathrm{T}$ define the collective behavior of the particles. Particles are confined in the y-direction, while they experience periodic boundary conditions in the x-direction. They are colored based on the direction of $\hat{\mathbf{n}}$, as indicated by the color wheel. At low interaction parameter $A = 10$, the particles remain isolated and diffuse. At high Pe, more particles get collected at the confining boundary. At higher values of the interaction parameter, A, particles form chains. The typical length of the chains is seen to decrease with increasing Pe. At very high interaction parameter, $A = 200$, networks with multiple branches form at low Pe, while chains aggregate into polar clusters at $Pe = 10$. Although the particles in the cluster are oriented in opposite directions, the cluster is stable and moves in the direction given by its overall polarity. Again at very high Péclet, $Pe = 100$, the particles in the chains are oriented in the same direction.

4.4 Results

4.4.1 Characteristic states of active dipolar particles: chains, polar bands, clusters and networks

We first explore the possible collective structures that result from the combination of active self-propulsion with dipolar attraction and alignment. We explore the parameter space of activity (given by the Péclet number, Pe) and strength of dipolar interactions (given by the effective elastic interaction parameter, A) for two representative systems: one dilute and the other semi-dilute. We show representative snapshots of the steady states of the simulations by coloring the particles according to their orientation. Collections of these snapshots as well as the color wheel corresponding to particle orientations are shown in Figs. 4.3, where the packing fraction $\phi \approx 0.25$, and Fig. 4.4, where the packing fraction $\phi \approx 0.08$.

We see from figure 4.3 that at both low motility and weak elastic interactions($A = 1$), particles do not form any ordered structures but are distributed uniformly in space, over the utilized simulation time. As motility is increased ($Pe \geq 10$), particles are seen clumping up at the boundary with their orientation vectors facing the wall at which they are localized. This is a familiar result of confined active Brownian particles (ABPs) wherein these tend to point towards the wall until their orientation is sufficiently randomized by the rotational diffusion[124]. As elastic interactions are dialed up such that the motions resulting from the dipolar interactions are much stronger than the stochastic diffusion of the system, structures characteristic of dipolar interactions emerge. In the case of low particle motility ($Pe = 1$), and high elastic interactions, we see a branched network form. In the case of intermediate motility ($Pe = 10$), networks are broken down into a single traveling cluster. In the former case, the particles comprising any given chain can either be oriented parallel (0) or anti-parallel (π) with respect to one another as the dipolar interaction is head-tail symmetric. In the latter case, networks form at short timescales and are compressed into one motile cluster at long timescales. This motile cluster contains numerous defects (shown by their different color) - particles oriented anti-parallel to the direction of cluster motion - caused by the earlier stage of network formation. Lastly, in the case of high particle motility ($Pe = 100$), particles assemble into traveling flexible chains which predominantly move parallel to the confining boundary and undergo inter-chain collisions in the bulk. Much of our forthcoming analysis is focused on these highly ordered, yet highly dynamic, structures.

At low packing fraction (Fig. 4.4), for $A = 10$ the elastic interaction between the particles is low and they diffuse around in the simulation space which is in contrast to what we see for higher packing fraction (Fig. 4.3) where particles show alignment with weak attraction. Accumulation of the particles can be seen at the confining boundaries which is attributed to the activity of the particles. Upon increasing the elastic strength to $A = 50$, formation of chains has been observed. At $Pe = 1$, long and branched chains of particles are formed. Increasing motility leads to a decrease in length of the chains and an increased polarity. At even higher elastic strength of $A = 200$, long chains with multiple branches are seen for $Pe = 1$. At increased activity, the chains stick to each other and form an ordered cluster that moves coherently in the direction determined by the net polarity of the constituent particles.

4.4.2 Pair correlations reveal spatial organization of active chains

To quantify the spatial distribution of particles around their neighbors, we calculate the pair correlation function, $g(r, \theta)$, the probability of finding a neighboring particle at a distance r in a direction θ from the central agent's orientation axis. We calculate this quantity by averaging over the positions of all agents over time and binning every other agent according to its separation vector (both distance and angle) from the current central agent. Finally the distribution is normalized such that $g(r, \theta)$ approaches 1 for distance r going to infinity. We then analyze the peaks in (r, θ) space. Fig. 4.5 shows four such distance and angle dependent maps in the space of motility and elastic interaction. Elastic interactions localize the peaks of the pair correlation function. When motility is low, particles form branched networks, and the primary configuration of particles is in straight chains. In this case, there exists two prominent peaks in the pair correlation function at (σ,0) and (σ,π). When both motility and elastic interactions are high, particles form into flexible traveling chains that have a tendency to join one another in a parallel fashion with an offset - a configuration that is energetically favorable to the elastic interaction and can be seen prominently in the simulation snapshot corresponding

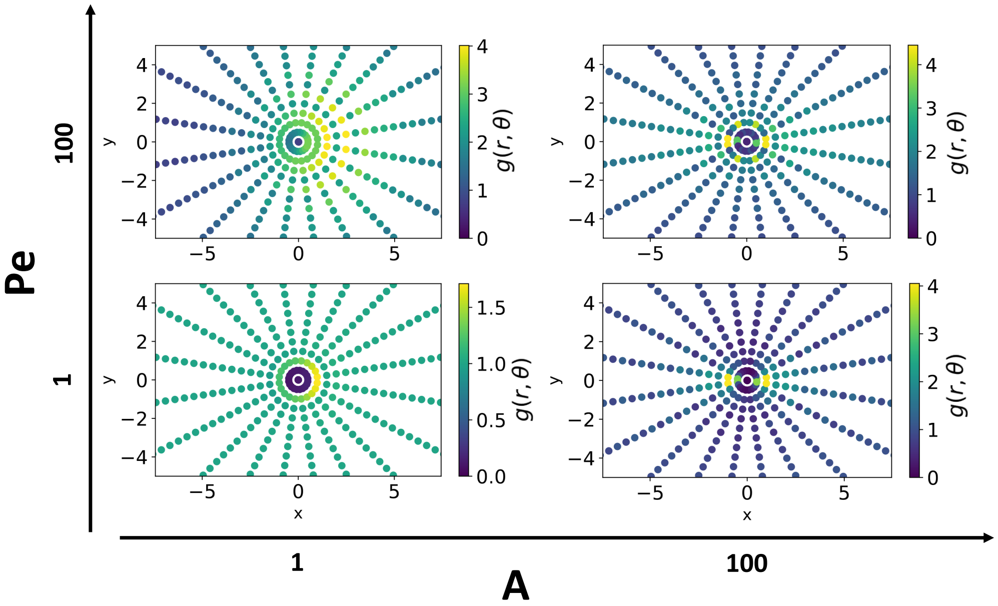

Figure 4.5: Angular dependent pair correlation function is affected by both motility and elastic interactions. Strong elastic interactions promote pair correlation peaks at $(r, \theta) =$ (σ,0) , (σ,π). At $Pe = 1$, these are the only prominent peaks in the pair correlation function. Motile activity gives rise to secondary peaks at roughly $(r, \theta) =$ (σ,$\frac{\pi}{3}$ mod π), (σ,$\frac{2\pi}{3}$ mod π) as the preeminent structures are bundles of offset traveling chains. Weak elastic interactions broaden the pair correlation distribution. In this case, motility breaks head-tail symmetry, and peaks can be seen at multiple integers of particle diameter at the head ($\theta = 0$ axis).

to $A = 100$ and $Pe = 100$ in Fig. 4.3. In this case, the primary peaks still occur at (σ,0) and (σ,π), but secondary peaks are present at (σ,$\frac{\pi}{3}$ mod π) and (σ,$\frac{2\pi}{3}$ mod π), indicating the offset parallel band structure. Low elastic interactions constitute the more familiar case of collections of repulsive ABPs. In this regime, the head-tail symmetry characteristic of the elastic interactions is broken as particles are more likely to encounter other particles along their direction of propulsion [125]. There exists a single prominent peak at the head of the dipole that monotonically decreases on either side of the head axis. Increasing motility in the ABP system adds layers to the single peak function in integer multiples of particle size σ as collision frequency increases.

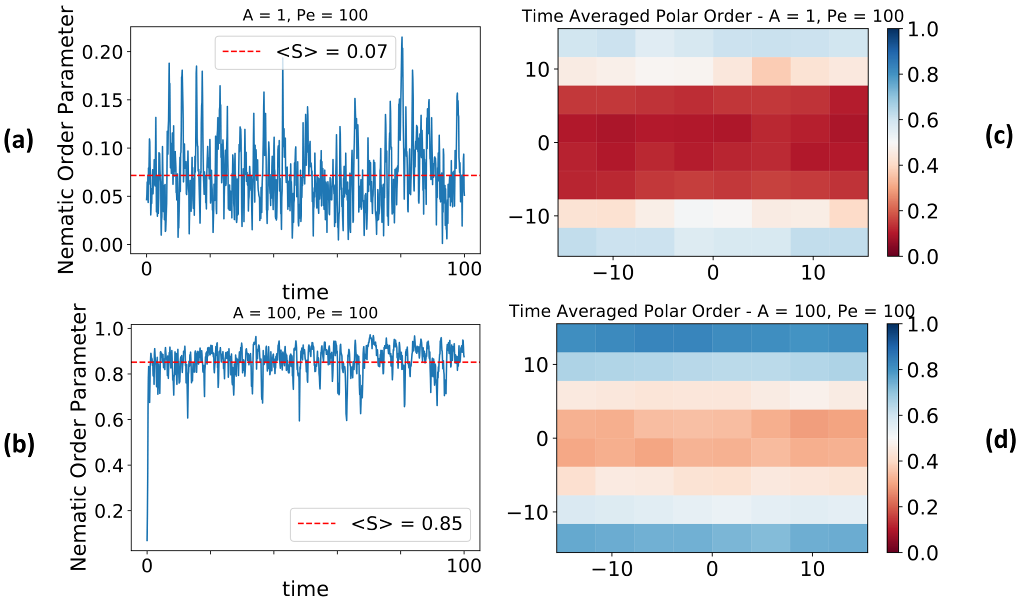

Figure 4.6: Elastic interactions promote global nematic order and local polar order. (a) Global nematic order, measuring the overall alignment of the particles' dipole axes, vs. time for low effective elastic interaction and high activity. Average global nematic order is negligible for these parameters. (b) Global nematic order vs. time for high effective elastic interaction and high activity. The system quickly gains a persistent global nematic order parameter near unity because the chains align parallel to each other. (c) Spatial distribution of time averaged polar order, where grid size is 3.75σ x 3.75σ, measuring the overall orientation of motility for the particles, for a characteristic run at low effective elastic interaction and high activity. Particles accumulate at the boundary and exhibit polar order along that boundary. This order rapidly decays away from the boundary and there is virtually no polar order observed in the bulk. (d) Spatial distribution of time averaged polar order, where grid size is 3.75σ x 3.75σ, for a characteristic run at high effective elastic interaction and high activity. A polar order near unity is observed at the boundary and persists into the bulk where near the middle of the channel $|p| \approx 0.3$.

4.4.3 Activity and elastic interactions promote orientational order

At higher interaction strength, A, and higher motility, Pe, we see chains that move parallel to each other forming polar bands at high density (top right of Fig. 4.3). Since chains are elongated objects, a collection of them can give rise to orientational order, similar to active nematic and polar states that result from active, anisotropic particles [101]. This type of order is commonly seen in active matter comprising suspensions of cytoskeletal filaments and motors [126]. To quantify the orientational order in these cases and to distinguish from the individual ABPs under confinement, we measure the nematic and polar order for these states. The magnitude of the nematic order parameter is defined as an average over the orientation of all particles, $S \equiv 2\langle\cos^2\theta\rangle - 1$, where θ is the angle between a particle's orientation and the average director. In this case, the global alignment direction is parallel to the confining boundaries given by the $x-$ axis. The nematic order tells us how well the dipoles are aligned, without distinguishing between the head and tail and contains no information about the motility direction. To quantify the oriented motion, we calculate the polar order, whose magnitude is given by, $|p| \equiv \sqrt{\langle n_x\rangle^2 + \langle n_y\rangle^2}$, where n_x and n_y are the x and y components of the orientation vector, $\hat{\mathbf{n}}$, respectively. This quantity is higher if the particles are oriented in the same direction, in addition to being aligned. While nematic alignment is encouraged by the passive dipolar interactions, active motility induces polar order.

Fig. 4.6(a,c) shows the global nematic order in time and Fig. 4.6(b,d) shows the time averaged spatial map of the polar order parameter, calculated by subdividing the simulation box into regions of dimension 3.75σ x 3.75σ, for both ABPs and traveling flexible chains. In the ABP system, the global nematic order is small due to the tendency of particles at the walls to be oriented orthogonal to the wall and those in the bulk to be oriented parallel to the wall, as well as the presence of orientational fluctuations from rotational diffusion. Traveling flexible chains of dipolar particles exhibit a global nematic order close to unity as all particles in this system tend to point along a director parallel to the confined boundary. Spatially resolving the average magnitude of the polar order parameter gives us a picture of particle alignment at a smaller length scale. ABPs exhibit polar alignment at the boundary. This alignment quickly diminishes, and no polar order is seen in the bulk. Traveling chains form bands at the boundary such that

$p > 0.7$ up to 6σ away from the wall. The polar order of these flexible chains drops off far less drastically in the bulk than the ABP system.

4.4.4 Transport properties of active chains are distinct from single particles

The mean-squared displacement or MSD is a typical metric that quantifies how motile entities cover space in time. In Fig. 4.7, we report the MSD for simulations with a packing fraction $\phi \approx 0.08$ in a square box of size 30σ, corresponding to the structures shown in Fig. 4.4. Given the confinement along one direction, we calculate the MSD separately for the confined (y-) and unconfined (x-) directions. The unconfined MSD, $\langle x^2 \rangle$, for particles with low elastic interaction *e.g.*, at $A = 10$, shows similar trends to individual active Brownian particles [127]. At short time intervals, individual ABPs propel persistently in the direction of their orientation, leading to ballistic behavior. In Fig. 4.7a, we see such behavior at very short time scales which gave way to super-diffusive behavior at intermediate time scales, where particles are slowed down by collisions with other particles. At sufficiently long time scales, the particles are diffusive as the rotational diffusion randomizes their orientation. Increasing Péclet number increases the timescale for super-diffusive behavior as the persistence time is longer.

We see qualitatively different regimes in the MSD for particles with stronger interaction in Fig. 4.7b. At interaction strength $A \geq 100$, which leads to formation of long, stable chains, we observe larger-scale structures such as branches, clusters and networks in the simulation snapshots shown in Fig. 4.4. In this case, the particles show sub-diffusive behavior at shorter time scales when they are still moving individually in an uncorrelated manner and beginning to form these structures. On the other hand, at longer time scales, they cluster into larger scale structures that move coherently in a specific direction like polar flocks, giving rise to a ballistic behavior. The crossover from subdiffusive to nearly ballistic behavior occurs earlier for higher Péclet numbers. At higher particle motility, we obtain ballistic behavior for all time scales. The resulting behavior is thus qualitatively different from single ABP behavior, which show a crossover from persistent to diffusive motion at timescales longer than the persistence time ($\sim Pe$). Here, on the other hand, the long time behavior is dictated by large-scale,

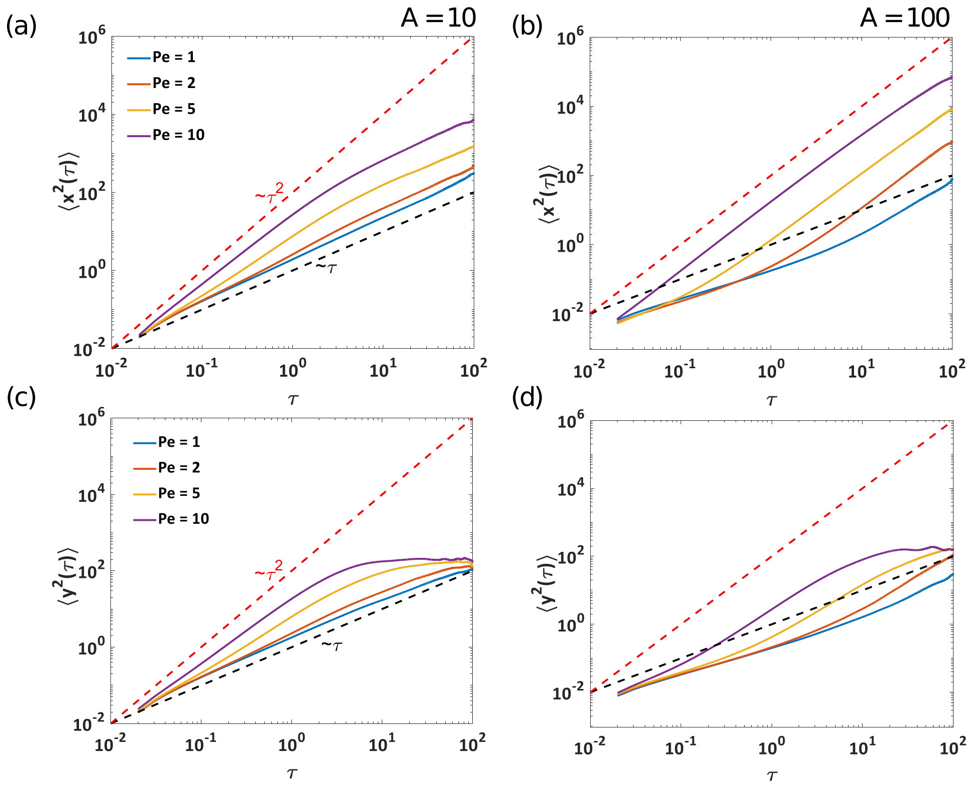

Figure 4.7: Mean-Squared Displacement or MSD vs. time interval, for 100 particles in a square simulation box of 30σ. Due to confinement of particles in y-direction, MSD is plotted separately for x and y components of displacement. (a), (b) MSD along unconfined direction: for $A = 10$, particles are super-diffusive at short time scale and diffusive at longer time scale, where the crossover time scale is determined by the Péclet number (Pe) of the particles. At $A = 100$, particles align themselves to form chains or clusters. At low Pe, the particles show sub-diffusive behavior at shorter times and ballistic behavior at longer times. At higher Pe, the ballistic behavior of particles is observed at all time scales. (c), (d) MSD along confined direction: particles reach the confining boundary at shorter times for high Pe number, and also at low elastic interactions A. At higher A, particles chain up and move predominantly parallel to the confining boundary.

polar structures that self-assemble irreversibly and move persistently at long times.

The MSD in the confined direction, $\langle y^2 \rangle$, plateaus off at long times, both for the individual ABPs (Fig. 4.7c) and the larger scale structures (Fig. 4.7d). The time scale to reach a plateau in the MSD corresponds to the time it takes an entity to reach the confining walls from the bulk of the simulation box. Thus, $\langle y^2 \rangle$ reaches a plateau at a shorter time scale for highly motile particles, as compared to the less motile ones. Due to the confining wall in the y-direction and strong alignment with neighboring particles at $A = 100$, the particles line up into chains that orient and move parallel to the confining walls, and not as much in the y-direction. Thus, $\langle y^2 \rangle$ for $A = 100$ reaches the plateau later than for the $A = 10$ case, for corresponding values of Pe.

4.4.5 Collisions of active chains reveal stable, mobile structures

We observe from simulations at low packing fraction (Fig. 4.4) that once particles self-assemble into chains, these can intersect to form junctions and get organized into larger-scale polar structures. We now explore in more detail the inter-chain interactions responsible for this self-organization. To do this, particles were initialized in an ordered chain and oriented in the same direction. Two such chains were oriented initially at different angles to control their approach direction, as shown in the insets in Fig. 4.8.

At $A = 200$ the junctions formed by chains depended on the Péclet number and the angle and position of approach. The 'Y' junction was the most observed for all Péclet number, which is formed from when the second chain attaches itself at the middle of the first chain (Figure 4.8, top left). An 'eye' (Figure 4.8, top right) is formed from two closely spaced 'Y's, which is observed for higher Péclet number, $Pe = 5$ and 10 and when the chains are oriented in the same direction. Again, at low particle motility $Pe = 1$, the chains upon colliding head on form a longer and more rigid chain (Figure 4.8, bottom left). On the other hand, at $Pe = 5$ chains show buckling upon undergoing head on collision which leads to a propelling 'necklace' (Figure 4.8, bottom right). At even higher Péclet number, the force between the particles is overpowered causing particles to detach from a chain and thereby creating defects. All these cases have been observed for $A = 200$. These junctions are also observed at lower elastic strength $A = 50$ and 100 but were unstable giving rise to many defects. Chains may interact with each other in

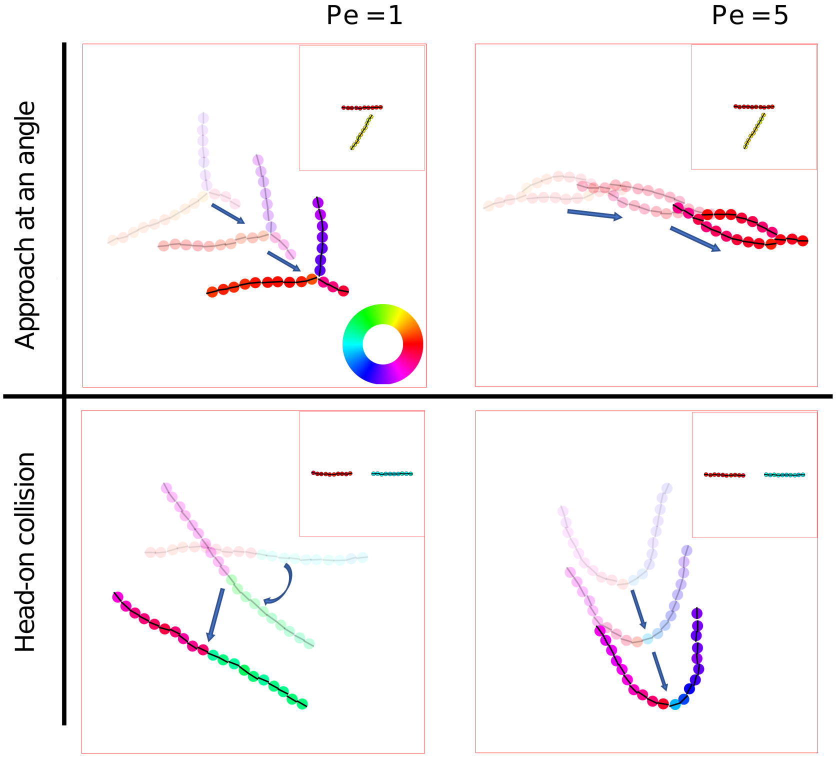

Figure 4.8: Interaction of two motile chains. Two straight chains of 10 particles each are initialized to approach each other at an angle of $\frac{\pi}{3}$ and also π (“head-on”) at $Pe = 1$ and 5. At $Pe = 1$, a ‘Y’ junction forms for an approach angle of $\frac{\pi}{3}$ whereas at $Pe = 5$, an ‘eye’ (two junctions) occurs. Upon head-on collision, a longer fluctuating chain with negligible net motility results at $Pe = 1$, and a propelling, buckled shape is observed at $Pe = 5$. Insets at the top corners represent the approach of the chains. Color represents angle of orientation of particles. The arrows indicate progression in time and suggest that the configurations are both stable and motile.

a head-tail fashion which results in a stable longer chain. Chains with multiple defects have also been observed to form these ‘Y’ and ‘eye’ structures at $A = 200$ and $Pe = 1$ (Figure 4.4).

4.4.6 Stronger confinement in narrow channels reveals polar clustering dynamics

In our system of traveling flexible chains comprised of strongly interacting and highly motile dipolar particles ($A = 100, Pe = 100$), bands that form along the confining boundary are relatively stable compared to those that form in the bulk. The latter are subject to more frequent collisions with other traveling chains. In order to gain understanding of these chain collision dynamics, we confine the same number of particles into a channel of width $L_y = \frac{L}{3}$, where L is the box size of our original simulation space, in order to induce more frequent and global chain-chain collisions. In this system we find a cyclic tripartite state dynamic. As shown in figure 4.9a, at some point, the particles with orientations $+x$ become well mixed with particles with orientations $-x$. The particles will then separate into lanes according to their polarity so that they can move unimpeded. These lanes will then collide which initializes another well mixed system and the cycle repeats.

This effect of colliding lanes can be seen quantitatively by tracking the magnitude of the polar order parameter averaged over boxes of width 3σ and height 2.5σ in time shown in figure 4.9b. The well mixed system has an average polar order parameter of $p \approx 0.2$. The system then phase separates into lanes with average polar order parameter ≈ 0.6. The $+x$ and $-x$ lanes collide, and the resultant combination has an average polar order parameter ≈ 0.4. When the channel is sufficiently wide, collisions between opposite lanes are less common, and the average polar order is bolstered by persistent polar chains at the confining boundary as seen in Fig. 4.9c. This time dependent formation and disbanding of polar structures is consistent with bead spring simulations of semiflexible filaments in the high activity regime [128].

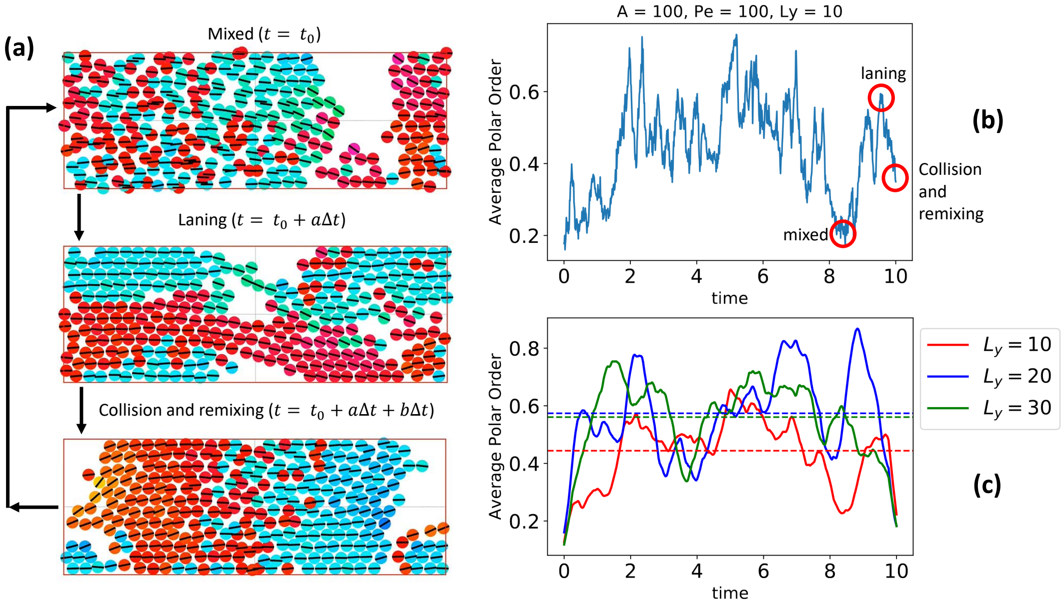

Figure 4.9: Traveling chains in a narrow channel exhibit cycles of mixing, laning, and collision and remixing. (a) Snapshots of a simulation where channel width has been decreased by a factor of 3. Dynamics of the system are encompassed by three cyclic states: A mixed state shown at an arbitrary initial time t_0, a phase separated laning state shown a short time after t_0, and a collision and remixing state shown a short time after the laning state. (b) Polar order averaged over boxes of width 3σ and height 2.5σ versus time is shown to elucidate the three states described in (a). The polar order for a mixed - laning - collision and remixing cycle are shown in the red circles. When the system is well mixed, the average polar order is small ($p \approx 0.2$). When the particles separate into lanes, the polar order increases rapidly ($p \approx 0.6$). When the lanes then collide and begin remixing, the remnants of the bulk of the lanes provide polar order while mixed particles and the interface between lanes decreases polar order ($p \approx 0.4$). (c) Polar order averaged over boxes of width 3σ and height 2.5σ versus time for three channel widths. Time averaged polar order, shown in dashed horizontal lines, is similar for the $L_y = 20$ and $L_y = 30$ cases when collision dynamics occur in the bulk, but non-interacting traveling chains line the boundaries. Time averaged polar order is smaller for the $L_y = 10$ case as collision dynamics are global phenomena.

4.5 Methods

Here, we present the equations governing the motion of the active motile particles discussed earlier and their interaction via the elastic substrate on which they move. In our model, we treat the particles as circular active Brownian particles (ABPs) that interact with other particles via long-range substrate modulated interactions and direct short-range particle-particle steric contact interactions. Long range interactions arise as each ABP exerts a contractile stress dipole $\mathbf{P}$ on the flat, semi-infinite, linearly elastic, isotropic substrate, thereby inducing strain fields which induces an effective force on nearby particles. For simplicity, we assume that the dipole axis is coincident with the direction of motion of the particle. For instance, in an elongated cell, the force dipole axis coincides with the orientational axis of the cell, that is also the direction of self-propulsion.

In the derivation that follows we use Einstein summation convention over the Latin indices, while Greek indices are used to label the particles. Consider a particle α that deforms the substrate. The work done by the associated dipole, $\mathbf{P}^{\alpha}$ in deforming the substrate in the presence of the strain created by a second dipole $\mathbf{P}^{\beta}$ (generated by a second particle β) is given by [31],

$$W_{\alpha\beta} = P^{\beta}_{ij}\partial_j\partial_l G^{\alpha\beta}_{ik}(\mathbf{r}_{\alpha\beta})P^{\alpha}_{kl}, \tag{4.2}$$

where $\mathbf{r}_{\alpha\beta} = \mathbf{r}_{\beta} - \mathbf{r}_{\alpha}$ is the separation vector connecting the centers of particles α and β (Fig. 4.10) (c.f [114, 49]). The elastic half space or Boussinesq Green's function that gives the displacement field in the linearly elastic medium at the location of one particle caused by the application of a point force at the location of the other is given by [29],

$$G^{\alpha\beta}_{ik}(\mathbf{r}_{\alpha\beta}) = \frac{1+\nu}{\pi E}\left[(1-\nu)\frac{\delta_{ik}}{r_{\alpha\beta}} + \nu\frac{r_{\alpha\beta,i}r_{\alpha\beta,k}}{r^3_{\alpha\beta}}\right], \tag{4.3}$$

where E is the stiffness (Young's modulus) and ν is Poisson's ratio of the substrate. Given the linearity of the problem, superposition of strain fields each of which is obtained by using the Green's function (Eqn. 4.3) appropriately provides the net displacement at a test position due to particles around it.

Two particles in our model interact via a combination of pairwise long-range and short-range interactions. The long range interaction forces originate from the substrate-mediated, elastic dipole-dipole interaction potential, $W^{\alpha\beta}$. The short-range interactions

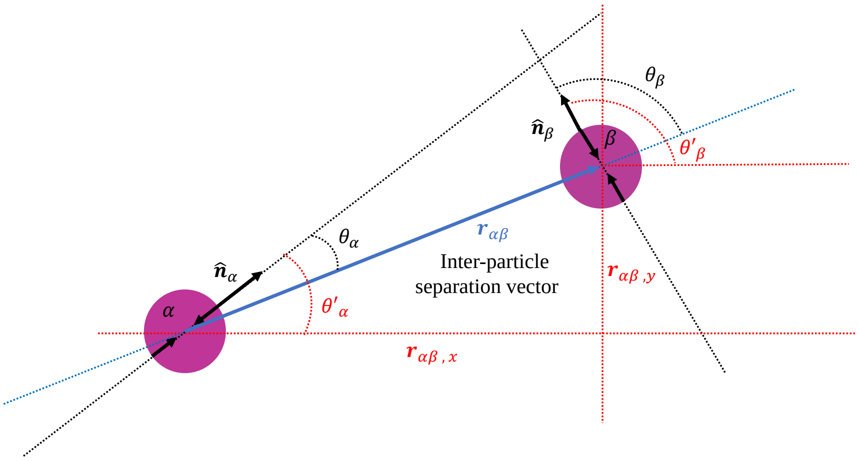

Figure 4.10: Schematic of two interacting particles with all relevant angles and vectors labeled. $\hat{\mathbf{n}}_i$ are unit vectors of force dipoles. θ'_i are angles of force dipoles with respect to the lab frame x-axis. θ_α and θ_β are angles of force dipoles with respect to their separation vector $\mathbf{r}_{\alpha\beta}$ which has components $\mathbf{r}_{\alpha\beta,x}$ and $\mathbf{r}_{\alpha\beta,y}$.

are steric in nature and prevent ABPs from overlapping. This functionality is achieved in the framework of our model by linear springs that only resist compression. Taken together, the total interaction potential between particles α and β can be written as,

$$\begin{aligned} W^{\alpha\beta} &= \frac{1}{2}k(\sigma - r_{\alpha\beta})^2, \quad \text{when} \quad 0 \leq r_{\alpha\beta} < \sigma \\ &= \frac{P^2}{E}\frac{f(\nu,\theta_\alpha,\theta_\beta)}{r_{\alpha\beta}^3}, \quad \text{when} \quad \sigma \leq r_{\alpha\beta} < r_{\text{cut}} \\ &= 0, \quad \text{when} \quad r_{\alpha\beta} \geq r_{\text{cut}}. \end{aligned} \tag{4.4}$$

where k is the spring constant of the linear (repulsive) spring preventing overlap, σ is the particle diameter (kept constant in our simulations), and r_{cut} is a cutoff distance beyond which the dipolar interactions are neglected. The magnitude of each force dipole is taken to be the same value denoted by P. The dependence of the pairwise dipolar interactions on the orientations of the two dipoles with respect to their separation vectors, and on the

Poisson ratio of the medium, ν, is expressed compactly in the expression [49],

$$f(\nu,\theta_\alpha,\theta_\beta) = \frac{\nu(\nu+1)}{2\pi}\Big(3(\cos^2\theta_\alpha + \cos^2\theta_\beta - 5\cos^2\theta_\alpha\cos^2\theta_\beta - \tfrac{1}{3}) \\ - (2-\nu^{-1})\cos^2(\theta_\alpha-\theta_\beta) - 3(\nu^{-1}-4)\cos\theta_\alpha\cos\theta_\beta\cos(\theta_\alpha-\theta_\beta)\Big). \tag{4.5}$$

where $\cos\theta_\alpha = \hat{\boldsymbol{n}}_\alpha \cdot \vec{\boldsymbol{r}}_{\alpha\beta}$ and $\cos\theta_\beta = \hat{\boldsymbol{n}}_\beta \cdot \vec{\boldsymbol{r}}_{\alpha\beta}$ are the orientations of particles, α and β, with respect to their separation vector, respectively (Fig. 4.10).

Motivated by natural and synthetic systems to which our model is applicable, we assume that the particles are in an over-damped viscous environment, and the inertia of the ABPs can be ignored. We can then write the equations of motion governing the translation and rotation, respectively, of particle α as,

$$\frac{d\mathbf{r}_\alpha}{dt} = v_0\hat{\mathbf{n}}_\alpha - \mu_T\sum_\beta \frac{\partial W^{\alpha\beta}}{\partial \mathbf{r}_\alpha} + \sqrt{2D_\mathrm{T}}\;\boldsymbol{\eta}_{\mathrm{T},\alpha}(t) \tag{4.6}$$

and

$$\frac{d\hat{\mathbf{n}}_\alpha}{dt} = -\mu_R\sum_\beta \hat{\mathbf{n}}_\alpha \times \frac{\partial W^{\alpha\beta}}{\partial \hat{\mathbf{n}}_\alpha} + \sqrt{2D_\mathrm{R}}\;\boldsymbol{\eta}_{\mathrm{R},\alpha}(t), \tag{4.7}$$

where $\mathbf{r}_\alpha$ and $\hat{\mathbf{n}}_\alpha$ are the position and orientation of particle α, respectively. In the equations above D_T and D_R are the translational and rotational diffusivity quantifying the random motion of a single particle, respectively. The viscous environment results in the translational and rotational mobilities, μ_T and μ_R respectively. Random white noise terms $\boldsymbol{\eta}_\mathbf{T}$ and $\boldsymbol{\eta}_\mathbf{R}$ have components that satisfy $\langle \eta_{i,\mathrm{T}}(t)\eta_{j,\mathrm{T}}(t')\rangle = \delta(t-t')\delta_{ij}$ and $\langle \eta_{i,\mathrm{R}}(t)\eta_{j,\mathrm{R}}(t')\rangle = \delta(t-t')\delta_{ij}$. Since the fluctuation dissipation theorem is not necessarily satisfied for a nonequilibrium system, the translational and rotational diffusivity are independent of each other. However, to reduce the number of free parameters and in the interest of simplicity, we assume that $D_\mathrm{T} = \sigma^2 D_\mathrm{R}$ and $\mu_\mathrm{T} = \sigma^2\mu_\mathrm{R}$. This allows the definition of an effective temperature, $k_B T_\mathrm{eff} = D_\mathrm{T}/\mu_T$. Finally we emphasize that each particle is endowed with the same dipole strength, P, and self-propulsion velocity, v_0, both of which are constant.

We now choose the cell diameter σ, the diffusion time, σ^2/D_T, and the effective thermal energy that quantifies the strength of stochastic fluctuations, D_T/μ_T, as physically relevant length, time, and energy scales in our model. Solutions to the scaled dynamical model are then dependent on three non-dimensional numbers,

$$Pe = \frac{v_0\sigma}{D_\mathrm{T}},\ A = \frac{\mu_T P^2}{E\sigma^3 D_\mathrm{T}},\ k^* = \frac{\mu_\mathrm{T} k\sigma^2}{D_\mathrm{T}} \tag{4.8}$$

where Pe is the Péclet number that is a measure of the self-propulsion in terms of the diffusion of motile particles, A is an effective elastic dipole-dipole interaction parameter, and k^* is the nondimensional steric spring constant.

Nondimensional forms of the dynamical equations Eq. 4.6-4.7 are discretized and numerically solved using the explicit half-order Euler-Maruyama method [129]. We use a time step of $\Delta t = 10^{-4}$ for a total of $10^5 - 10^6$ timesteps corresponding to a total simulation time of $10 - 100$. Each particle was initialized with a random position and orientation in our simulation box of size $L_x = 30\sigma$ and $10\sigma \leq L_y \leq 30\sigma$ with periodic boundary conditions in x and confinement modeled by repulsive springs identical to those used for particle-particle steric repulsions, with a fixed spring constant, $k^* = 10^4$, placed along the top and bottom walls. In our simulations, we want particles near each other to interact via the elastic potential at every time step, and to ensure that the overlap of particles is minimized. Furthermore, to ensure that the particles are not subject to unphysical repulsive forces, we choose k^* such that $k^*\Delta t = 1$. The higher order structures formed by the particles at different k^* are qualitatively similar when the timestep is appropriately rescaled. A and Pe are varied and analyzed in the Results section of the text.

4.6 Discussion

We have shown the typical collective behavior that emerges when active particles interact with each other as dipoles, using Brownian dynamics simulations. This minimal model is inspired by collective cell motility on elastic substrates where the cell-cell interaction is mediated by their mutual deformations of the passive substrate. While some of the emergent collective structures have analogs in cell culture experiments, such as the network organization of endothelial cells [62], our model is not intended to capture any specific biological behavior. We expect the first tests of our model to happen in dilute cell culture experiments that measure both pairwise cell interactions and substrate traction forces as in Ref. [23, 24].

The passive dipolar interactions lead to the end-to-end alignment of the particles into motile chains, which can be mutually aligned into polar bands and clusters because of their active motion. Polar chains that travel in opposite directions would be sorted into bands that get out of each other's way. These basic implications of our model, while specifically demonstrated here for elastic dipoles, belong to a broader class of active particles with dipolar interactions [109, 44, 130], and may therefore also be experimentally realized in active colloids endowed with permanent or induced dipole moments [45, 131]. We note that the symmetry of the elastic dipolar interactions is modified at higher Poisson's ratio [49], which is expected to result in structures such as active rings with rotational motion. This richer behavior with elastic interactions is a direct consequence of the tensorial, as opposed to vectorial nature of the elastic dipoles, in contrast with magnetic or electric dipoles, and will be the subject of future study. We further note that the mechanical interactions between cells in elastic media is, in reality, expected to include effects not considered here including from the nonlinear elastic properties of the substrate and nonlinear effects arising from the cells actively maintaining mechanical homeostasis at their boundaries, such as by regulating their shape [132]. We also ignore the elastic response of the cells themselves, which can give rise to additional interactions similar to that between rigid inclusions in soft media [133].

We focused on the strong elastic interaction cases in the dilute regime, where the self-assembly and dynamics of single chains can be studied. Since the chains are stable in this regime, they resemble other active polymer systems [126], that typically arise in gliding assays of biological filaments [134] or with synthetic colloids [106]. Polar bands are also seen at a higher density of active polymers [128]. However, in our system where these chains are self-assembled by dipolar interactions, multiple chains can stick to each other at higher interaction strength, while they can also fall apart, when colliding at high motility. By showing how a pair of chains interact with each other, we show the stable higher order structures that form and contribute to the polar clusters seen at higher density. Although not investigated in detail here, it will also be interesting to explore the bending dynamics of a single active polymer [135, 136] and characterize how the bending rigidity increases with dipolar interaction strength or decreases with particle motility.

To conclude, we note that our cell mechanobiology-inspired model also realizes a new class of active matter with long-range dipolar interactions. The emergent self-organization behavior distinct from the two typically studied pathways to the clustering of active particles: motility-induced phase separation [10], and Vicsek-style models [137]. In the latter, particle alignment is imposed in an agent-based manner, whereas here alignment emerges as a natural consequence of physical interactions.

Chapter 5

Off-axis propulsion and stochastic buckling drive chiral motion of active filaments

Note the code used for the forthcoming Brownian dynamics bead-spring chain simulations was written by Madhuvanthi Athani [138, 139].

5.1 Introduction

Chirality is a ubiquitous characteristic of nature observed across many biologically relevant length scales from the molecular scale wherein amino acid prevalence seems to highly favor the left-handed conformation [140, 141] to the subcellular and cellular scale [142, 143] to the scale of organism [144] wherein certain organs, for example, are consistently found on one side of the midline. A recent result suggests that symmetry breaking at all scales may be the result of a small set of motor proteins [145]. This left-right asymmetry is present from early stages of embryogenesis [146].

Several living systems that exhibit chirality have been of great interest to both the physics and biology communities. Examples include bacteria which form static spiral structures as a result of proliferation [147] and dynamic vortical structures in their collective motion [148, 149]. Furthermore, crystalline formations of starfish embryos were recently found to preferentially rotate in a coordinated fashion [150]. In addition to being seen in collective systems, single filament rotation has also been observed in experiments of actin gliding on myosin motors bound to lipid bilayers [151].

Here we take inspiration from a recent experimental result which shows that kinesin propelled microtubules on gliding assays exhibit persistent rotation of the nematic director characterizing their collective orientation [152]. Preliminary image analysis of dilute gliding microtubule assays, where the density of filaments is not high enough to form orientationally ordered phases, likewise suggest directionally biased rotation. While there have been several mechanisms proposed for this rotation such as motor induced filament curvature [153] and collision induced torque [154], there is not yet consensus as to which modalities and to what degree govern both the single and collective filament rotations observed in these gliding microtubule experiments.

Microtubules are comprised of stacks of strings, called protofilaments, made up of a succession of heterodimers of the protein tubulin. Depending on how many protofilaments make up the microtubule, the orientation of the protofilaments may be exactly parallel to the axis of the microtubule, as is in the case of microtubules with thirteen protofilaments (MT 13), or there may be a helical wrapping of the protofilaments, as is the case for non-MT 13 microtubules, where the deviation from thirteen sets both the direction and degree of twist of the protofilaments [155]. Kinesins are motor proteins that bind to microtubules and hydrolyze ATP to walk along the filaments. Kinesin walk, primarily, along protofilaments taking steps alternating between α and β tubulin. We thus posit that one of the contributing factors to observed rotation of microtubules in gliding motility assay experiments is the action of kinesin on a single microtubule. The instantaneous propulsive force on a given microtubule from a motor is not directly along the long axis of the microtubule, but at some small angle determined by the helicity of the protofilaments comprising the microtubule. This angle should be non-zero in filaments where the number of constituent protofilament differs from thirteen [156].

5.2 Model and Results

5.2.1 Off-axis propelled bead-spring chains show persistent rotation in the direction of offset

In this study, we utilize a bead-spring filament model and run two dimensional Brownian dynamics simulations (described fully in Refs. [138, 139]) where each bead has an active force v_0 along the direction of its local tangent, $\hat{\mathbf{n}}$, plus an angle, θ_{offset}, motivated by the action of an individual myosin motor walking along a helical path of tubulin heterodimers corresponding to a protofilament comprising the microtubule (Fig. 5.1a). Additionally, beads are connected to one other through Hookean springs that cannot easily stretch or compress and can bend with an energy cost, where the bending stiffness parameter, k_{bend}, is a main parameter of the model. We find, qualitatively, that flexible filaments exhibit a dynamic behavior in which a kink is nucleated by thermal fluctuations in an approximately straight filament thereby inducing a torque in the direction of offset. This torque induces a greater curvature in the kink which gives rise to an even greater torque in the direction of offset. All the while, the kink is travelling down relative to the filament due to propulsion until it is fully extruded thereby leaving the filament straight. This process, which will be described in more detail later, results in a net rotation of the filament (Fig. 5.1b). The aforementioned rotation modality is for unobstructed freely gliding filaments. Filaments, however, may well interact with obstacles, such as dead motors. In this case, a piece of the filament is rendered pinned. When this pinning occurs at the tail of the filament, the filament is subject to stretching forces and rotates in the direction of offset, while if the pinning occurs at the head, the filament is subject to compressive forces and rotates opposite the offset with greater magnitude (Fig. 5.1c).

The central parameters of the aforementioned model are the bending stiffness, k_{bend}, which can be tuned experimentally by both the polymerization and stabilization protocol of the microtubules [157, 158] and the offset angle, θ_{offset}, which is determined by the number of protofilaments that comprise the microtubule where thirteen protofilament microtubules (MT 13) have no measurable angular difference between the long axis of the filament and orientation of the constituent protofilaments and deviations about this

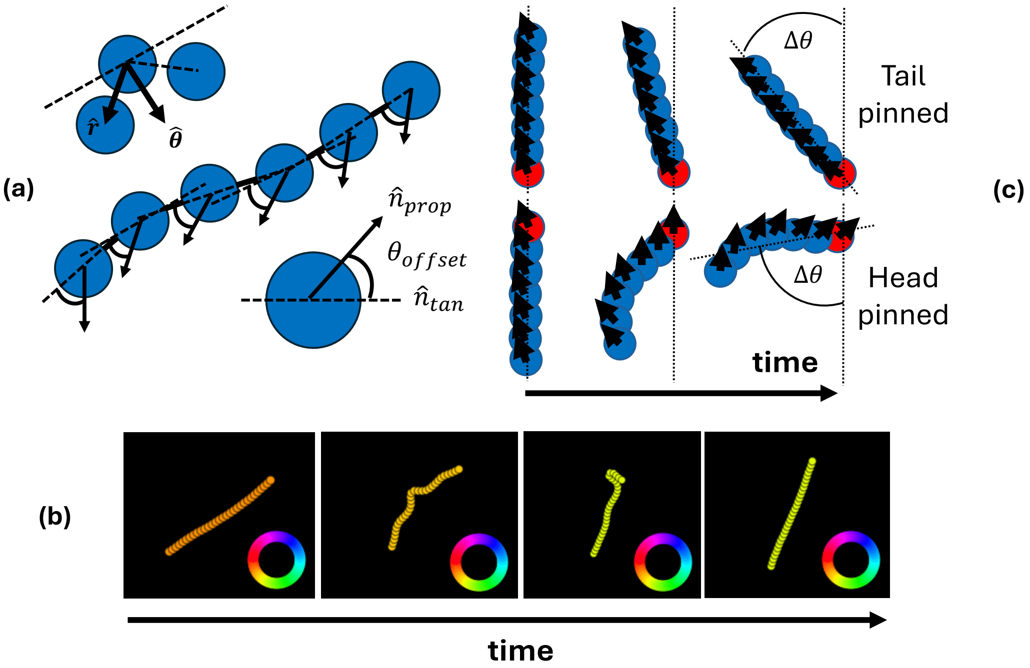

Figure 5.1: Free chiral active filaments (CAF) persistently rotate in the direction of offset propulsion, while pinning cases provide the full spectrum of rotation events. (a) Modified bead-spring model wherein each bead is driven at an identical angle, shown by arcs, relative to the local tangent direction. (b) Time lapse images of a characteristic rotation event of a freely gliding CAF where each filament is colored by its average orientation according to the inset color wheel. (c) Interaction with defects can give rise to tail pinned events (top) wherein the tail bead cannot translate which gives rise to filament stretching and rotation in the direction of offset, or head pinned events (bottom) wherein the head bead cannot translate which gives rise to filament compression and rotation in the direction opposite the offset.

number of protofilaments determine direction and degree of protofilament helicity [155]. We find that simulated filaments exhibit persistent rotation in the direction of the offset angle where rotation rate scales with magnitude of offset (Fig. 5.2 - left). Furthermore, given an offset angle, simulated filaments show greater rotation as they become easier to bend until they are too flimsy at which point they exhibit very little rotation (Fig. 5.2 - right). The justification and corresponding intuition for this emergent optimal bending stiffness will be discussed later.

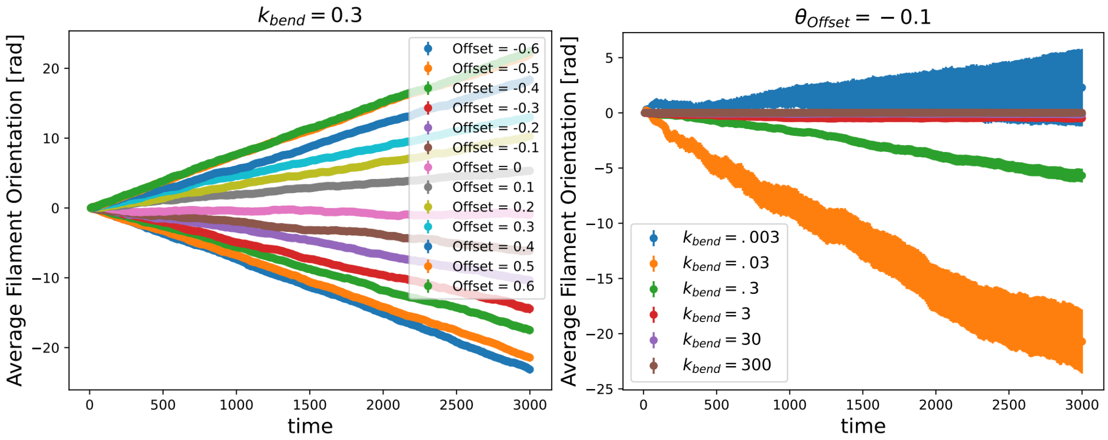

Figure 5.2: Off-axes driven filaments rotate in the direction of the offset propulsion. (Left) Flexible filaments ($k_{bend} = 0.3$) rotate more at larger offsets in the direction of offset. (Right) Filaments exhibit rotation rates that scale with bending flexibility until the filament is too flimsy ($k_{bend} = 0.003 - blue$)) at which point thermal fluctuations dominate. N = 100 simulations were run per curve.

5.2.2 Rotation dynamics are governed by a positive feedback between torque and curvature driven by kink nucleation and propagation

We have observed qualitatively that, rather than rotating in a smooth fashion at a fixed rate as would be the case with a tangentially driven filaments with an inherent curvature, off-axis driven filament rotation is characterized by bursts of high rotation events induced by curvature. To investigate this behavior quantitatively, we calculate the torque about the center of mass of the filament by the following:

$$\text{Torque}_{COM} = \Sigma_{i=0}^{N}(\mathbf{r}_{COM} - \mathbf{r}_i) \times v_0\hat{\mathbf{n}}_{prop}, \tag{5.1}$$

where i is the bead number that runs from the head bead ($i = 0$) to the tail bead ($i = N$), $\mathbf{r}_{COM}$ is the center of mass vector defined by $\mathbf{r}_{COM} = \frac{1}{N}\Sigma_{i=0}^{N}\mathbf{r}_i$ where $\mathbf{r}_i$ is the position of bead i, and $v_0\hat{\mathbf{n}}_{prop}$ is the propulsive force vector. Additionally, we calculate the curvature of each bead as

$$\text{Curvature}_i = \frac{\hat{\mathbf{n}}_{i,i+1} \times \hat{\mathbf{n}}_{i-1,i}}{|\hat{\mathbf{n}}_{i,i+1} \times \hat{\mathbf{n}}_{i-1,i}|} \arccos\left(\hat{\mathbf{n}}_{i,i+1} \cdot \hat{\mathbf{n}}_{i-1,i}\right)/\Delta s, \tag{5.2}$$

where $\hat{\mathbf{n}}_{i,i+1} = \frac{\mathbf{r}_{i+1}-\mathbf{r}_i}{|\mathbf{r}_{i+1}-\mathbf{r}_i|}$ is the local forward tangent and $\Delta s = |\mathbf{r}_i - \mathbf{r}_{i-1}|$ is the separation distance of beads i and $i-1$. Plotting the filament configurations of the three highest torque events in our sample reveals an accompanying high curvature event, or kink (Fig. 5.3a). Furthermore, plotting the full distributions of torque versus the curvature of the bead with the greatest curvature in the chain (Fig. 5.3b - left) shows that both the highest torque and curvature events occur in the direction of offset while plotting torque versus the average curvature of beads in the chain (Fig. 5.3b - right) confirms the direct relation between torque and curvature we would expect. Calculating the Pearson correlation coefficient of both maximum and mean curvature shows that while at zero offset mean curvature is entirely correlated with torque, the maximum curvature only becomes strongly correlated with torque at larger offsets where the proposed mechanism of kink nucleation followed by torque curvature feedback is prominent (Fig. 5.3c).

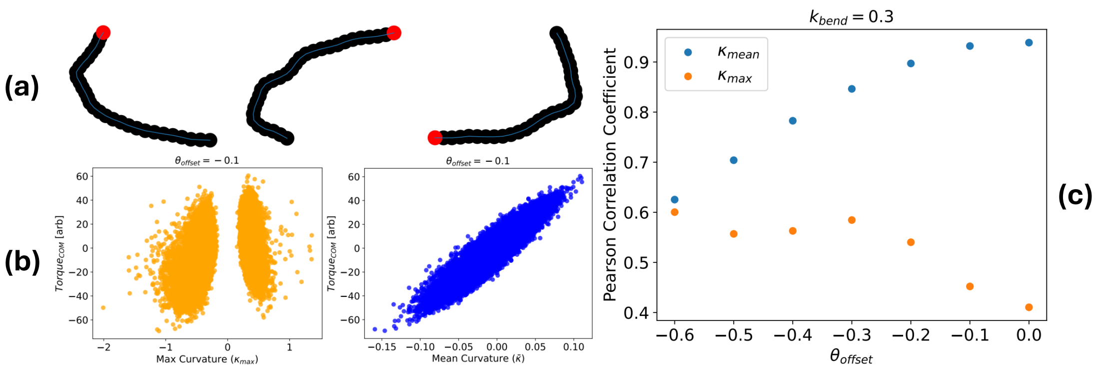

Figure 5.3: Torque about filament center of mass is correlated with curvature. (a) Snapshots of filaments corresponding to the three largest negative torque events where $\theta_{offset} = -0.1$, $k_{bend} = 0.3$, and the head bead has been colored red. Configurations show pronounced kinks, suggesting a torque-curvature correlation. (b) Scatter plots of torque about the center of mass of the filament as a function of max (left) or mean (right) indicate larger torque events being clockwise - in the direction of offset - and accompanied by greater curvature. (c) Pearson correlation coefficient as a function of θ_{offset} shows that while average curvature is consistently strongly correlated with torque, max curvature is more strongly correlated with torque at higher offsets, where cyclic kink nucleation, propagation, and extrusion is accentuated.

5.2.3 Offset propulsion aids onset of buckling

Analysis of bead resolved curvatures indicates that while almost no curvature is localized near the head of the chain, curvature increases smoothly toward the tail until a maximum is reached, indicating the position at which the kink defect is sharpest. Interestingly, while the position of the kink relative to the chain does not vary widely with θ_{offset}, the magnitude of the characteristic curvature increases monotonically with offset (Fig. 5.4 - left). In contrast with passive filaments undergoing solely thermal fluctuations which would be fully characterized by a Boltzmann distribution in bending energy and, therefore, a gaussian distribution in curvature, it has been found in previous analyses of actin gliding assays paired with models of active filaments that propelled filaments exhibit non-gaussian curvature distributions [159]. In this study, it was found that motor heterogeneity led to bursts of activity within the chain that induced buckling instabilities as evidenced by exponential tails in the filament curvature distributions. Similarly, we find that off-axis propulsion can aid in the onset of buckling. Additionally, we see that the exponential in the non-gaussian region scales with offset, indicating a chiral length scale (Fig. 5.4 - right).

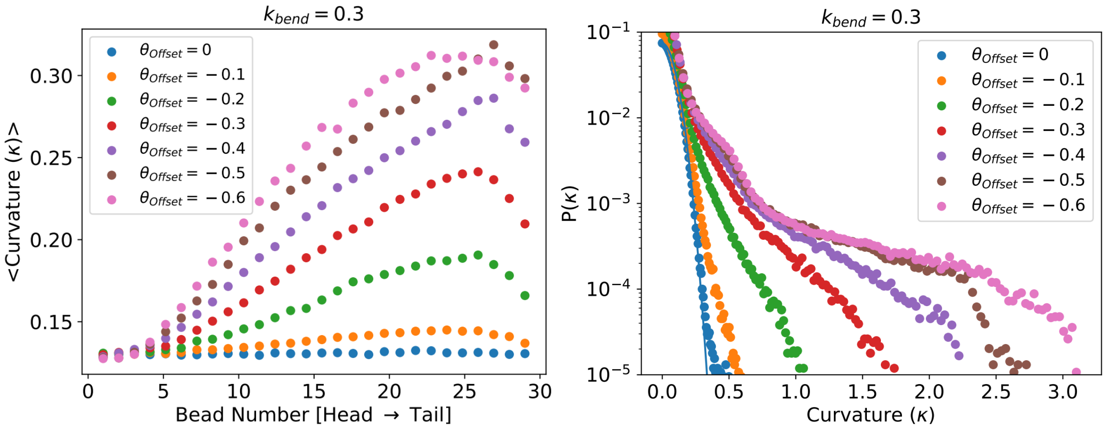

Figure 5.4: Curvature distributions suggest tail favored curvature and a chiral length scale. (Left) Bead resolved curvatures indicate high curvature events being localized to the tail of the filament. The magnitude of these high curvature events increases with magnitude of the offset angle. (Right) Nonzero offset filaments exhibit an exponential tail in their curvature distributions indicating a length scale emerging from activity induced chirality. N = 100 simulations were run per curve.

5.2.4 Optimal flexibility promotes robust rotation

The rotation mechanism we have discussed up to this point consisting of a kink nucleation event followed by a cycle of torque and curvature feedback ultimately being relieved by extrusion assumes a flexible filament. A phase diagram of rotation rates in the space of bending stiffness parameter, k_{bend}, and reduced temperature, $T*$, reveals a stripe corresponding to a fixed ratio $\frac{k_{bend}}{T*}$ that results in the greatest rotation rates (Fig. 5.5a,b). If a filament has too great a persistence length, thermal fluctuations will be insufficient to nucleate the kink that we know is needed for directed rotation events. Conversely, if the filament is too flimsy, the picture of a single kink parsing the filament into an active head segment that acts as a lever arm in these high torque events and a relatively stationary tail falters and a menagerie of thermal fluctuations saturates any coherent motion. It is only between these regimes wherein thermal fluctuations are prominent enough to induce a kink event and the filament is stiff enough to maintain roughly straight conformations on either side of the kink that give rise to rotation events as we have described them (Fig. 5.5c).

5.3 Summary, Discussion, and Future Work

Motivated by the lattice geometry of non-MT 13 microtubules combined with kinesin-1 motor proteins that walk along protofilament paths, we utilize Brownian dynamics to simulate single filaments driven at an offset angle relative to the filament orientation representative of the angle of microtubule supertwist as a coarse grained model of dilute microtubule gliding assays. We have shown that filaments modeled as bead-spring chains wherein each bead comprising the chain undergoes constant propulsion at an angle relative to the local tangent exhibit rotation. We have shown that this rotation occurs in the direction of the offset angle and that the magnitude of rotation increases with offset angle magnitude and is nonmonotonic in bending stiffness. We showed that rotation is characterized by cycles of kink nucleation, a positive feedback loop between torque and curvature, and kink extrusion via an effective reptation. We found that the location of greatest kink curvature is insensitive to offset, and the magnitude monotonically increases with greater offset. Lastly, we show that offset propulsion aids in active buckling

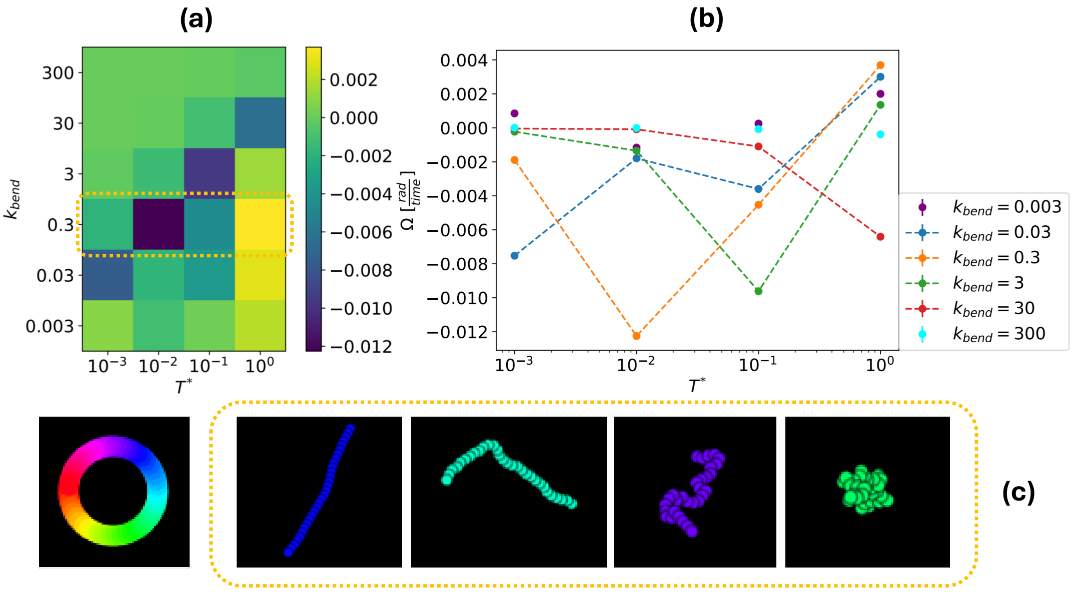

Figure 5.5: Phase Diagram reveals a persistence length at which rotation is optimized. (a) Phase diagram in bending rigidity and reduced temperature (k_{bend}, T^*) space where $\theta_{offset} = -0.1$. Dark boxes along the diagonal indicate large magnitude rotations in the direction of offset. (b) Plots of rotation rates at various bending rigidities as a function of reduced temperature. Those with dashed lines show pronounced minima within this interval of temperature while those which are purely points remain near zero over the temperature space. (c) A stripe of characteristic snapshots at $k_{bend} = 0.3$ for increasing reduced temperatures $T^* = 10^{-3}, 10^{-2}, 10^{-1}, 10^{0}$, where the beads are colored by the filament's average orientation. At very low temperature, the filament remains roughly straight and so largely translates diagonally. At very high temperatures, large thermal fluctuations produce globular structures. At intermediate temperatures, thermal fluctuations are strong enough to nucleate a kink in the filament which causes large rotation events. N = 100 simulations were run per parameter set in (a) and (b).

in the emergence of a chiral length scale revealed by curvature distributions.

The results we have presented were predominantly for negative offset angles which corresponds to left-handed supertwist [155]. We found that for such a helicity, one would expect clockwise rotation. Preliminary experimental analysis suggests, however, that for MT 14, whose lattice structure indeed indicates left-handed supertwist [160], as well as for a predominantly MT 12 system whose supertwist is right-handed, filament rotation is overall counterclockwise. This suggests that either there is another mechanism for chirality in dilute microtubule gliding assays or that, even for these systems, surface defects and/or the effects of motor heterogeneity, both of which could give rise to head-pinned rotation events which rotate opposite the free filament (Fig. 5.1c - bottom), are influential to differing degrees with respect to density and stiffness. A definitive check for the validity of our model would be running the same experimental conditions with motors pinned to both the top and bottom of the glass slide. If the statistics indicate the filaments are rotating in opposite directions, this will lend credence to our proposed mechanism.

Chapter 6

Final Discussion and Future Work

In this work, we have built minimal models, conducted agent-based Brownian dynamics simulations, and ran comparative data analyses of multicellular and cell component systems. We have found that purely mechanical models of motile agents were sufficient to consistently qualitatively recapitulate behavior of their *in vitro* experimental counterparts, occasionally quantitatively match the experimental system, and inspire new kinds of experimental systems yet to be realized.

In chapter 2, we coarse grained the focal adhesion coupled actomyosin force distribution of cells into a stochastic anisotropic contractile force dipole in elastic half-space. We found that simulations of this minimal mechanical approximate model gave rise to fractal network architectures in a density and substrate mechanical properties dependent way - a qualitatively similar result to those of cell cultures on hydrogels. Furthermore, we compared both global transport properties via the percolation probability metric and local morphological traits via the shape factor metric with collaborative cell culture experiments and found strong agreement between simulation and experiment over a broad range of packing fractions and substrate stiffness. This lends strong credence to the importance of substrate-mediated cell-cell elastic interactions in the early stages of vasculogenesis and cellular self-assembly. Future work includes considering both more realistic environmental conditions and laying the groundwork for engineered systems. For the former, this means considering not a purely linear, elastic substrate in two dimensions but a nonlinear, viscoelastic fibrous medium in three dimensions. The extracellular matrix is a three-dimensional environment comprised of cross-linked fibers as well as fluid in their interstices. While there could, indeed, be several ways to alter the model to describe the matrix more accurately, one such path would be to change the form of the Green's function so as to implement a memory kernel for strain propagation to handle viscoelasticity. Furthermore, coupling dipole orientation to a dynamic local nematic order parameter may be a viable strategy to compensate for the local directional bias of the fibrous ECM. As for engineered systems, another prominent future direction would be to consider a patterned substrate, that is, a medium with heterogeneous stiffness. Having spatial control over stiffness should, by our model predictions, allow for spatial control of cellular structure. Similarily, conducting cell culture experiments on materials of varying Poisson's ratio including metamaterials with negative Poisson's ratio would give insight into the corresponding characteristic cellular configurations. Realizing these engineering feats would give immense control to the assembly process and might allow for designed cellular architectures which would have potential applications to tissue engineering and medicine.

In chapter 3, we have shown preliminary results regarding the nonlinearity of force production and boundary stress of anisotropic dipoles embedded in a triangular mesh as a model for compaction of collagen gels by embedded fibroblasts. We showed that a model where cell contractility is sensitive to internal strain exhibits a weakly nonlinear boundary stress regime as a function of cell density. We have also shown that while model cells configured in a line decrease elastic energy with increasing density, randomly distributed cells with both random and specified orientations do no such minimization. The prime direction of future work on this project is then to pair the aforementioned results and plot a modified boundary stress that takes into account the probability of such a macrostate - as states which lower elastic energy would be more likely - by multiplying the corresponding boundary stress by a Boltzmann factor. This, we predict, will give a sharper transition of macroscopic contractility versus cell density that could explain global compaction seen in *in vitro* collagen gel experiments. If this is insufficient, there remain several avenues of nonlinearity to explore. Namely, motivated by collagen fiber behavior, making matrix springs easier to compress than to stretch may help accentuate the transition. It could also be that the feedback parameter itself need be a functional rather than a static value. Specifically, one could either implement a critical strain, internal or external, that must be surpassed before the activity feedback is applied. Similarly, a hard distance cutoff for a neighbor to upregulate its force production may be explored.

In chapter 4, motivated by a variety of synthetic and organic systems, we placed simulated motile elastic dipolar particles in a channel geometry. We found that at low elastic interaction strength, particles displayed typical ABP behavior, that is, they collected at the boundary forming clumps with polar order oriented orthogonal to the confining boundary. At high elastic interaction strength and low motility, they formed network structures similar to those studied in depth in chapter 2 of this dissertation. At intermediate activity, network structure occurred at early times and was followed by compaction into a master cluster. This cluster translated in the direction of the sum of the propulsion orientations of the constituent particles but was hindered by frozen-in defects of the opposing orientations. At high motility, dipolar particles self-assembled into flexible brittle motile polymers that formed protected polar bands at the confining boundaries and underwent highly dynamic reconfigurations in the bulk as the result of frequent collisions. Such highly motile substrate mediated interactive particles have yet to be realized in experiment, but bare resemblance to driven Janus colloid systems and constitute a novel active matter system with long-range interactions. Microfluidic devices may offer a fitting *in vitro* test bed for the dynamics seen in our simulations. Cell motility experiments in this environment wherein cell-cell contacts via cadherin mediated binding are suppressed may give rise to a portion of our phase space. Additionally, the dynamic behavior of highly motile dipolar particles - active transient chains - may hold general promise in therapeutics and drug transport as directed filament motility for fast transport and disbanding for substance release is desirable.

In chapter 5 we considered the shallow helical winding of non-MT 13 microtubules. We modeled the action of kinesin motors on such microtubules as a bead-spring chain with a propulsion on each bead given by the local tangent direction plus an offset angle. We found that simulated filaments rotate in the direction of offset angle with a magnitude that increases with magnitude of offset angle. We found that this rotary motion is governed by a cyclic process of kink nucleation followed by feedback between torque and curvature until the kink is extruded by which point a net rotation was achieved. This rotation was suppressed at both very high filament bending rigidity when the filament simply remained straight and translates diagonally, and at very low filament rigidity when thermal fluctuations washed out any coherent offset induced motion. These simulation predictions must be verified by single filament microtubule gliding assay experiments paying close attention to the presence of defects. As we have shown in the limiting cases of head and tail pinning, rotation events characteristic of these circumstances and the free filament are vastly different. The link between single filament behavior and collective nematic orientation rotation observed in dense suspensions needs to be explored in greater depth. More generally, the idea of offset driven filaments could hold promise in fields such as soft robotics. The transport properties that chiral chains without intrinsic curvature are capable of should be explored by engineered systems. Specifically, characterizing how these filaments navigate boundaries and behave in crowded environments could inform design principles of dynamically chiral particle chains.

Appendix A

SI - Chapter 2

A.1 Elastic dipole interaction model

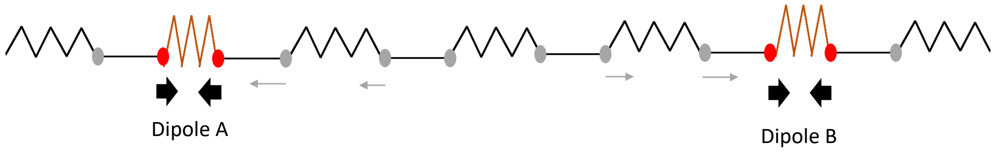

Supp. Fig. A.1: 1D spring model illustrating origin of elastic interaction potential between two contractile dipoles.

Consistent with adherent cell behavior on soft substrates, we assume our model cells are elongated and exert contractile traction forces at the poles of their long body axis. It is by this behavior that we model our cells as contractile force dipoles. The mechanical interaction between a pair of force dipoles is illustrated by the schematic in Fig. A.1 in the form of a 1D series of springs representing the effect of the elastic substrate. While the springs underlying the contractile dipoles are compressed, the springs between them are stretched. By moving to different positions in the medium for a given position of dipole A, the dipole B can reduce the net substrate deformation energy by compressing regions stretched by dipole A. This physical interaction between elastic dipoles considered here is analogous to the interaction of an electric dipole with the electric field induced by another dipole. A similar reciprocal force results on dipole A, since the interactions are based on an elastic free energy. The physical origin of this force is the tendency of the passive elastic medium to minimize its deformations in response to the active, contractile forces generated by the cells. We now assume these cells are on an isotropic, homogeneous, linear substrate in elastic halfspace of Young's modulus and Poisson's ratio E and ν, respectively, and derive the displacement field due to a coarse-graining of the traction forces on either side of the nucleus into single point like forces, $\mathbf{F}^1$ and $\mathbf{F}^2$ where $\mathbf{F}^1 = -\mathbf{F}^2$, separated by a distance a. Let the center of the force distribution lie at $\mathbf{r}'$. Then, by elasticity theory, the displacement at position $\mathbf{r}$ can be written

$$u_i(\mathbf{r}) = G_{ij}(\mathbf{r} - (\mathbf{r}' - \frac{\mathbf{a}}{2}))F_j^1 + G_{ij}(\mathbf{r} - (\mathbf{r}' + \frac{\mathbf{a}}{2}))F_j^2, \tag{A.1}$$

where G_{ij} is the Green's function that captures the displacement in the elastic medium at the location of one cell (dipole) caused by the application of a point force at the location of the other [29] defined as

$$G_{ij}(\mathbf{r}) = \frac{1+\nu}{\pi E}\left[(1-\nu)\frac{\delta_{ij}}{r} + \nu\frac{r_i r_j}{r^3}\right]. \tag{A.2}$$

Replacing $\mathbf{F}^1 = -\mathbf{F}^2 = \mathbf{F}$ in eqn. A.1 and performing a Taylor expansion about $\mathbf{r} - \mathbf{r}'$ to first order in $\mathbf{a}$ gives

$$u_i(\mathbf{r}) = \partial_k G_{ij}(\mathbf{r} - \mathbf{r}')F_j a_k = \partial_k G_{ij}(\mathbf{r} - \mathbf{r}')P_{jk}, \tag{A.3}$$

where $P_{jk} = F_j a_k$ is the force dipole representation of one of our cell's force distribution, ∂k is the partial derivative with respect to x_k, and terms of order $\mathbf{a}^2$ and higher have been neglected. We now write the strain by the derivatives of the displacement field as $u_{il}(\mathbf{r}) = \frac{1}{2}(\partial_l u_i(\mathbf{r}) + \partial_i u_l(\mathbf{r}))$, now substituting our symmetric Green's function, we can write the strain field as

$$u_{il}(\mathbf{r}) = \partial_l \partial_k G_{ij}(\mathbf{r} - \mathbf{r}')P_{jk}, \tag{A.4}$$

where the u_{xx} and u_{yy} fields are shown in Fig. A.2. Lastly, we note that that by coupling the strain field due to one cell in the proximity of another, we can write the work done by deforming the medium and thus an effective pairwise interaction potential energy given by

$$W_{\alpha\beta}(\mathbf{r}_{\alpha\beta}) = P_{il}^{\beta}\partial_k\partial_l G_{ij}^{\alpha\beta}(\mathbf{r}_{\alpha\beta})P_{jk}^{\alpha}, \tag{A.5}$$

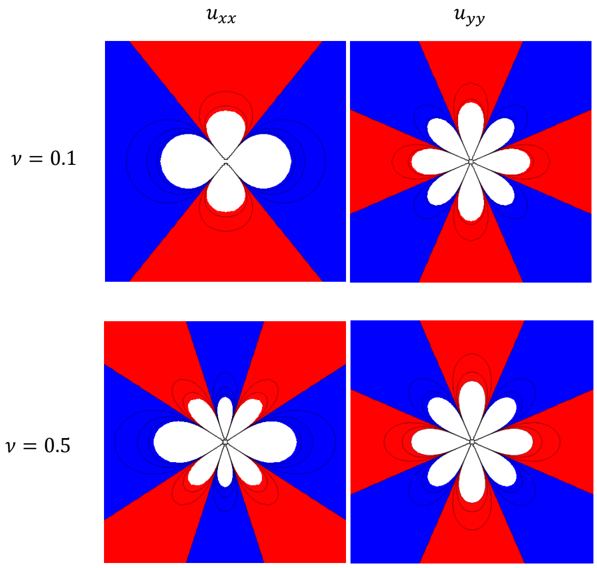

Supp. Fig. A.2: u_{xx}(left) and u_{yy}(right) components of strain field due to a contractile force dipole oriented along the $x-$axis in elastic half-space of a linear, isotropic medium. u_{xx} component shows the $\nu = 0.1$(top) map whose orientational distribution is that of an electric field from a quadrupole, while $\nu = 0.5$(bottom) resembles an electric octupole. u_{yy} has a similar structure for both shown values of Poisson's ratio, ν.

where P_α and P_β are the magnitude of the contractile force dipole exerted by cell α and cell β, respectively. E is the Young's modulus of the elastic substrate, ν is Poisson's ratio, and $\mathbf{r}_{\alpha\beta} = \boldsymbol{r}_\beta - \boldsymbol{r}_\alpha$ is the separation vector connecting the positions of cell dipoles, α and β.

By transforming to the separation vector coordinate frame, the cell-cell elastic potential can be written as [31]

$$W_{\alpha\beta} = \frac{P_\alpha P_\beta}{E r_{\alpha\beta}^3} f(\nu, \theta_\alpha, \theta_\beta), \tag{A.6}$$

where $\cos(\theta_\alpha) = \hat{\boldsymbol{n}}_\alpha \cdot \boldsymbol{r}_{\alpha\beta}$ and $\cos(\theta_\beta) = \hat{\boldsymbol{n}}_\beta \cdot \boldsymbol{r}_{\alpha\beta}$ are the orientations of cell α and cell β with respect to their separation vector, respectively. All relevant geometrical aspects of this interaction are realized and labeled in Fig. A.3. The dependence on these angles and the Poisson's ratio is collected in the function,

$$f(\nu,\theta_\alpha,\theta_\beta) = \frac{\nu(\nu+1)}{2\pi}\Big(3(\cos^2\theta_\alpha + \cos^2\theta_\beta - 5\cos^2\theta_\alpha\cos^2\theta_\beta - \tfrac{1}{3}) \\ - (2-\nu^{-1})\cos^2(\theta_\alpha-\theta_\beta) - 3(\nu^{-1}-4)\cos\theta_\alpha\cos\theta_\beta\cos(\theta_\alpha-\theta_\beta)\Big). \tag{A.7}$$

For simplicity, We will assume the magnitude of all contractile cell force dipoles in our system are equal, so $P_\alpha = P_\beta = P$, which is justified when considering a culture of identical cells.

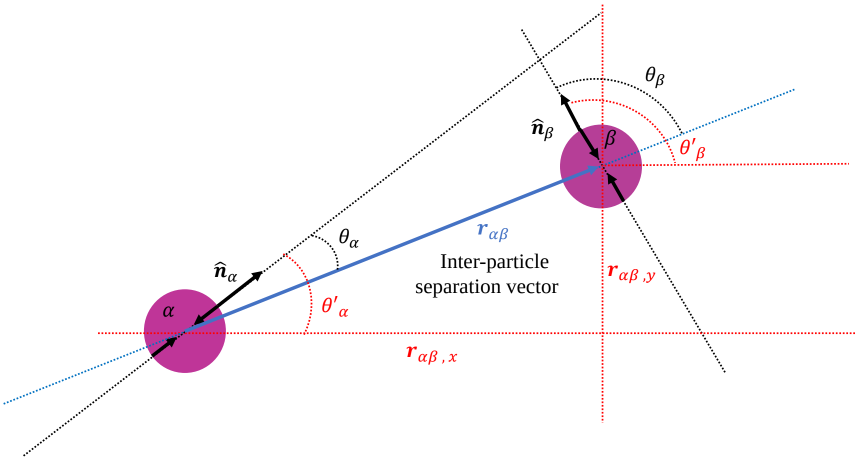

Supp. Fig. A.3: Schematic of two interacting particles with all relevant angles and vectors labeled. $\hat{\mathbf{n}}_i$ are unit vectors of force dipoles. θ'_i are angles of force dipoles with respect to the lab frame x-axis. θ_α and θ_β are angles of force dipoles with respect to their separation vector $\mathbf{r}_{\alpha\beta}$ which has components $\mathbf{r}_{\alpha\beta,x}$ and $\mathbf{r}_{\alpha\beta,y}$.

Taking derivatives of eqn. A.6 with respect to x_β and y_β to compute the x and y components of the force, respectively, on cell α from cell β yields

$$
\begin{aligned}
-\frac{dW_{\alpha\beta}}{dx_\alpha} = \frac{dW_{\alpha\beta}}{dx_\beta} &= \frac{\partial W_{\alpha\beta}}{\partial x_\beta} + \frac{\partial W_{\alpha\beta}}{\partial \theta_\alpha}\frac{\partial \theta_\alpha}{\partial x_\beta} + \frac{\partial W_{\alpha\beta}}{\partial \theta_\beta}\frac{\partial \theta_\beta}{\partial x_\beta} \\
&= -\frac{3P^2(1+\nu)}{16\pi E r_{\alpha\beta}^5}\Big(-2 + 2\nu + 6(\nu-1)(\cos 2\theta_\alpha + \cos 2\theta_\beta) \\
&+ (\nu-2)\cos 2(\theta_\alpha - \theta_\beta) - 15\nu \cos 2(\theta_\alpha + \theta_\beta)\Big) r_{\alpha\beta,x} \\
&- \frac{P^2(1+\nu)}{16\pi E r_{\alpha\beta}^5}\Big(12(\nu-1)(\sin 2\theta_\alpha + \sin 2\theta_\beta) - 60\nu \sin 2(\theta_\alpha + \theta_\beta)\Big) r_{\alpha\beta,y}
\end{aligned} \tag{A.8}
$$

and

$$
\begin{aligned}
-\frac{dW_{\alpha\beta}}{dy_\alpha} = \frac{dW_{\alpha\beta}}{dy_\beta} &= \frac{\partial W_{\alpha\beta}}{\partial y_\beta} + \frac{\partial W_{\alpha\beta}}{\partial \theta_\alpha}\frac{\partial \theta_\alpha}{\partial y_\beta} + \frac{\partial W_{\alpha\beta}}{\partial \theta_\beta}\frac{\partial \theta_\beta}{\partial y_\beta} \\
&= -\frac{3P^2(1+\nu)}{16\pi E r_{\alpha\beta}^5}\Big(-2 + 2\nu + 6(\nu-1)(\cos 2\theta_\alpha + \cos 2\theta_\beta) \\
&+ (\nu-2)\cos 2(\theta_\alpha - \theta_\beta) - 15\nu \cos 2(\theta_\alpha + \theta_\beta)\Big) r_{\alpha\beta,y} \\
&+ \frac{P^2(1+\nu)}{16\pi E r_{\alpha\beta}^5}\Big(12(\nu-1)(\sin 2\theta_\alpha + \sin 2\theta_\beta) - 60\nu \sin 2(\theta_\alpha + \theta_\beta)\Big) r_{\alpha\beta,x} \, ,
\end{aligned} \tag{A.9}
$$

where $r_{\alpha\beta,x} \equiv x_\beta - x_\alpha$ and $r_{\alpha\beta,y} \equiv y_\beta - y_\alpha$ are the x and y- components of the separation vector $\mathbf{r}_{\alpha\beta}$, respectively.

Similarly, for the torque on cell α by cell β, we take a derivative of the elastic potential with respect to θ_α

$$
\begin{aligned}
-\frac{\partial W_{\alpha\beta}}{\partial \theta_\alpha} = -\frac{P^2(1+\nu)}{8\pi E r_{\alpha\beta}^3}\Big(&-6(\nu-1)\sin 2\theta_\alpha \\
&- (\nu-2)\sin 2(\theta_\alpha - \theta_\beta) + 15\nu \sin 2(\theta_\alpha + \theta_\beta)\Big) \, .
\end{aligned} \tag{A.10}
$$

A.2 Phase portrait of simulation final snapshots on compressible and incompressible substrates

Fig. A.4b is shown in the main text. We now show the phase portrait for the low ν case in Supp. Fig. A.4a. While the trends and general dependence on A and N is the same for both values of Poisson's ratio, we can see from the $A = 10, N = 300$ cases that $\nu = 0.1$ forms longer chained, larger ringed structures than the $\nu = 0.5$ system which forms compact structures of tight rings and many junctions.

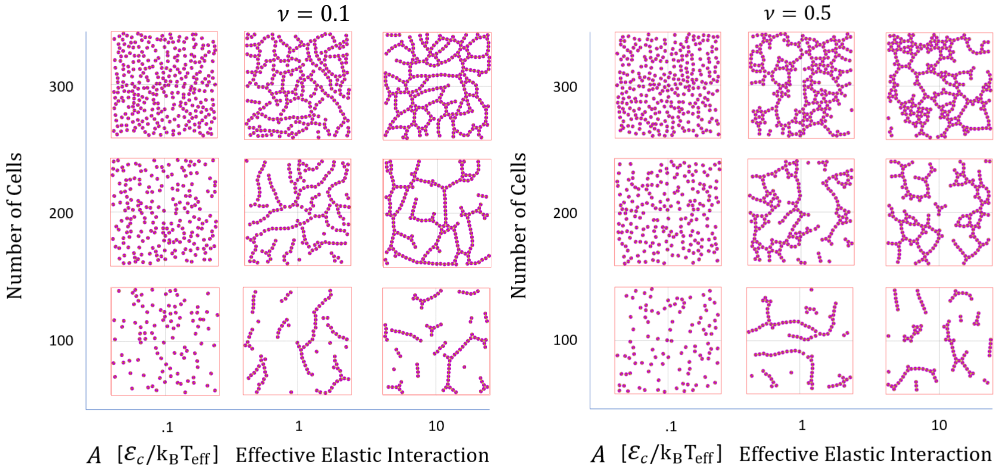

Supp. Fig. A.4: Simulation snapshots of final configurations in the parameter space of number of cells and $A \equiv \frac{\mathcal{E}_c}{k_\mathrm{B} T_\mathrm{eff}}$, the ratio of the characteristic elastic interaction strength and noise, for $\nu = 0.1$ (left) and $\nu = 0.5$ (right). At lower packing fractions, cells form segments of branches and stems. At lower A values, cells remain isolated. At higher values of A with sufficient packing fraction, cells form space spanning network configurations characterised by rings, branches, and junctions. At higher packing fractions, parallel chains occur frequently in these networks.

A.3 Computational analysis of networks

Identifying clusters

Each cell is assigned to a cluster by assigning an initial cell to zeroth cluster. Then the cells in its neighbor list - a list identifying all other cells that are within $1.2d$ of the central cell - are assigned to this cluster. The neighbor list of each of these neighbors is assigned this cluster label in an identical way. Once all neighbor lists have been exhausted, we search for unassigned cells and repeat the process with an incremented cluster number until every cell belongs to one or the other cluster. Once each cell belongs to a cluster, cell-cell distances are checked. If the distance between any two cells within the same cluster is greater than or equal to the size of the simulation box, we consider that realization of the network to be percolating. This calculation is done at the final time step of forty simulations per data point shown in Fig. 3 for dipoles and ten simulations per data point for diffusive sticky disks. The average value and corresponding error are then plotted as a function of packing fraction ϕ in Fig. 3a and of the effective elastic interaction parameter A in Fig. 3b.

Identifying junctions/branches

Final configurations of cells, like those shown in Figs. 1 and 2, are re-plotted with elongated black markers on cell positions along the direction of the dipole axis. This gives us networks like those shown in Supp. Fig. 11. These images are imported into imageJ [91], Gaussian blurred, intensity thresholded, binarized, and skeletonized. By then using the ”Analyze Skeleton” plugin in ImageJ, we obtain skeleton information including the full branch length distribution and junction counts [161].

Identifying rings

Instead of using the ”Analyze Skeleton” plugin in ImageJ, we invert the binarized image described above and utilize the ”Analyze Particles” function of ImageJ to obtain a distribution of rings and ring areas in the networks.

A.4 Critical packing fraction dependent on box size

In the main text, the connectivity percolation we report is for a specific box size $L = 26.66d$. This curve is subject to shift and/or dilate/contract under varying the box size (Supp. Fig. A.5). The box size we chose to use in the main text is appropriate (given our characteristic length scale of $\approx 50\mu m$ to compare to in vitro experiments of cells on compliant substrates.

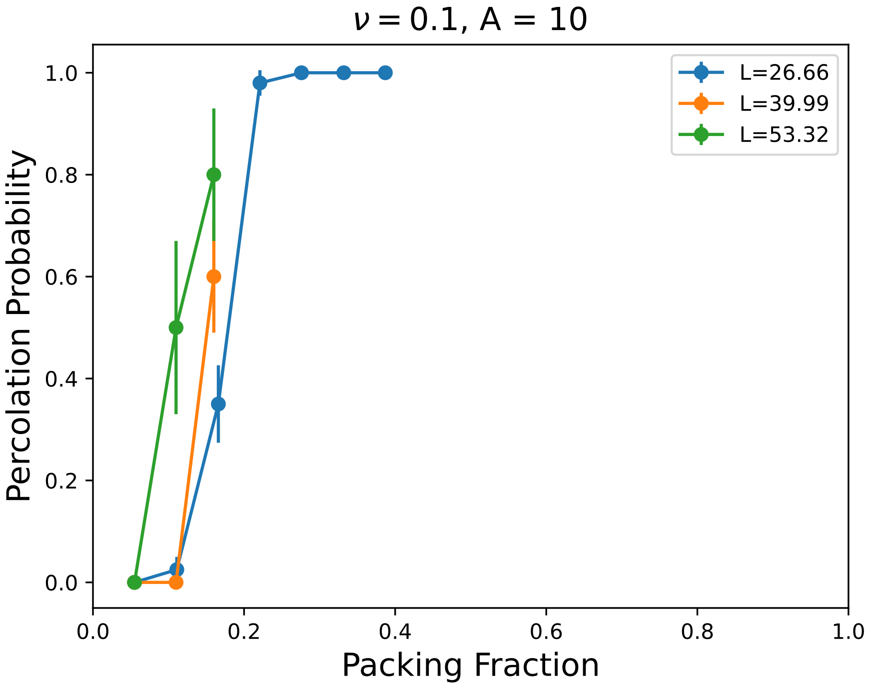

Supp. Fig. A.5: Critical packing fraction of elastic dipoles decreases with increasing box size. Due to the highly anisotropic nature of elastic dipolar interactions, dipoles will percolate at lower critical area fraction as (near the transition) area scales as L^2 whereas cluster size scales as L^{d_f} where d_f is the fractal dimension. Thus, the critical packing fraction will go as $L^{d_f - 2}$ where $d_f - 2 < 0$.

A.5 Mapping the effective interaction parameter to substrate stiffness

We have considered the effective elastic interaction, A, to be the model parameter which encodes stochasticity, cell forces, and substrate stiffness. We wish now to relate this parameter to an easily accessible and measurable experimental value - substrate stiffness. By casting A in terms of substrate stiffness, we aim to predict trends with varying substrate stiffness, which can be directly tested in experiment. It is known from traction force experiments (such as Ref. [87]) that cells on elastic substrates adapt their forces to substrate stiffness. Adherent cells on softer substrates build fewer and smaller focal adhesions. With increasing substrate stiffness, cells spread more and exert stronger traction forces which saturate to a constant value beyond a typical substrate stiffness E^*

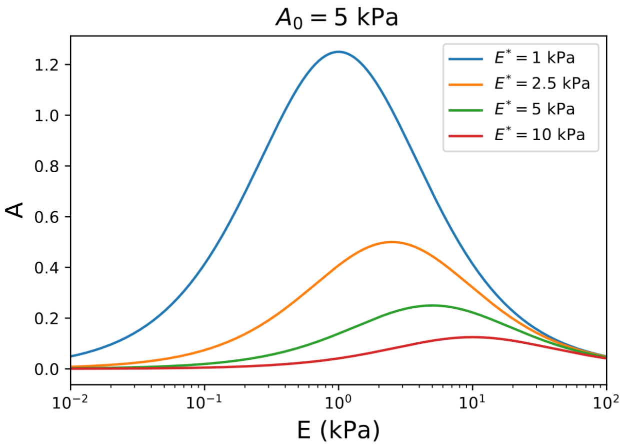

Supp. Fig. A.6: Mapping A to E. Four curves characterized by various choices of optimal substrate stiffness E^* for A_0 are shown. Range of A values mapped to E decreases as the choice of optimal stiffness increases.

which depends on cell type (table A.1). This mechanical adaptivity of the cell traction

Table A.1: Contractility and optimal stiffness of various cell types.

P_0 **(J)**	E^* **(kPa)**	**Cell Type**
10^{-12}[53][58]	1-10[62, 61]	Endothelial
10^{-13}[162]	0.1[163, 164]	Neuron
10^{-9}[165]	20[163]	Smooth Muscle
10^{-11} [166]	10 [166]	Astrocyte

is modeled by considering a force dipole magnitude that scales with substrate stiffness as [54],

$$P(E) = P_0E/(E + E^*). \tag{A.11}$$

Plugging in A.11 to our definition of A gives us $A = \frac{P^2}{16Ed^3k_\mathrm{B}T_\mathrm{eff}} = \frac{P_0^2E}{16(E+E^*)^2d^3k_\mathrm{B}T_\mathrm{eff}}$, which has a non-monotonic dependence on substrate stiffness, as seen in Supp. Fig. A.6, reaching a maximum of $\frac{A_0}{4}$ where $A_0 \equiv \frac{P_0^2}{16d^3k_\mathrm{B}T_\mathrm{eff}}$ at $E = E^*$. We now have a mapping from effective interaction parameter A to substrate stiffness E which we can directly relate to experiments.

We know from experiments of endothelial cells on elastic substrates, that cells can form networks or remain isolated from one another depending on the substrate rigidity

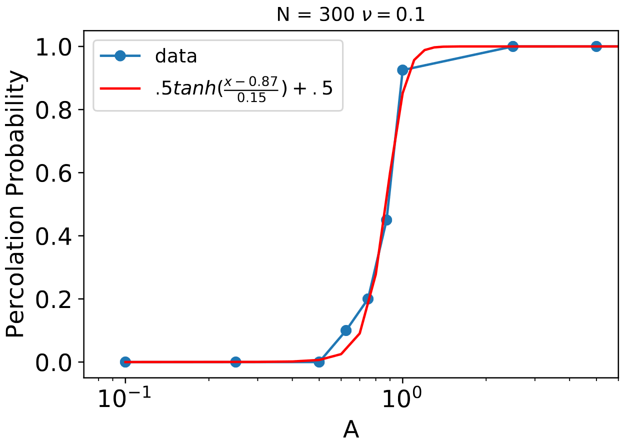

Supp. Fig. A.7: Percolation probability as a function of effective elastic interaction for $N = 300(\phi \approx .33)$ cells where $\nu = 0.1$. The percolation curve is fit well to a hyperbolic tangent function with two free parameters corresponding to the position and width of the transition.

[62]. This is to say that there is a range of viable substrate stiffnesses over which cells will self-assemble into vascular networks. We now ask if we can predict the viable range of stiffnesses that accommodate network formation. We use the metric of percolation probability to quantify the tendency for network formation. We know that we can make these predictions numerically as we now have a mapping from A to E for our simulations. Percolation vs. substrate stiffness curves are shown in Supp. Fig. A.8b for various values of $A_0 \equiv \frac{P_0^2}{16k_\mathrm{B}T_\mathrm{eff}d^3}$, the effective elastic interaction without stiffness dependence.

We now seek to develop an analytic treatment of the substrate dependent percolation metric and obtain a closed form expression which predicts the range of substrate stiffnesses conducive to network formation. Supp. Fig. A.7 shows that percolation vs. A is well fit by a hyperbolic tangent function with two fit parameters A^* and k such that

$$p = .5\tanh\left(\frac{A - A^*}{k}\right) + .5, \qquad \text{(A.12)}$$

where p is the percolation probability. We will use the full width at half maximum (FWHM) to represent the range of values over which networks are formed. In order to find the FWHM, which we will call Σ, of the above function, we set p equal to half of its maximum value, which we assume is 1. This gives us the condition $A = A^*$, which

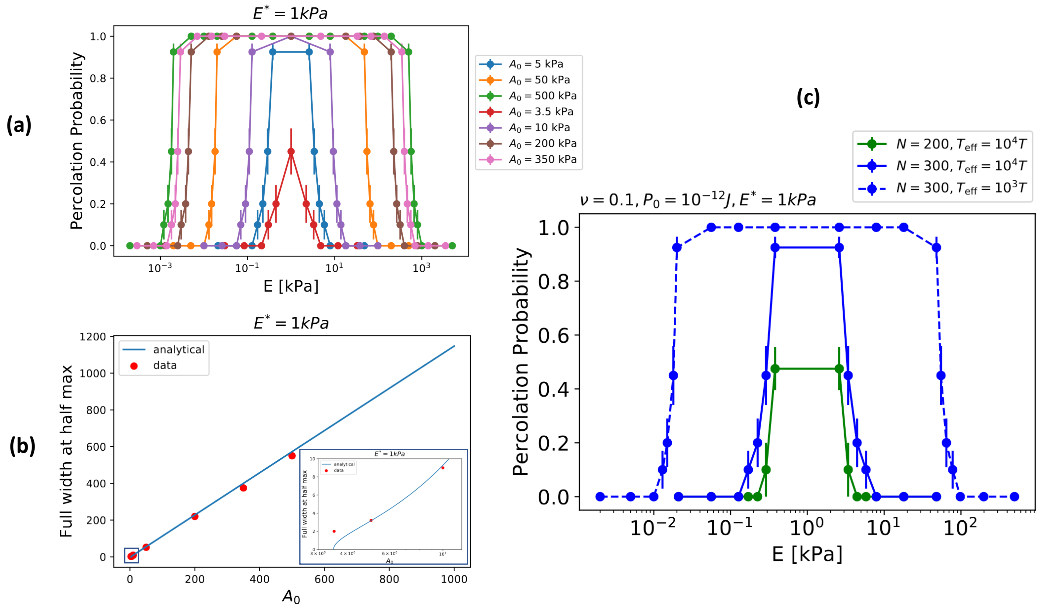

Supp. Fig. A.8: Percolation peak width as a function of A_0. (a) Percolation probability as a function of substrate stiffness for various values of A_0. (b) Blue curve shows the analytic expression for percolation peak width quadratic in A_0 gives good agreement with mappings from simulation data, shown in red dots obtained from (a), except at lower values of A_0 where the analytical expression breaks down due to an assumption of transition ($p_{max} \approx 1$). (c) Percolation probability as a function of elastic substrate stiffness where the optimal stiffness is assumed to be 1 kPa. Percolation peak is centered on critical stiffness and has a width dependent on both packing fraction and effective temperature.

we can rewrite in the following way

$$E^2 + \left(2E^* - \frac{A_0}{A^*}\right)E + E^{*2} = 0. \tag{A.13}$$

Thus, we obtain an expression for the FWHM of our percolation curves given by

$$\Sigma = \sqrt{\left(\frac{A_0}{A^*} - 2E^*\right)^2 - 4E^{*2}}. \tag{A.14}$$

Supp. Fig. A.8a shows a comparison of peak width for various values of A_0 computed with A.14 and computed numerically from Supp. Fig. A.8b. The plot shows great agreement between the analytical prediction and numerical results except at values of A_0 that are close to the analytical solution condition $\frac{P_0^2}{16d^3 k_{\rm B} T_{\rm eff} A^*} \geq 4E^*$. This disparity, shown in the inset of Supp. Fig. A.8a is due to the assumption that the maximum percolation value is 1, which is not the case for the red curve in Supp. Fig. A.8b.

Thus, A.14 provides us a closed form expression, valid over a large interval of parameter space, for the range of substrate stiffnesses over which cells will form percolating networks. This value is dependent on cell forces, effective temperature, cell size, and a fit parameter A^* which represents the position of the percolation transition. In particular, it predicts that higher force dipole magnitude (P_0), lower noise (T_{eff}), and higher cell density corresponding to lower required elastic interaction for percolation (A^*), all lead to wider peaks in percolation vs substrate stiffness.

A.6 Order Parameter Thresholds informed by largest cluster and spatial extent

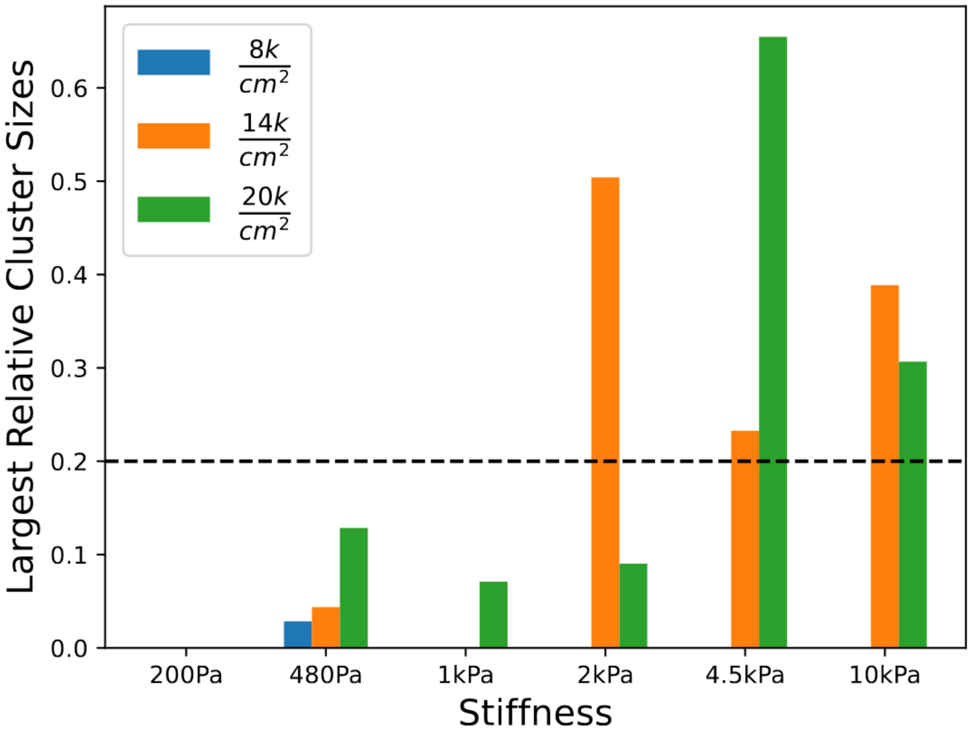

Supp. Fig. A.9: Largest relative cluster group size. Values are the sum of the largest clusters contributions as determined by the DBSCAN algorithm with tolerance .01, corresponding to a one percent difference in relative cluster size. Only those whose largest cluster group contributes at least twenty percent the total cell area are classified as percolating structures.

In the main text, we classify experimental systems into percolating “networks” if the average percolation is greater than $p_T = 0.7$; into elongated ”chains” if the percolation is below p_T and shape factor above $s_T = 0.95$; and isotropic ”isolated” clusters if percolation is below p_T and shape factor is below s_T. Supp. Fig. A.9 shows that the percolation threshold value corresponds to the largest cluster group (as determined by a density-based spatial clustering algorithm with a max distance set to one percent [167]) account for more than twenty percent of total cell area. The shape factor threshold is chosen as it is greater than two simulation cells in a line - the elongated morphology we want to characterize with this metric.

A.7 Dependence of percolation on packing fraction and elastic interactions

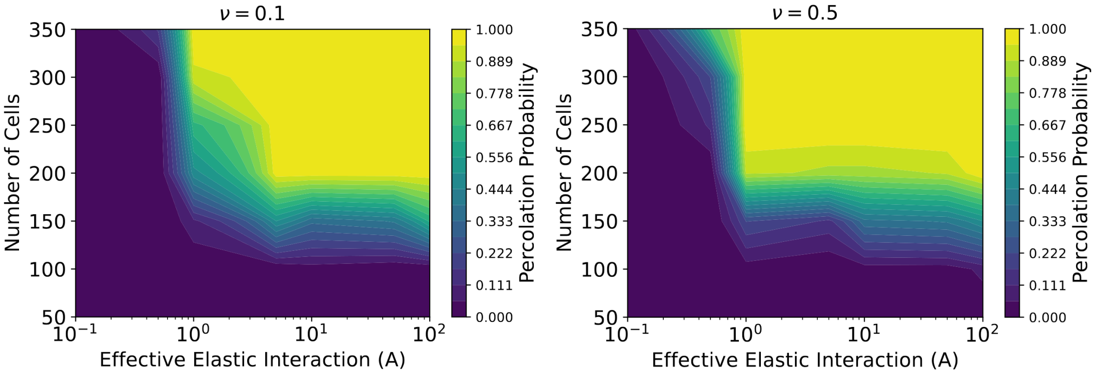

Supp. Fig. A.10: Percolation contour plots show $\nu = 0.1$ is more efficient with respect to N while $\nu = 0.5$ is more efficient with respect to A. (a) Color represents percolation probability in (A,N) space for $\nu = 0.1$ (left) and $\nu = 0.5$ (right). For $A < 5$, $\nu = 0.5$ is more percolating while for $A \geq 5$, $\nu = 0.1$ is more percolating.

While we report several percolation curves in Fig.3 of the main text, Supp. Fig. A.10 shows a percolation contour map in (A,N) space. At low A, $\nu = 0.5$ percolates more reliably than the low ν counterpart as the system is more resilient to noise. At $A \geq 5$, however, $\nu = 0.1$ percolates more reliably with fewer cells as we have seen the lower ν

system forms more extended structures in general. The full percolation map then shows that networks at low Poisson's ratio are more efficient with respect to number of cells, whereas the high Poisson's ratio networks are more efficient with respect to effective elastic interaction.

A.8 Irrigation area reveals a marginal efficiency for networks at low Poisson's ratio

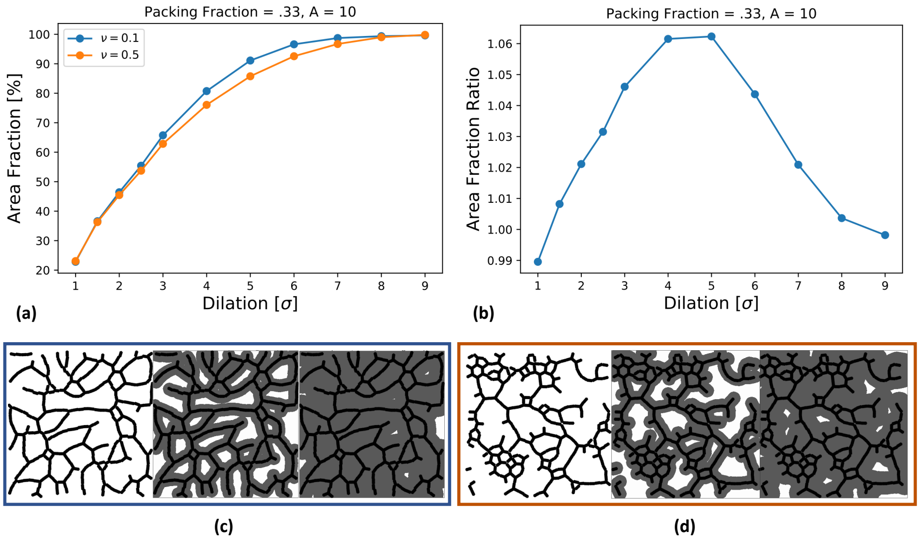

Supp. Fig. A.11: Substrate compressibility alters area coverage of networks. (a) Fraction of available area covered by simulated networks at $A = 10$ and $\phi = .33 (N = 300)$, as the cell area is uniformly inflated by a dilation factor . $\nu = 0.1$ exhibits greater area for given dilation than the $\nu = 0.5$ case. This is due to the fact that higher values of ν produce networks with more compact structures like junctions and 4-rings. These structures overlap with one another when inflated unlike sparse networks with long branches. (b) Ratio of area coverage of $\nu = 0.1$ to $\nu = 0.5$ for $A = 10$ and $\phi = .33 (N = 300)$. The plot increases sharply past unity then saturates to one at area limited dilation. (c) Visualizations of homogeneous dilation of a representative $\nu = 0.1$ network. (d) Visualizations of homogeneous dilation of a representative $\nu = 0.5$ network.

The ability of a biological network to efficiently cover space is crucial to deliver signals and materials. Assuming the drainage area of each cell to be a dilation factor times the cell size, we analyze how the filling area of our networks scale with this cell dilation. We can then determine the density of interconnections within our networks. Supp. Fig. A.11 shows the filled area fraction of our networks as a function of homogeneous dilation factors. Realizations of these dilated networks at different dilation factors are shown as shaded regions in part c and d. This plot shows that the lower ν case increases area coverage as a function of dilation faster than the higher ν case. This reinforces the result in Fig. 6e as area fraction growth rate is maximized when cell overlap and proximity is minimized. Since higher values of Poisson's ratio produce networks with more compact structures of higher neighbor counts, its area coverage does not scale with dilation as strongly as the lower ν case.

A.9 Model network morphological features depend on substrate compressibility given by Poisson's ratio

While percolation is by nature a global quantity describing the whole network, we now employ more local metrics to classify the topology of our networks. Figs. A.12a-d show characteristic networks of $N = 300$ ($\phi = 0.33$) cells for $\nu = 0.1$ (top) and $\nu = 0.5$ (bottom) when the system is well past the percolation transition ($A = 10$, right), and at the shoulder of the transition ($A \leq 1$, left). The particles in these snapshots have been given artificially elongated bodies along their dipole axis to emphasize the backbone of the network and aid the image analysis process, detailed in SI section A.3. The relative number of the different topological features of these networks, e.g. open ends, junctions, and rings, will determine the average number of neighbors (or coordination number, z) of each cell dipole.

Fig. A.12e shows that the average number of neighbors increases with effective elastic interaction A (for $N = 300$ fixed) and cell number density (for $A = 10$ fixed), for both $\nu = 0.1$ and $\nu = 0.5$ that saturates in A. This quantity is calculated for the final simulation configuration of three networks per value of Poisson's ratio. The saturating neighbor count for each Poisson's ratio is reached for percolating networks and corresponds to the disparate topological features characteristic of these two cases. The higher $\nu = 0.5$ (incompressible) substrate case shows a higher saturating neighbor ($z > 3$), which indicates the preeminent structures inherent to this network are junctions

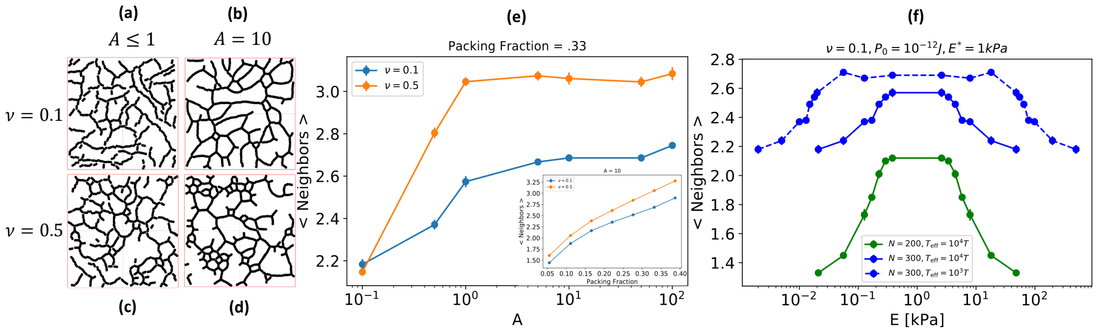

Supp. Fig. A.12: Neighbor counts reveal relative prevalence of various morphological structures in networks formed by elastic dipolar interactions.(a)-(d) Simulation snapshots of cell assemblies at the shoulder of the percolation transition (left) and well above the percolation transition (right).(e) Number of neighbors as a function of A when $\phi = .33 (N = 300)$ for $\nu = 0.1$ - blue - and $\nu = 0.5$ - orange where a neighbor in this context is defined as a cell α whose center is within one and a half cell diameters away from cell β ($|r_{\alpha\beta}| \leq 1.5d$). While the number of neighbors is relatively insensitive to A, there is a marked difference between the two values of Poisson's ratio. Across A space, cells on substrates of higher ν values accumulate more neighbors than the lower ν cases. Inset shows number of neighbors as a function of packing fraction for $A = 10$. Cells on higher ν value substrates have more neighbors than the low ν case regardless of packing fraction. (f) Number of neighbors as a function of substrate stiffness. Optimal stiffness is assumed to be 1 kPa. $N = 200 (\phi \approx .22)$ exhibits an average neighbor count of 1-2 indicating the prominence of short chains. $N = 300 (\phi \approx .33)$ case shows average neighbor counts of 2-3 indicating an abundance of chains, rings, and junctions. The peak in neighbor count over stiffness is taller and wider for lower effective temperature and higher cell density. Each data point and error bar represents the average and standard error of the mean, respectively, of ten simulations.

and tighter rings (with up to 4 neighbors), consistent with the characteristic simulation snapshots in Fig. A.12d. The saturating neighbor count for low $\nu = 0.1$ (more compressible) substrates is lower ($2 < z < 3$. This suggests that these networks exhibit long chains as well as more interconnected structures like junctions and rings, consistent with the characteristic simulation snapshots shown in Fig. A.12b. This trend is seen over a wide range of packing fractions as shown by the inset in Fig. A.12e. The qualitative differences between the two types of networks ultimately arise from the different orientational dependencies of the deformation induced by a dipole, as shown in Fig. 1e, with a transition expected at $\nu = 0.3$ [53]. We note that these results are for a relatively dilute regime ($\phi = 0.33$), whereas in the limit of complete packing, neighbor count would saturate to a maximum possible value of 6.

Interestingly, the networks on the lower Poisson ratio substrates exhibit a saturating neighbor count ($z \simeq 2.6$), that is very close to that for the predicted rigidity percolation threshold for elastic fiber networks ($z_c = 2.67$) [75, 76]. This may be attributed to the self-assembled linear chains that mimic semiflexible polymers [168], with bending rigidity of a "polymer" of disks, set by the dipolar interaction strength, A. This implies that although we do not measure the rigidity of networks in simulation, the connectivity percolation is closely related to it and predicts the onset of rigidity percolation threshold as well. Such a transition from isolated, fluid-like, motile cells to a mechanically rigid state has been shown to be biologically important for epithelial cells during development and disease [77], and may also be relevant to network-forming endothelial cells.

Similarly to percolation, Fig. A.12f shows that neighbor counts exhibit peaks over intervals of substrate stiffness centered around the characteristic substrate stiffness (chosen to be $E^* = 1$ kPa) and can be narrowed and decreased by increasing effective temperature and decreasing packing fraction. This result is consistent with Fig. 1 where cells on substrates that are too soft or too stiff remain isolated and have fewer neighbors than those in network configurations that form at the optimal stiffness range.

A.10 Simulation results for different choices of translational and rotational diffusivity

While the results we present in the main text are for systems in which we choose the rotational and translational diffusivity to be proportional ($d^2 D_R = D_T$), this is not required to be the case for cells. The random movements of cells are caused by their internal physico-chemical activity, and the diffusivities are therefore not constrained by the fluctuation-dissipation theorem. Supp. Fig. A.13 shows that both $\nu = 0.1$(top) and $\nu = 0.5$(bottom) systems give rise to similar network configurations, whether the rotational diffusion is half or double its translational counterpart. This suggests that a different choice of rotational and translational diffusivity does not change the tendency of dipoles to form networks.

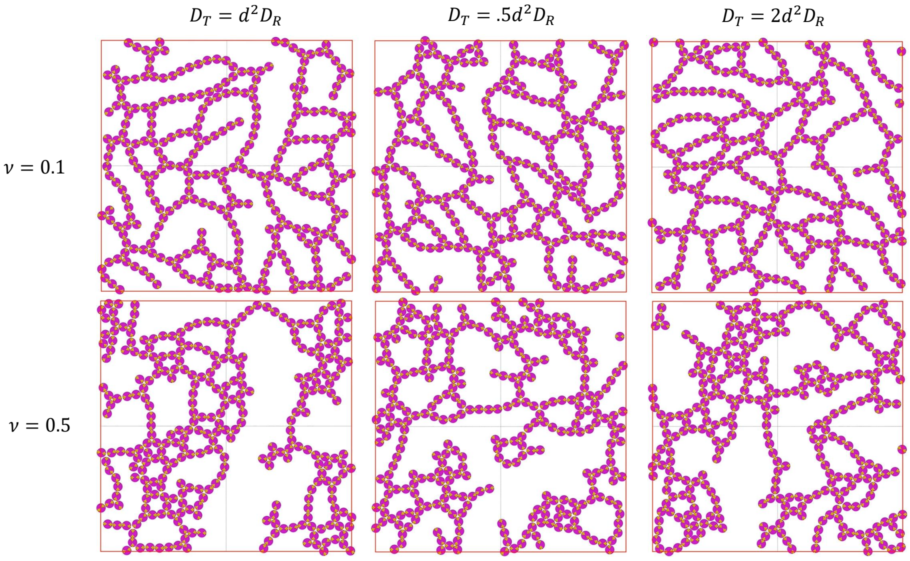

Supp. Fig. A.13: Network formation tendency robust to differing diffusion coefficients. (left) Networks formed from assumption stated in main text ($D_T = d^2 D_R$). (middle) Networks form when $D_T = .5d^2 D_R$. (right) Networks form when $D_T = 2d^2 D_R$.

A.11 Nondimensionalization of Langevin equations

We begin with the Langevin equation for cell position stated on the first line of the Model section of the main text.

$$\frac{d\mathbf{r}_\alpha}{dt} = -\mu_T \sum_\beta \frac{\partial W_{\alpha\beta}}{\partial \mathbf{r}_\alpha} + \sqrt{2D_\mathrm{T}}\ \boldsymbol{\eta}_{\alpha,\mathrm{T}}(t)\ , \tag{A.15}$$

where D_T is the effective translational diffusivity quantifying the random motion of an isolated moving cell, with $\boldsymbol{\eta}$ as a random white noise term whose components satisfy $\langle \eta_i(t)\eta_j(t')\rangle = \delta(t-t')\delta_{ij}$. Note that η - the noise term describing active cell motility - has units of $t^{-1/2}$. $W_{\alpha\beta}$ is a long-range elastic potential (full form shown in kdwrite equation number) when $d \leq \mathrm{r}_{\alpha\beta} \leq 3d$ and a steric spring given by $W_{\alpha\beta} = \frac{1}{2}k(d - r_{\alpha\beta})^2$ when $0 < \mathrm{r}_{\alpha\beta} \leq d$.

We now choose characteristic time, length, and energy scales. Let $\mathbf{r}^* = \frac{\mathbf{r}}{d}$ be a dimensionless distance vector scaled by cell size, let $W^*_{\alpha\beta} = \left(\frac{P^2}{16Ed^3}\right)^{-1} W_{\alpha\beta}$ be a dimensionless energy scaled by elastic energy at cell length separation, and let $t^* = \frac{P^2\mu_\mathrm{T}}{16Ed^5}t$ be a dimensionless time scaled by an elastic interaction.

Non-dimensionalizing our translational Langevin equation using the above characteristic scales gives us the following equation

$$\frac{d\mathbf{r}_\alpha^*}{dt^*} = -\sum_\beta \frac{\partial W_{\alpha\beta}^*}{\partial \mathbf{r}_\alpha^*} + \sqrt{\frac{2}{A}}\ \boldsymbol{\eta}_{\alpha,\mathrm{T}}^*(t^*)\ , \tag{A.16}$$

where

$$A \equiv \frac{P^2\mu_\mathrm{T}}{16Ed^3D_\mathrm{T}} = \frac{P^2}{16Ed^3k_\mathrm{B}T_\mathrm{eff}} = \frac{\mathcal{E}_c}{k_\mathrm{B}T_\mathrm{eff}} \tag{A.17}$$

is a dimensionless parameter that is the ratio of characteristic elastic energy to an effective temperature called the effective elastic interaction.

The Langevin equation for cell orientation is given by

$$\frac{d\hat{\mathbf{n}}_\alpha}{dt} = -\mu_R \sum_\beta \left(\hat{\mathbf{n}}_\alpha \times \frac{\partial W_{\alpha\beta}}{\partial \hat{\mathbf{n}}_\alpha}\right) + \sqrt{2D_\mathrm{R}}\ \boldsymbol{\eta}_{\alpha,\mathrm{R}}(t) \tag{A.18}$$

where $\hat{\boldsymbol{n}}$ is the cell orientation and D_R is the effective rotational diffusivity quantifying the random reorientations of an isolated moving cell.

Nondimensionalizing eqn. A.18 with the same scales as in the translational Langevin equation and assuming $\mu_\mathrm{R}d^2 = \mu_\mathrm{T}$ and $D_\mathrm{R}d^2 = D_\mathrm{T}$ gives us

$$\frac{d\hat{\mathbf{n}}_\alpha}{dt^*} = -\sum_\beta \left(\hat{\mathbf{n}}_\alpha \times \frac{\partial W_{\alpha\beta}^*}{\partial \hat{\mathbf{n}}_\alpha}\right) + \sqrt{\frac{2}{A}}\ \boldsymbol{\eta}_{\alpha,\mathrm{R}}^*(t^*)\ . \tag{A.19}$$

A.12 Junction count shows similar behavior to neighbor counts

Another metric that can be used to probe the morphologies of our branched networks is junction density - the number of cells connected to a node after skeletonizing normalized by the total number of cells. Junction density is shown in Supp. Fig. A.14 as a function of A (left) and ϕ (or N) (right). Unsurprisingly, junction density vs. A follows the same trend as neighbors vs. A shown in Supp. Fig. A.12 since junctions are structures which promote higher neighbor counts. In contrast with neighbors vs. ϕ, our highest value of packing for junction density exhibits a different trend. While neighbor counts continue to increase, junction density slightly decreases for $\nu = 0.1$. This is due to the ground states explored in the previous section. At our highest packing fraction,

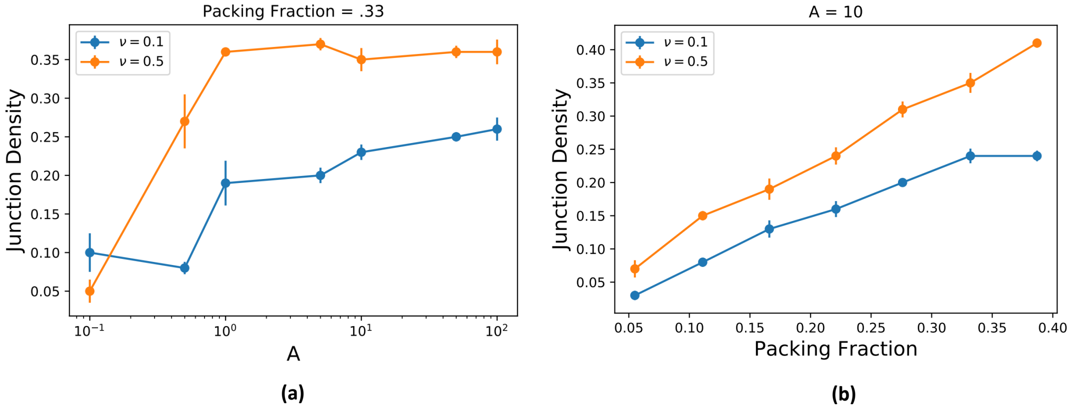

Supp. Fig. A.14: Junction density shows a trend similar to neighbor counts. (a) Junction density vs. A shows at low A, few cells are part of a junction. As A increases, irreversible networks structures are formed where the $\nu = 0.5$ systems exhibit a greater capacity to form junctions - structures which produce greater neighbor counts. (b) Junction density vs. ϕ (or N) increases as a function for all N when $\nu = 0.5$. Junction density begins to decrease at highest ϕ as the system begins to form more parallel strings in the low ν case.

we begin to transition out of the dilute regime where we know $\nu = 0.1$ dipoles will form parallel strings. Tightly packed parallel strings will have a high neighbor count but no junctions.

A.13 Experimental branch lengths

One of the metrics we have used to characterize the morphology of our simulated dipole assemblies is branch length. While it is difficult to directly compare simulation to experiment with branch lengths due to there not being a common length scale, we report the branch lengths for two different seeding densities and post seeding times (Fig. A.15). The branch lengths show a saturation in substrate stiffness.

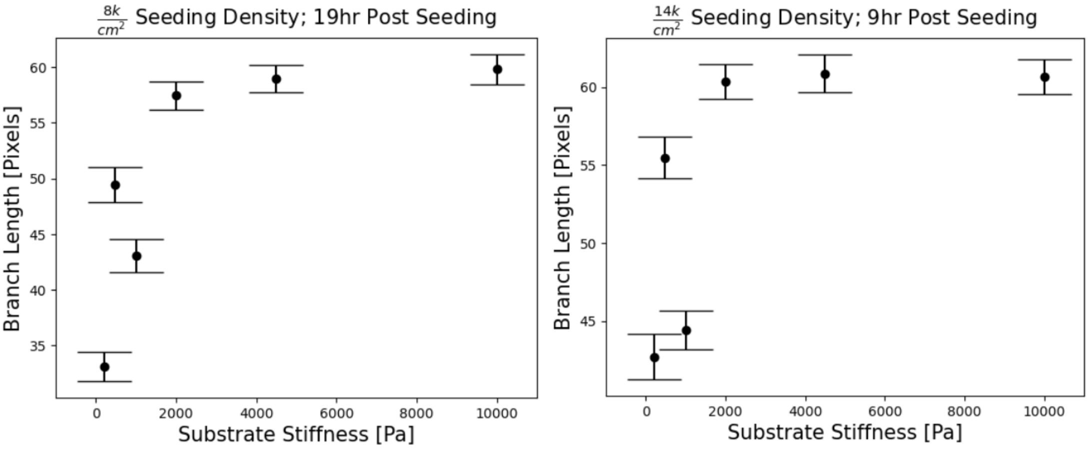

Supp. Fig. A.15: Average branch lengths of experimental systems at both low and high seeding density show a saturation in substrate stiffness.

A.14 Branch length analysis of simulation box and a larger composite box shows boundary errors are minimal

We utilize skeletonization in ImageJ for branch length, junction count, ring count, and robustness. ImageJ, however, does not account for the periodic boundary conditions by which cells interact. These boundary errors could lead to an incorrect analysis for the aforementioned metrics. To study the effect of these boundary errors, we report the branch length histograms and average branch lengths for both the original simulation box results and a box comprised of a 3x3 replication of the original simulation box in order to reconstitute periodicity and minimize boundary errors. Supp. Fig. A.16 shows that the errors due to the boundary effects are minimal which lets us use the original box size for a computationally easier analysis.

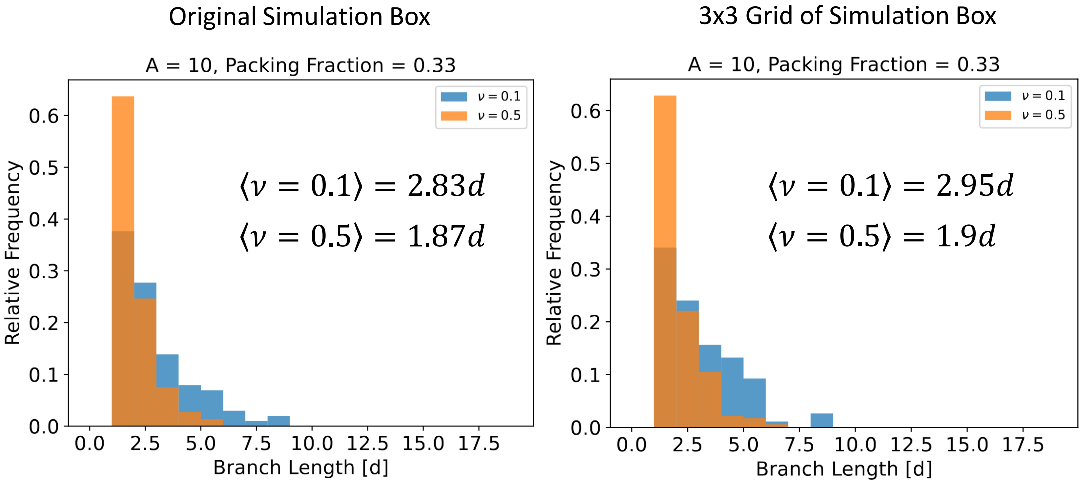

Supp. Fig. A.16: Branch length distributions for both the original simulation box and a composite box reveal minimal boundary effects. (a) Branch length distribution for $A = 10$ and $N = 300$ with average branch length for our original simulation box. (b) Branch length distribution for $A = 10$ and $N = 300$ with average branch length when the original simulation box is made into an identical 3x3 grid of the simulation snapshots to reconstitute periodicity and study the effect of this boundary effect. Histograms are qualitatively similar and the error for the average branch lengths for both $\nu = 0.1$ and $\nu = 0.5$ is less than 5%. Thus, for computational feasibility of robustness studied in Fig.7d, we use the original simulation box snapshots.

Appendix B

Code Availability

The code for simulating dipole networks, dipoles in spring meshes, and motile dipoles under confinement found in the methods section of chapter 2, the model and results section of chapter 3, and the methods section of chapter 4, respectively, can be found at the following github repository.

Bibliography

[1] TJ Mitchison and LP Cramer. Actin-based cell motility and cell locomotion. Cell, 84(3):371–379, 1996.

[2] Vivek K Gupta and Ovijit Chaudhuri. Mechanical regulation of cell-cycle progression and division. Trends in cell biology, 32(9):773–785, 2022.

[3] Yuta Shimamoto, Stefanie Redemann, and Daniel Needleman. Mechanics of cell division, 2020.

[4] Caroline Uhler and GV Shivashankar. Regulation of genome organization and gene expression by nuclear mechanotransduction. Nature reviews Molecular cell biology, 18(12):717–727, 2017.

[5] Adam J. Engler, Shamik Sen, H. Lee Sweeney, and Dennis E. Discher. Matrix elasticity directs stem cell lineage specification. Cell, 126(4):677–689, 2006.

[6] Sriram Ramaswamy. Active matter. Journal of Statistical Mechanics: Theory and Experiment, 2017(5):054002, 2017.

[7] Pawel Romanczuk, Markus Bär, Werner Ebeling, Benjamin Lindner, and Lutz Schimansky-Geier. Active brownian particles. The European Physical Journal Special Topics, 202(1):1–162, 2012.

[8] Alexandre P Solon, Michael E Cates, and Julien Tailleur. Active brownian particles and run-and-tumble particles: A comparative study. The European Physical Journal Special Topics, 224(7):1231–1262, 2015.

[9] David Martin, Jérémy O'Byrne, Michael E Cates, Étienne Fodor, Cesare Nardini, Julien Tailleur, and Frédéric Van Wijland. Statistical mechanics of active ornstein-uhlenbeck particles. Physical Review E, 103(3):032607, 2021.

[10] Michael E. Cates and Julien Tailleur. Motility-induced phase separation. Annual Review of Condensed Matter Physics, 6(1):219–244, 2015.

[11] Robert J. Pelham and Yu-li Wang. Cell locomotion and focal adhesions are regulated by substrate flexibility. Proceedings of the National Academy of Sciences, 94(25):13661–13665, 1997.

[12] Micah Dembo and Yu-Li Wang. Stresses at the cell-to-substrate interface during locomotion of fibroblasts. Biophysical Journal, 76(4):2307 – 2316, 1999.

[13] Nathalie Q. Balaban, Ulrich S. Schwarz, Daniel Riveline, Polina Goichberg, Gila Tzur, Ilana Sabanay, Diana Mahalu, Sam Safran, Alexander Bershadsky, Lia Addadi, and Benjamin Geiger. Force and focal adhesion assembly: a close relationship studied using elastic micropatterned substrates. Nature Cell Biology, 3:466, Apr 2001. Article.

[14] Michael Murrell, Patrick W. Oakes, Martin Lenz, and Margaret L. Gardel. Forcing cells into shape: the mechanics of actomyosin contractility. Nature Reviews Molecular Cell Biology, 16:486, Jul 2015. Review Article.

[15] Cynthia A. Reinhart-King, Micah Dembo, and Daniel A. Hammer. Cell-cell mechanical communication through compliant substrates. Biophysical Journal, 95(12):6044 – 6051, 2008.

[16] Xin Tang, Piyush Bajaj, Rashid Bashir, and Taher A. Saif. How far cardiac cells can see each other mechanically. Soft Matter, 7:6151–6158, 2011.

[17] Ido Nitsan, Stavit Drori, Yair E Lewis, Shlomi Cohen, and Shelly Tzlil. Mechanical communication in cardiac cell synchronized beating. Nature Physics, 12(5):472–477, 2016.

[18] Jacob Notbohm, Ayelet Lesman, Phoebus Rosakis, David A Tirrell, and Guruswami Ravichandran. Microbuckling of fibrin provides a mechanism for cell mechanosensing. Journal of The Royal Society Interface, 12(108):20150320, 2015.

[19] A.S. Abhilash, Brendon M. Baker, Britta Trappmann, Christopher S. Chen, and Vivek B. Shenoy. Remodeling of fibrous extracellular matrices by contractile cells: Predictions from discrete fiber network simulations. Biophysical Journal, 107(8):1829 – 1840, 2014.

[20] RFM van Oers, EG Rens, DJ LaValley, CA Reinhart-King, and RMH Merks. Mechanical cell-matrix feedback explains pairwise and collective endothelial cell behavior in vitro. PLoS Comput Biol, 10(8):e1003774, 2014.

[21] K. Dasbiswas, S. Majkut, D. E. Discher, and S. A. Safran. Substrate stiffness-modulated registry phase correlations in cardiomyocytes map structural order to coherent beating. Nature Communications, 6:6085, 2015.

[22] Ohad Cohen and Samuel A Safran. Elastic interactions synchronize beating in cardiomyocytes. Soft matter, 12(28):6088–6095, 2016.

[23] Cynthia A. Reinhart-King, Micah Dembo, and Daniel A. Hammer. Endothelial cell traction forces on rgd-derivatized polyacrylamide substrata. Langmuir, 19(5):1573–1579, Mar 2003.

[24] Benoit Palmieri, Christine Scanlon, Daniel Worroll III, Martin Grant, and Juliet Lee. Substrate mediated interaction between pairs of keratocytes: Multipole traction force models describe their migratory behavior. Plos one, 14(3):e0212162, 2019.

[25] Matthew R Hannaford and Nasser M Rusan. Positioning centrioles and centrosomes. Journal of Cell Biology, 223(4), 2024.

[26] Elizabeth Granger, Gavin McNee, Victoria Allan, and Philip Woodman. The role of the cytoskeleton and molecular motors in endosomal dynamics. In Seminars in cell & developmental biology, volume 31, pages 20–29. Elsevier, 2014.

[27] Joshua J Park and Y Peng Loh. Minireview: How peptide hormone vesicles are transported to the secretion site for exocytosis. Molecular endocrinology, 22(12):2583–2595, 2008.

[28] Pedro Guedes-Dias and Erika LF Holzbaur. Axonal transport: Driving synaptic function. Science, 366(6462):eaaw9997, 2019.

[29] L. D. Landau and E. M. Lifshitz. Theory of Elasticity, volume 7 of Course of Theoretical Physics. Pergamon Press, London, 1959.

[30] Xiaonan Hou and Vadim V Silberschmidt. Metamaterials with negative poisson's ratio: A review of mechanical properties and deformation mechanisms. Mechanics of Advanced Materials: Analysis of Properties and Performance, pages 155–179, 2015.

[31] I. B. Bischofs, S. A. Safran, and U. S. Schwarz. Elastic interactions of active cells with soft materials. Phys Rev E Stat Nonlin Soft Matter Phys, 69(2 Pt 1):021911, Feb 2004.

[32] Patrick S Noerr, Jose E Zamora Alvarado, Farnaz Golnaraghi, Kara E McCloskey, Ajay Gopinathan, and Kinjal Dasbiswas. Optimal mechanical interactions direct multicellular network formation on elastic substrates. Proceedings of the National Academy of Sciences, 120(45):e2301555120, 2023.

[33] Gabor Forgacs and Stuart A Newman. Biological physics of the developing embryo. Cambridge University Press, 2005.

[34] Ramsey A Foty and Malcolm S Steinberg. The differential adhesion hypothesis: a direct evaluation. Developmental biology, 278(1):255–263, 2005.

[35] D. Manoussaki, S. R. Lubkin, R. B. Vemon, and J. D. Murray. A mechanical model for the formation of vascular networks in vitro. Acta Biotheoretica, 44(3):271–282, Nov 1996.

[36] A. Gamba, D. Ambrosi, A. Coniglio, A. de Candia, S. Di Talia, E. Giraudo, G. Serini, L. Preziosi, and F. Bussolino. Percolation, morphogenesis, and burgers dynamics in blood vessels formation. Phys. Rev. Lett., 90:118101, Mar 2003.

[37] Andras Szabo, Erica D. Perryn, and Andras Czirok. Network formation of tissue cells via preferential attraction to elongated structures. Phys. Rev. Lett., 98:038102, Jan 2007.

[38] N Kleinstreuer, D Dix, M Rountree, N Baker, N Sipes, and D et al. Reif. A computational model predicting disruption of blood vessel development. PLoS Comput Biol, 9(4):e1002996, 2013.

[39] J. R. D. Ramos, R. Travasso, and J. Carvalho. Capillary network formation from dispersed endothelial cells: Influence of cell traction, cell adhesion, and extracellular matrix rigidity. Phys. Rev. E, 97:012408, Jan 2018.

[40] Daria Stepanova, Helen M. Byrne, Philip K. Maini, and Tomás Alarcón. A multiscale model of complex endothelial cell dynamics in early angiogenesis. PLoS computational biology, 17(1):e1008055–e1008055, Jan 2021. 33411727[pmid].

[41] P. G. de Gennes and P. A. Pincus. Pair correlations in a ferromagnetic colloid. Physik der Kondensierten Materie, 11(3):189–198, August 1970.

[42] Patrick Ilg and Emanuela Del Gado. Non-linear response of dipolar colloidal gels to external fields. Soft Matter, 7:163–171, 2011.

[43] Andreas Kaiser, Sonja Babel, Borge ten Hagen, Christian von Ferber, and Hartmut Löwen. How does a flexible chain of active particles swell? The Journal of Chemical Physics, 142(12):124905, 2015.

[44] Guo-Jun Liao, Carol K. Hall, and Sabine H. L. Klapp. Dynamical self-assembly of dipolar active brownian particles in two dimensions. Soft Matter, 16(9):2208–2223, 2020.

[45] Nariaki Sakaï and C Patrick Royall. Active dipolar colloids in three dimensions: strings, sheets, labyrinthine textures and crystals. arXiv preprint arXiv:2010.03925, 2020.

[46] Francisca Guzmán-Lastra, Andreas Kaiser, and Hartmut Löwen. Fission and fusion scenarios for magnetic microswimmer clusters. Nature Communications, 7(1):13519, Nov 2016.

[47] Vitali Telezki and Stefan Klumpp. Simulations of structure formation by confined dipolar active particles. Soft Matter, 16:10537–10547, 2020.

[48] Ulrich S. Schwarz and Samuel A. Safran. Physics of adherent cells. Rev. Mod. Phys., 85:1327–1381, Aug 2013.

[49] I. B. Bischofs and U. S. Schwarz. Cell organization in soft media due to active mechanosensing. Proceedings of the National Academy of Sciences, 100(16):9274–9279, 2003.

[50] Dennis E. Discher, Paul Janmey, and Yu-li Wang. Tissue cells feel and respond to the stiffness of their substrate. Science, 310(5751):1139–1143, 2005.

[51] U. S. Schwarz, N. Q. Balaban, D. Riveline, A. Bershadsky, B. Geiger, and S. A. Safran. Calculation of forces at focal adhesions from elastic substrate data: the effect of localized force and the need for regularization. Biophysical journal, 83(3):1380–1394, Sep 2002. 12202364[pmid].

[52] J. D. Eshelby. The determination of the elastic field of an ellipsoidal inclusion, and related problems. Proceedings of the Royal Society of London. Series A, Mathematical and Physical Sciences, 241(1226):376–396, 1957.

[53] I. B. Bischofs and U. S. Schwarz. Effect of poisson ratio on cellular structure formation. Phys. Rev. Lett., 95:068102, Aug 2005.

[54] A. Zemel, F. Rehfeldt, A. E. X. Brown, D. E. Discher, and S. A. Safran. Optimal matrix rigidity for stress-fibre polarization in stem cells. Nature Physics, 6:468 –, Mar 2010.

[55] Adam J. Engler, Christine Carag-Krieger, Colin P. Johnson, Matthew Raab, Hsin-Yao Tang, David W. Speicher, Joseph W. Sanger, Jean M. Sanger, and Dennis E. Discher. Embryonic cardiomyocytes beat best on a matrix with heart-like elasticity: scar-like rigidity inhibits beating. Journal of Cell Science, 121(22):3794–3802, 2008.

[56] B. Friedrich, A. Buxboim, D. E. Discher, and S. A. Safran. Striated acto-myosin fibers can reorganize and register in response to elastic interactions with the matrix. Biophys. J., 100:2706, 2011.

[57] K. Dasbiswas, H. Shiqiong, F. Schnorrer, S. A. Safran, and A. D¿ Bershadsky. Ordering of myosin ii filaments driven by mechanical forces: experiments and theory. Philosophical Transactions of the Royal Society B: Biological Sciences, 373(1747):20170114, May 2018.

[58] Ilka B. Bischofs and Ulrich S. Schwarz. Collective effects in cellular structure formation mediated by compliant environments: A monte carlo study. Acta Biomaterialia, 2(3):253–265, 2006.

[59] Ovijit Chaudhuri, Justin Cooper-White, Paul A. Janmey, David J. Mooney, and Vivek B. Shenoy. Effects of extracellular matrix viscoelasticity on cellular behaviour. Nature, 584(7822):535–546, Aug 2020.

[60] Merrill E Asp, Minh-Tri Ho Thanh, Danielle A Germann, Robert J Carroll, Alana Franceski, Roy D Welch, Arvind Gopinath, and Alison E Patteson. Spreading rates of bacterial colonies depend on substrate stiffness and permeability. PNAS Nexus, 1(1):pgac025, 2022.

[61] Daniel Rüdiger, Kerstin Kick, Andriy Goychuk, Angelika M. Vollmar, Erwin Frey, and Stefan Zahler. Cell-based strain remodeling of a nonfibrous matrix as an organizing principle for vasculogenesis. Cell Reports, 32(6):108015, 2020.

[62] Joseph P. Califano and Cynthia A. Reinhart-King. A balance of substrate mechanics and matrix chemistry regulates endothelial cell network assembly. Cellular and Molecular Bioengineering, 1(2):122, Oct 2008.

[63] Katherine Copenhagen, Gema Malet-Engra, Weimiao Yu, Giorgio Scita, Nir Gov, and Ajay Gopinathan. Frustration-induced phases in migrating cell clusters. Science Advances, 4(9), 2018.

[64] Subhaya Bose, Kinjal Dasbiswas, and Arvind Gopinath. Matrix stiffness modulates mechanical interactions and promotes contact between motile cells. Biomedicines, 9(4), 2021.

[65] Subhaya Bose, Patrick S. Noerr, Ajay Gopinathan, Arvind Gopinath, and Kinjal Dasbiswas. Collective states of active particles with elastic dipolar interactions. Frontiers in Physics, 10, 2022.

[66] Yousef Javanmardi, Huw Colin-York, Nicolas Szita, Marco Fritzsche, and Emad Moeendarbary. Quantifying cell-generated forces: Poisson's ratio matters. Commun. phys., 4(1):237, November 2021.

[67] Dietrich Stauffer. Scaling theory of percolation clusters. Physics reports, 54(1):1–74, 1979.

[68] Fumiko Yonezawa, Shoichi Sakamoto, and Motoo Hori. Percolation in two-dimensional lattices. i. a technique for the estimation of thresholds. Physical Review B, 40(1):636–649, July 1989.

[69] Scott Kirkpatrick. Percolation and conduction. Reviews of Modern Physics, 45(4):574–588, October 1973.

[70] M. F. Sykes and J. W. Essam. Some exact critical percolation probabilities for bond and site problems in two dimensions. Physical Review Letters, 10(1):3–4, January 1963.

[71] Heiko Schmidle, Carol K. Hall, Orlin D. Velev, and Sabine H. L. Klapp. Phase diagram of two-dimensional systems of dipole-like colloids. Soft Matter, Dec 2011.

[72] Rumi De, Assaf Zemel, and Samuel A. Safran. Dynamics of cell orientation. Nature Physics, 3:655, Jul 2007. Article.

[73] Justin R. Tse and Adam J. Engler. Preparation of hydrogel substrates with tunable mechanical properties. Current Protocols in Cell Biology, 47(1), June 2010.

[74] Ramaswamy Krishnan, Darinka D Klumpers, Chan Y Park, Kavitha Rajendran, Xavier Trepat, Jan Van Bezu, Victor WM Van Hinsbergh, Christopher V Carman, Joseph D Brain, Jeffrey J Fredberg, et al. Substrate stiffening promotes endothelial monolayer disruption through enhanced physical forces. American Journal of Physiology-Cell Physiology, 300(1):C146–C154, 2011.

[75] E. M. Huisman and T. C. Lubensky. Internal stresses, normal modes, and nonaffinity in three-dimensional biopolymer networks. Phys. Rev. Lett., 106:088301, Feb 2011.

[76] Alessio Zaccone. Elastic deformations in covalent amorphous solids. Modern Physics Letters B, 27(05):1330002, 2013.

[77] Nicoletta I Petridou, Bernat Corominas-Murtra, Carl-Philipp Heisenberg, and Edouard Hannezo. Rigidity percolation uncovers a structural basis for embryonic tissue phase transitions. Cell, 184(7):1914–1928, 2021.

[78] Lia Papadopoulos, Pablo Blinder, Henrik Ronellenfitsch, Florian Klimm, Eleni Katifori, David Kleinfeld, and Danielle S Bassett. Comparing two classes of biological distribution systems using network analysis. PLoS Comput. Biol., 14(9):e1006428, September 2018.

[79] Henrik Ronellenfitsch and Eleni Katifori. Global optimization, local adaptation, and the role of growth in distribution networks. Physical Review Letters, 117(13):138301, Sep 2016.

[80] Cody O Crosby and Janet Zoldan. Mimicking the physical cues of the ECM in angiogenic biomaterials. Regenerative Biomaterials, 6(2):61–73, 02 2019.

[81] Brooke N. Mason, Alina Starchenko, Rebecca M. Williams, Lawrence J. Bonassar, and Cynthia A. Reinhart-King. Tuning three-dimensional collagen matrix stiffness independently of collagen concentration modulates endothelial cell behavior. Acta Biomaterialia, 9(1):4635–4644, 2013.

[82] Anthony J. Berger, Kelsey M. Linsmeier, Pamela K. Kreeger, and Kristyn S. Masters. Decoupling the effects of stiffness and fiber density on cellular behaviors via

an interpenetrating network of gelatin-methacrylate and collagen. Biomaterials, 141:125–135, 2017.

[83] David B. Brückner, Nicolas Arlt, Alexandra Fink, Pierre Ronceray, Joachim O. Rädler, and Chase P. Broedersz. Learning the dynamics of cell–cell interactions in confined cell migration. Proceedings of the National Academy of Sciences, 118(7), February 2021.

[84] M. Scianna, C.G. Bell, and L. Preziosi. A review of mathematical models for the formation of vascular networks. Journal of Theoretical Biology, 333:174 – 209, 2013.

[85] Umnia Doha, Onur Aydin, Md Saddam Hossain Joy, Bashar Emon, William Drennan, and M Taher A Saif. Disorder to order transition in cell-ecm systems mediated by cell-cell collective interactions. Acta Biomaterialia, 154:290–301, 2022.

[86] D. A. Beysens, G. Forgacs, and J. A. Glazier. Cell sorting is analogous to phase ordering in fluids. Proceedings of the National Academy of Sciences, 97(17):9467–9471, 2000.

[87] Marion Ghibaudo, Alexandre Saez, Léa Trichet, Alain Xayaphoummine, Julien Browaeys, Pascal Silberzan, Axel Buguin, and Benoît Ladoux. Traction forces and rigidity sensing regulate cell functions. Soft Matter, 4:1836–1843, 2008.

[88] Kalpana Mandal, Irène Wang, Elisa Vitiello, Laura Andreina Chacòn Orellana, and Martial Balland. Cell dipole behaviour revealed by ecm sub-cellular geometry. Nature Communications, 5(1):5749, Dec 2014.

[89] Daniel Riveline, Eli Zamir, Nathalie Q. Balaban, Ulrich S. Schwarz, Toshimasa Ishizaki, Shuh Narumiya, Zvi Kam, Benjamin Geiger, and Alexander D. Bershadsky. Focal Contacts as Mechanosensors: Externally Applied Local Mechanical Force Induces Growth of Focal Contacts by an Mdia1-Dependent and Rock-Independent Mechanism. Journal of Cell Biology, 153(6):1175–1186, 06 2001.

[90] C.L. Stokes, D.A. Lauffenburger, and S.K. Williams. Migration of individual microvessel endothelial cells: stochastic model and parameter measurement. Journal of Cell Science, 99(2):419–430, 06 1991.

[91] Caroline A. Schneider, Wayne S. Rasband, and Kevin W. Eliceiri. Nih image to imagej: 25 years of image analysis. Nature Methods, 9(7):671–675, Jul 2012.

[92] Bin Li and James H-C Wang. Fibroblasts and myofibroblasts in wound healing: force generation and measurement. Journal of tissue viability, 20(4):108–120, 2011.

[93] Carl-Philipp Heisenberg and Yohanns Bellaïche. Forces in tissue morphogenesis and patterning. Cell, 153(5):948–962, 2013.

[94] Kyra Campbell, Fabrizio Rossi, Jamie Adams, Ioanna Pitsidianaki, Francisco M Barriga, Laura Garcia-Gerique, Eduard Batlle, Jordi Casanova, and Andreu Casali. Collective cell migration and metastases induced by an epithelial-to-mesenchymal transition in drosophila intestinal tumors. Nature communications, 10(1):2311, 2019.

[95] Zhonggang Feng, Yusuke Wagatsuma, Masato Kikuchi, Tadashi Kosawada, Takao Nakamura, Daisuke Sato, Nobuyuki Shirasawa, Tatsuo Kitajima, and Mitsuo Umezu. The mechanisms of fibroblast-mediated compaction of collagen gels and the mechanical niche around individual fibroblasts. Biomaterials, 35(28):8078–8091, 2014.

[96] Pablo Fernandez and Andreas R Bausch. The compaction of gels by cells: a case of collective mechanical activity. Integrative biology, 1(3):252–259, 2009.

[97] Rudolf Clausius. Die mechanische behandlung der electricität. Vieweg+ Teubner Verlag, 1879.

[98] Ottaviano Fabrizio Mossotti. Discussione analitica sull'influenza che l'azione di un mezzo dielettrico ha sulla distribuzione dell'elettricità alla superficie di più corpi elettrici disseminati in esso, volume 22. Dai Tipi della RD Camera, 1846.

[99] Andrei Zakharov, Myra Awan, Arvind Gopinath, Sang-Joon John Lee, Anand K Ramasubramanian, and Kinjal Dasbiswas. Clots reveal anomalous elastic behavior of fiber networks. Science Advances, 10(2):eadh1265, 2024.

[100] Jacob Notbohm, Ayelet Lesman, Phoebus Rosakis, David A Tirrell, and Guruswami Ravichandran. Microbuckling in fibrin networks enables long-range cell mechanosensing. JR Soc., Interface, 12:20150320, 2015.

[101] M. C. Marchetti, J. F. Joanny, S. Ramaswamy, T. B. Liverpool, J. Prost, Madan Rao, and R. Aditi Simha. Hydrodynamics of soft active matter. Rev. Mod. Phys., 85:1143–1189, Jul 2013.

[102] Gerhard Gompper, Roland G Winkler, Thomas Speck, Alexandre Solon, Cesare Nardini, Fernando Peruani, Hartmut Löwen, Ramin Golestanian, U Benjamin Kaupp, Luis Alvarez, Thomas Kiørboe, Eric Lauga, Wilson C K Poon, Antonio DeSimone, Santiago Muiños-Landin, Alexander Fischer, Nicola A Söker, Frank Cichos, Raymond Kapral, Pierre Gaspard, Marisol Ripoll, Francesc Sagues, Amin Doostmohammadi, Julia M Yeomans, Igor S Aranson, Clemens Bechinger, Holger Stark, Charlotte K Hemelrijk, François J Nedelec, Trinish Sarkar, Thibault Aryaksama, Mathilde Lacroix, Guillaume Duclos, Victor Yashunsky, Pascal Silberzan, Marino Arroyo, and Sohan Kale. The 2020 motile active matter roadmap. Journal of Physics: Condensed Matter, 32(19):193001, feb 2020.

[103] Clemens Bechinger, Roberto Di Leonardo, Hartmut Löwen, Charles Reichhardt, Giorgio Volpe, and Giovanni Volpe. Active particles in complex and crowded environments. Reviews of Modern Physics, 88(4):045006, 2016.

[104] H. Chaté, F. Ginelli, G. Grégoire, F. Peruani, and F. Raynaud. Modeling collective motion: variations on the vicsek model. The European Physical Journal B, 64(3):451–456, Aug 2008.

[105] Pasquale Digregorio, Demian Levis, Antonio Suma, Leticia F Cugliandolo, Giuseppe Gonnella, and Ignacio Pagonabarraga. Full phase diagram of active brownian disks: From melting to motility-induced phase separation. Physical review letters, 121(9):098003, 2018.

[106] Daiki Nishiguchi, Junichiro Iwasawa, Hong-Ren Jiang, and Masaki Sano. Flagellar dynamics of chains of active janus particles fueled by an AC electric field. New Journal of Physics, 20(1):015002, jan 2018.

[107] T. Tlusty and S. A. Safran. Defect-induced phase separation in dipolar fluids. Science, 290(5495):1328–1331, 2000.

[108] Lorenzo Rovigatti, John Russo, and Francesco Sciortino. No evidence of gas-liquid coexistence in dipolar hard spheres. Physical review letters, 107(23):237801, 2011.

[109] Andreas Kaiser, Katarina Popowa, and Hartmut Löwen. Active dipole clusters: From helical motion to fission. Phys. Rev. E, 92:012301, Jul 2015.

[110] Soheil Fatehiboroujeni, Arvind Gopinath, and Sachin Goyal. Nonlinear oscillations induced by follower forces in prestressed clamped rods subjected to drag. Journal of Computational and Nonlinear Dynamics, 13(12):121005, 2018.

[111] Ashok S Sangani and Arvind Gopinath. Elastohydrodynamical instabilities of active filaments, arrays, and carpets analyzed using slender-body theory. Physical Review Fluids, 5(8):083101, 2020.

[112] Yaouen Fily, Priya Subramanian, Tobias M Schneider, Raghunath Chelakkot, and Arvind Gopinath. Buckling instabilities and spatio-temporal dynamics of active elastic filaments. Journal of the Royal Society Interface, 17(165):20190794, 2020.

[113] Raghunath Chelakkot, Michael F Hagan, and Arvind Gopinath. Synchronized oscillations, traveling waves, and jammed clusters induced by steric interactions in active filament arrays. Soft Matter, 17(4):1091–1104, 2021.

[114] U. S. Schwarz and S. A. Safran. Elastic interactions of cells. Phys. Rev. Lett., 88:048102, Jan 2002.

[115] Jing Yan, Ming Han, Jie Zhang, Cong Xu, Erik Luijten, and Steve Granick. Reconfiguring active particles by electrostatic imbalance. Nature materials, 15(10):1095–1099, 2016.

[116] M Cristina Marchetti, Yaouen Fily, Silke Henkes, Adam Patch, and David Yllanes. Minimal model of active colloids highlights the role of mechanical interactions in controlling the emergent behavior of active matter. Current Opinion in Colloid & Interface Science, 21:34–43, 2016.

[117] David Boal. Mechanics of the Cell. Cambridge University Press, 2 edition, 2012.

[118] Herbert Wagner and Heinz Horner. Elastic interaction and the phase transition in coherent metal-hydrogen systems. Advances in Physics, 23(4):587–637, 1974.

[119] H Zabel and H Peisl. Sample-shape-dependent phase transition of hydrogen in niobium. Physical Review Letters, 42(8):511, 1979.

[120] Anna-Kristina Marel, Matthias Zorn, Christoph Klingner, Roland Wedlich-Söldner, Erwin Frey, and Joachim O Rädler. Flow and diffusion in channel-guided cell migration. Biophysical journal, 107(5):1054–1064, 2014.

[121] Barath Ezhilan, Roberto Alonso-Matilla, and David Saintillan. On the distribution and swim pressure of run-and-tumble particles in confinement. Journal of Fluid Mechanics, 781, 2015.

[122] Jens Elgeti and Gerhard Gompper. Run-and-tumble dynamics of self-propelled particles in confinement. EPL (Europhysics Letters), 109(5):58003, 2015.

[123] Wen Yan and John F Brady. The force on a boundary in active matter. Journal of Fluid Mechanics, 785, 2015.

[124] Caleb Wagner, Michael Hagan, and Aparna Baskaran. Steady-state distributions of ideal active brownian particles under confinement and forcing. Journal of Statistical Mechanics: Theory and Experiment, 2017:043203, 04 2017.

[125] Alexis Poncet, Olivier Bénichou, Vincent Démery, and Daiki Nishiguchi. Pair correlation of dilute active brownian particles: From low-activity dipolar correction to high-activity algebraic depletion wings. Physical Review E, 103(1), January 2021.

[126] Roland G. Winkler and Gerhard Gompper. The physics of active polymers and filaments. The Journal of Chemical Physics, 153(4):040901, 2020.

[127] Giorgio Volpe, Sylvain Gigan, and Giovanni Volpe. Simulation of the active brownian motion of a microswimmer. American Journal of Physics, 82(7):659–664, 2014.

[128] Gerard A Vliegenthart, Arvind Ravichandran, Marisol Ripoll, Thorsten Auth, and Gerhard Gompper. Filamentous active matter: Band formation, bending, buckling, and defects. Science advances, 6(30):eaaw9975, 2020.

[129] Michael P Allen and Dominic J Tildesley. Computer simulation of liquids. Oxford university press, 2017.

[130] Hanumantha Rao Vutukuri, Maciej Lisicki, Eric Lauga, and Jan Vermant. Light-switchable propulsion of active particles with reversible interactions. Nature communications, 11(1):1–9, 2020.

[131] Hanumantha Rao Vutukuri, Bram Bet, René Van Roij, Marjolein Dijkstra, and Wilhelm TS Huck. Rational design and dynamics of self-propelled colloidal bead chains: from rotators to flagella. Scientific reports, 7(1):1–14, 2017.

[132] Roman Golkov and Yair Shokef. Shape regulation generates elastic interaction between living cells. New Journal of Physics, 19(6):063011, 2017.

[133] Mate Puljiz, Shilin Huang, Günter K. Auernhammer, and Andreas M. Menzel. Forces on rigid inclusions in elastic media and resulting matrix-mediated interactions. Phys. Rev. Lett., 117:238003, Nov 2016.

[134] Rob Phillips, Jane Kondev, and Julie Theriot. Physical Biology of the Cell. Garland Science, Taylor & Francis Group, New York, November 2008.

[135] Thomas Eisenstecken, Gerhard Gompper, and Roland Winkler. Conformational properties of active semiflexible polymers. Polymers, 8(8):304, Aug 2016.

[136] Xinyu Liao, Prashant K. Purohit, and Arvind Gopinath. Extensions of the worm-like-chain model to tethered active filaments under tension. The Journal of Chemical Physics, 153(19):194901, 2020.

[137] Tamás Vicsek, András Czirók, Eshel Ben-Jacob, Inon Cohen, and Ofer Shochet. Novel type of phase transition in a system of self-driven particles. Physical review letters, 75(6):1226, 1995.

[138] Madhuvanthi Guruprasad Athani and Daniel A Beller. Symmetry and stability of orientationally ordered collective motions of self-propelled, semiflexible filaments. arXiv preprint arXiv:2306.01180, 2023.

[139] Fereshteh L Memarian, Joseph D Lopes, Fabian Jan Schwarzendahl, Madhuvanthi Guruprasad Athani, Niranjan Sarpangala, Ajay Gopinathan, Daniel A Beller, Kinjal Dasbiswas, and Linda S Hirst. Active nematic order and dynamic lane formation of microtubules driven by membrane-bound diffusing motors. Proceedings of the National Academy of Sciences, 118(52):e2117107118, 2021.

[140] Jason E Hein and Donna G Blackmond. On the origin of single chirality of amino acids and sugars in biogenesis. Accounts of chemical research, 45(12):2045–2054, 2012.

[141] Julian Chela-Flores. The origin of chirality in protein amino acids. Chirality, 6(3):165–168, 1994.

[142] Atsushi Tamada, Satoshi Kawase, Fujio Murakami, and Hiroyuki Kamiguchi. Autonomous right-screw rotation of growth cone filopodia drives neurite turning. Journal of Cell Biology, 188(3):429–441, 2010.

[143] Yee Han Tee, Wei Jia Goh, Xianbin Yong, Hui Ting Ong, Jinrong Hu, Ignacius Yan Yun Tay, Shidong Shi, Salma Jalal, Samuel FH Barnett, Pakorn Kanchanawong, et al. Actin polymerisation and crosslinking drive left-right asymmetry in single cell and cell collectives. Nature communications, 14(1):776, 2023.

[144] Emily S Noël, Manon Verhoeven, Anne Karine Lagendijk, Federico Tessadori, Kelly Smith, Suma Choorapoikayil, Jeroen Den Hertog, and Jeroen Bakkers. A nodal-independent and tissue-intrinsic mechanism controls heart-looping chirality. Nature communications, 4(1):2754, 2013.

[145] G Lebreton, C Géminard, F Lapraz, S Pyrpassopoulos, D Cerezo, P Spéder, EM Ostap, and S Noselli. Molecular to organismal chirality is induced by the conserved myosin 1d. Science, 362(6417):949–952, 2018.

[146] José M Martín-Durán, Bruno C Vellutini, and Andreas Hejnol. Embryonic chirality and the evolution of spiralian left–right asymmetries. Philosophical Transactions of the Royal Society B: Biological Sciences, 371(1710):20150411, 2016.

[147] Eshel Ben-Jacob, Inon Cohen, Ofer Shochet, Adam Tenenbaum, András Czirók, and Tamás Vicsek. Cooperative formation of chiral patterns during growth of bacterial colonies. Physical Review Letters, 75(15):2899, 1995.

[148] Kazusa Beppu, Ziane Izri, Tasuku Sato, Yoko Yamanishi, Yutaka Sumino, and Yusuke T Maeda. Edge current and pairing order transition in chiral bacterial vortices. Proceedings of the National Academy of Sciences, 118(39):e2107461118, 2021.

[149] Zuzana Dunajova, Batirtze Prats Mateu, Philipp Radler, Keesiang Lim, Dörte Brandis, Philipp Velicky, Johann Georg Danzl, Richard W Wong, Jens Elgeti, Edouard Hannezo, et al. Chiral and nematic phases of flexible active filaments. Nature Physics, 19(12):1916–1926, 2023.

[150] Tzer Han Tan, Alexander Mietke, Junang Li, Yuchao Chen, Hugh Higinbotham, Peter J Foster, Shreyas Gokhale, Jörn Dunkel, and Nikta Fakhri. Odd dynamics of living chiral crystals. Nature, 607(7918):287–293, 2022.

[151] Serapion Pyrpassopoulos, Elizabeth A Feeser, Jessica N Mazerik, Matthew J Tyska, and E Michael Ostap. Membrane-bound myo1c powers asymmetric motility of actin filaments. Current Biology, 22(18):1688–1692, 2012.

[152] Kyongwan Kim, Natsuhiko Yoshinaga, Sanjib Bhattacharyya, Hikaru Nakazawa, Mitsuo Umetsu, and Winfried Teizer. Large-scale chirality in an active layer of microtubules and kinesin motor proteins. Soft Matter, 14(17):3221–3231, 2018.

[153] Jeffrey M Moore, Matthew A Glaser, and Meredith D Betterton. Chiral self-sorting of active semiflexible filaments with intrinsic curvature. Soft Matter, 17(17):4559–4565, 2021.

[154] Tetsuya Hiraiwa, Ryo Akiyama, Daisuke Inoue, Arif Md Rashedul Kabir, and Akira Kakugo. Collision-induced torque mediates the transition of chiral dynamic patterns formed by active particles. Physical Chemistry Chemical Physics, 24(47):28782–28787, 2022.

[155] Denis Chrétien and Stephen D Fuller. Microtubules switch occasionally into unfavorable configurations during elongation. Journal of molecular biology, 298(4):663–676, 2000.

[156] Francesco Pampaloni and Ernst-Ludwig Florin. Microtubule architecture: inspiration for novel carbon nanotube-based biomimetic materials. Trends in biotechnology, 26(6):302–310, 2008.

[157] Brian Mickey and Jonathon Howard. Rigidity of microtubules is increased by stabilizing agents. The Journal of cell biology, 130(4):909–917, 1995.

[158] Taviare L Hawkins, David Sept, Binyam Mogessie, Anne Straube, and Jennifer L Ross. Mechanical properties of doubly stabilized microtubule filaments. Biophysical journal, 104(7):1517–1528, 2013.

[159] Christoph A Weber, Ryo Suzuki, Volker Schaller, Igor S Aranson, Andreas R Bausch, and Erwin Frey. Random bursts determine dynamics of active filaments. Proceedings of the National Academy of Sciences, 112(34):10703–10707, 2015.

[160] George M Langford. Arrangement of subunits in microtubules with 14 profilaments. The Journal of cell biology, 87(2):521–526, 1980.

[161] Ignacio Arganda-Carreras, Rodrigo Fernández-González, Arrate Muñoz-Barrutia, and Carlos Ortiz-De-Solorzano. 3d reconstruction of histological sections: Application to mammary gland tissue. Microscopy Research and Technique, 73(11):1019–1029, March 2010.

[162] Callen Hyland, Aaron F. Mertz, Paul Forscher, and Eric Dufresne. Dynamic peripheral traction forces balance stable neurite tension in regenerating aplysia bag cell neurons. Scientific Reports, 4(1):4961, May 2014.

[163] Jérôme Solon, Ilya Levental, Kheya Sengupta, Penelope C. Georges, and Paul A. Janmey. Fibroblast adaptation and stiffness matching to soft elastic substrates. Biophysical Journal, 93(12):4453–4461, 2007.

[164] Lisa A. Flanagan, Yo-El Ju, Beatrice Marg, Miriam Osterfield, and Paul A. Janmey. Neurite branching on deformable substrates. Neuroreport, 13(18):2411–2415, Dec 2002. 12499839[pmid].

[165] Avril Stéphane Petit Claudie, Guignandon Alain. Traction force measurements of human aortic smooth muscle cells reveal a motor-clutch behavior. Molecular & Cellular Biomechanics, 16(2):87–108, 2019.

[166] Ariege Bizanti, Priyanka Chandrashekar, and Robert Steward. Culturing astrocytes on substrates that mimic brain tumors promotes enhanced mechanical forces. Experimental Cell Research, 406(2):112751, 2021.

[167] F. Pedregosa, G. Varoquaux, A. Gramfort, V. Michel, B. Thirion, O. Grisel, M. Blondel, P. Prettenhofer, R. Weiss, V. Dubourg, J. Vanderplas, A. Passos, D. Cournapeau, M. Brucher, M. Perrot, and E. Duchesnay. Scikit-learn: Machine learning in Python. Journal of Machine Learning Research, 12:2825–2830, 2011.

[168] Chase P Broedersz and Fred C MacKintosh. Modeling semiflexible polymer networks. Reviews of Modern Physics, 86(3):995, 2014.